Imaging and Spectroscopy of Laser Produced Annular Plasmas

A thesis submitted for the degree of:

DOCTOR OF PHILOSOPHY

Presented To:

The School of Physical Sciences, Faculty of Science
and Health, Dublin City University

Submitted by:

Ben Delaney

B. Sc. Hons.

Research Supervisor

Prof. John T. Costello

Co-Supervisors

Prof. Eugene T. Kennedy

September 2019

Declaration

I hereby certify that this material, which I now submit for assessment on the programme of study leading to the award of Doctor of Philosophy is entirely my own work, that I have exercised reasonable care to ensure that the work is original, and does not to the best of my knowledge breach any law of copyright, and has not been taken from the work of others save and to the extent that such work has been cited and acknowledged within the text of my work.

Signed: ______________________

ID No.: 13212913

Date: ______________________

For Tom.

Acknowledgements

First and foremost, I would like to thank my supervisor, Prof. John Costello, without whom the planning, undertaking and completion of this work would not have been possible. I would also like to thank Prof. Eugene Kennedy for his invaluable support at the most pivotal moments during my studies. Thanks, must also go to Dr. Mossy Kelly and Dr. Paddy Hayden, for their constant day to day support.

I also need to thank, in no particular order; Dan, Rachel, Stephen, Claire, Laurens, Hannah, Leah, Conor, Ronan, Brian, Paul, Silvin, Nicky, Colm, Columb, Cleo, Adam, Aoife, John, Deborah, Marion, Colm, Rob, Eoin, Terry and Skipper. All of whom made crucial contributions to getting me through this in one piece.

I would like to extend my thanks to all the support staff in DCU and the NCPST including Pat Wogan, Sheila Boughton, Alan Hughes, Lisa Peyton and Des Lavelle.

Finally, I would like to thank my family. To my parents, my brothers, my sisters and all the niblings – thanks for all the support you have given me throughout my studies.

Contents

Abstract

Ben Delaney

Imaging and Spectroscopy of Laser Produced Annular Plasmas

Laser induced breakdown spectroscopy (LIBS) has emerged as a commonly used analytical technique for both qualitative elemental identification and quantitative concentration determination in various academic and industrial fields. The ultimate performance of LIBS is dependent on the signal to background ratio (SBR) of the spectra which are acquired from a sample and is quantified as the limit of detection (LOD) of the technique. A significant body of work has already been reported in the literature aimed at lowering of the LOD of LIBS. This work includes investigations into the effects of; laser fluence, wavelength and pulse length as well as space and time optimization, along with double pulse plasma formation and reheating arrangements. The aim of the work presented here is to generate and investigate the stagnation layer formed in vacuo, at the centre of an annular plasma, and to employ it in a LIBS experiment on trace Cu in Al. This is achieved by retrofitting a single optical element, namely an axicon, to the focusing lens normally used for point plasma formation.

Spatially and temporally resolved imaging and spectroscopy are employed to track the formation and evolution of a stagnation layer at the centre of an annular plasma. Comparisons of these imaging and spectroscopy measurements are drawn with those obtained for a stagnation layer formed between two point seed plasmas, as well as for single laser produced plasma. An off axis parabolic mirror was used to carry out imaging and spectroscopy along the plasma expansion axis, normal to the target. A simple relay lens system was used for imaging and spectroscopy parallel to the target surface. The former is, to the best of my knowledge, the first time such an investigation into stagnation layers has been undertaken. The targets used were slabs of aluminium with trace amounts of copper.

Point, dual colliding and annular colliding plasmas were investigated to determine their relative merits in laser induced breakdown spectroscopy. It found that the limit-of-detection for trace amounts of Cu in Al is lowest for annular plasmas formed at low laser pulse energies of ca. 25 – 30 mJ.

1. Introduction

This thesis has been divided into seven chapters. A short description of the contents of each chapter is given below to aid the reader in navigating the thesis.

1.1. Thesis Structure

Chapter One gives a brief overview of the motivations for studying colliding laser produced plasmas from both a fundamental perspective and with a view to applying them to laser induced breakdown spectroscopy (LIBS) experiments. A short literature review focusing on the important papers published to date on colliding plasmas, laser induced breakdown spectroscopy and indeed on a combination of the two is also presented.

Chapter Two covers the relevant theoretical background required for the analysis and discussion of the results presented later in the thesis. The salient atomic processes in plasmas and thermodynamic equilibrium models are outlined. Next the fundamental principles of laser induced breakdown spectroscopy are described, as are the optical elements used to modify the laser beam to allow for the generation of stagnation layers.

Chapter Three provides a detailed discussion of the experimental systems used to obtain the data presented in chapters 4, 5 and 6. Spatio-temporal broadband emission imaging and spatio-temporal imaging spectroscopy setups are both described in detail. The plasma diagnostic techniques used to extract plasma plume evolution dynamics, electron temperature and electron density are discussed, along with the programming techniques and codes used to extract these parameters.

Chapter Four presents the results and analysis of both time integrated and time broadband imaging. Expansion dynamics of stagnation layers are compared to those of single plasma plumes with varying ambient pressure and laser fluence.

Chapter Five compares time integrated and time resolved spectroscopy of the stagnation layer generated at the centre of an annular plasma with a stagnation layer formed between dual colliding plasmas. Time resolved electron density and electron temperature values are extracted from these spectra and are presented at varying ambient pressure and for varying laser energy.

Chapter Six presents time resolved spectroscopy and its implementation for laser induced breakdown spectroscopy (LIBS) of trace elements in bulk aluminium. A comparison between signal-to-back ground ratio (SBR) and limit-of-detection (LOD) is made between stagnation layers and single plasma plumes for varying laser fluence.

Chapter Seven concludes the work by providing a summary of all of the results presented in the thesis. Suggestions for future experimental work are also made.

1.2. Review of Laser Produced Plasma Stagnation Layers and Laser Induced Breakdown Spectroscopy.

When a high power pulsed nanosecond (i.e., Q-switched) laser is focused onto a target (solid, liquid or gas) a hot and dense plasma is formed. Initial experiments on such laser produced plasmas (LPP) using pulsed ruby lasers were on solid targets [1]. As the field developed solid targets were interchanged with both liquids [2] and gases [3] while targets were also placed in vacuum chambers allowing investigations into plasma dynamics at varying pressures. Further variations including an experiment by Rumsby et. al [4] who split a laser beam using a wedge prism and focused both halves of this split beam onto a solid target within close proximity to each other, *in vacuo,* to ensure that these two expanding plasmas collided with each other. Along this collision front a bright band of plasma formed, this band of plasma is now referred to as a stagnation layer [5]. This appears to be the first observation of a stagnation layer in LPP collisions.

Traditional stagnation layer generation involves forming two adjacent plasmas, in an ambient gas at a pressure of less that 1×10^{-1} mbar as in Rumsby et al [4]. In this range the plasmas will expand not just away from the target but also laterally into each other in a direction parallel to the target [6]–[8]. The plasmas will decelerate at the collision plane, with their kinetic energy being converted into excitation energy, forming what is known as a stagnation layer; the two initial plasmas are referred to as seed plasmas. Most reported studies use a wedge prism to split a beam [9]–[11] and form two adjacent plasmas. In this thesis a biprism is used to form two collinearly expanding, adjacent LPPs. The rationale behind this decision will be outlined in Chapter 2.

Stagnation layers can also be generated using an axicon [12], [13], which can be defined as a conical lens or a rotationally symmetric prism (essentially the same entity) which in turn can be either convex or concave, to form an annular plasma, which, upon expansion, forms a stagnation layer at its centre. To the best of my knowledge no studies have been published which demonstrate the formation of a stagnation layer at the centre of an expanding annular plasma. Two studies of annular LPPs exist in the literature; Cabalin et al. [12] carried out imaging and spectroscopy under atmospheric pressure air conditions, while also showing secondary excitation of particulate matter within an annular plasma while Veloso et al. [13] carried out shadography based experiments on an annular plasma in a helium atmosphere. Neither of the papers report stagnation layer formation, but this is to be expected as the background pressure in both experiments was too high for plasma-plasma stagnation to develop.

Laser induced breakdown spectroscopy (LIBS) is a well-developed analytical technique which requires no sample preparation and promises fast, minimally destructive, qualitative and quantitative sample analysis

[14]–[18]. A significant body of work has been carried out with the aim of identifying and lowering of the limit of detection (LOD) of LIBS for various analytes [19]–[24], this work includes investigations into; laser fluence, wavelength and pulse length as well as space and time optimization along with double pulse arrangements [25]–[31]. While all of these techniques have shown improvements in limits of detection one important aim of this work is to further improve the LOD by adding a single optical element which can be readily retrofitted into existing LIBS apparatus.

Bibliography

[1] W. I. Linlor, "Some Properties of Plasma Produced by Laser Giant Pulse," *Phys.Rev.Lett.*, Vol. 12, no. 14, pp. 383–385, 1964.

[2] M. W. Dowley, K. B. Eisenthal, and W. L. Peticolas, "Laser-Produced Dielectric Breakdown in Liquids with Resulting Absorption of A Secondary Light Beam," *Phys. Rev. Lett.*, Vol. 18, no. 14, pp. 531–533, 1967.

[3] S. A. Ramsden and W. E. R. Davies, "Radiation Scattered from the Plasma Produced by a Focused Ruby Laser Beam," *Phys.Rev.Lett.*, Vol. 13, no. 7, pp. 227–229, 1964.

[4] P. T. Rumsby, J. W. M. Paul, and M. M. Masoud, "Interactions between two colliding laser produced plasmas," *Plasma Phys.*, Vol. 16, no. 10, p. 969, 1974.

[5] H. Luna, K. D. Kavanagh, and J. T. Costello, "Study of a colliding laser-produced plasma by analysis of time- and space-resolved image spectra," *J. Appl. Phys.*, Vol. 101, no. 3, Art. No. 033302, 2007.

[6] S. L. Gupta and R. K. Thareja, "Photoluminescence of nanoparticles in vapour phase of colliding plasma," *J. Appl. Phys.*, no. 113, Art. No. 143308 2013.

[7] T. Cummins *et al.*, "Colliding laser-produced plasmas as targets for laser-generated extreme ultraviolet sources," *Appl. Phys. Lett.*,

Vol. 105, no. 4, Art. No. 044101, 2014.

[8] A. K. Saxena, R. K. Singh, H. C. Joshi, and A. Kumar, "Spectroscopic investigation of molecular formation in laterally colliding laser-produced carbon plasmas," *Appl. Opt.*, Vol. 58, no. 3, pp. 561–570, 2019.

[9] P. Hough, C. McLoughlin, S. S. Harilal, J. P. Mosnier, and J. T. Costello, "Emission characteristics and dynamics of the stagnation layer in colliding laser produced plasmas," *J. Appl. Phys.*, Vol. 107, no. 2, Art. No. 024904, 2010.

[10] C. Fallon, P. Hayden, N. Walsh, E. T. Kennedy, and J. T. Costello, "The Effect of Wedge Angle on the Evolution of a Stagnation Layer in a Colliding Plasma Experiment," *J. Phys. Conf. Ser.*, Vol. 548, no. 1, Art. No. 012036, 2014.

[11] C. Fallon, P. Hayden, N. Walsh, E. T. Kennedy, and J. T. Costello, "Target geometrical effects on the stagnation layer formed by colliding a pair of laser produced copper plasmas," *Phys. Plasmas*, Vol. 22, no. 9, Art. No. 093506, 2015.

[12] L. M. Cabalin and J. J. Laserna, "Atomic emission spectroscopy of laser-induced plasmas generated with an annular-shaped laser beam," - *Journal of Analytical Atomic Spectrometry*, Vol. 19, no. 4. pp. 445-450, 2004.

[13] F. Veloso, H. Chuaqui, R. Aliaga-Rossel, M. Favre, I. H. Mitchell, and E. Wyndham, "Laser-produced annular plasmas," *Rev. Sci. Instrum.*, Vol. 77, no. 6, Art. No. 063506, 2006.

[14] D. W. Hahn and N. Omenetto, "Laser-Induced Breakdown Spectroscopy (LIBS), Part I: Review of Basic Diagnostics and Plasma--Particle Interactions: Still-Challenging Issues Within the Analytical Plasma Community," *Appl. Spectrosc.*, Vol. 64, no. 12, pp. 335A-366A, 2010.

[15] D. W. Hahn and N. Omenetto, "Laser Induced Breakdown

Spectroscopy (LIBS), Part II: Review of Instrumental and Methodological Approaches th Material Analysis and Applications to Different Fields," *Appl. Spectrosc.*, Vol. 66 No 4, pp. 347-419, 2012.

[16] D. A. Cremers, F.-Y. Yueh, J. P. Singh, and H. Zhang, "Laser-Induced Breakdown Spectroscopy, Elemental Analysis Update based on the original article by Fang-Yu Yueh, Jagdish P. Singh, Hansheng Zhang, Encyclopedia of Analytical Chemistry, © 2000, John Wiley & Sons, Ltd.," in *Encyclopedia of Analytical Chemistry*, American Cancer Society, 2012.

[17] F. J. Fortes, J. Moros, P. Lucena, L. M. Cabalín, and J. J. Laserna, "Laser-Induced Breakdown Spectroscopy," *Anal. Chem.*, Vol. 85, no. 2, pp. 640–669, 2013.

[18] J. El Haddad, L. Canioni, and B. Bousquet, "Good practices in LIBS analysis: Review and advices," *Spectrochim. Acta Part B At. Spectrosc.*, Vol. 101, pp. 171–182, 2014.

[19] H. Li, M. Liu, Z. Chen, and R. Li, "Quantitative analysis of impurities in aluminum alloys by laser-induced breakdown spectroscopy without internal calibration," *Transactions of Nonferrous Metals Society of China*, Vol. 18, no. 1. pp. 222–226, 2008.

[20] T. Takahashi and B. Thornton, "Quantitative methods for compensation of matrix effects and self-absorption in Laser Induced Breakdown Spectroscopy signals of solids," *Spectrochim. Acta Part B At. Spectrosc.*, Vol. 138, pp. 31–42, 2017.

[21] B. Sezer *et al.*, "Detection and quantification of a toxic salt substitute (LiCl) by using laser induced breakdown spectroscopy (LIBS)," *Meat Sci.*, Vol. 135, pp. 123–128, 2018.

[22] M. A. Ismail, H. Imam, A. Elhassan, W. T. Youniss, and M. A. Harith, "LIBS limit of detection and plasma parameters of some elements in two different metallic matrices," *J. Anal. At.*

Spectrom., Vol. 19, no. 4, pp. 489–494, 2004.

[23] M. Corsi *et al.*, “Effect of Laser-Induced Crater Depth in Laser-Induced Breakdown Spectroscopy Emission Features,” *Appl.Spectrosc.*, Vol. 59, no. 7, pp. 853–860, 2005.

[24] Z. Z. Wang, Y. Deguchi, M. Kuwahara, J. J. Yan, and J. P. Liu, “Enhancement of Laser-Induced Breakdown Spectroscopy (LIBS) Detection Limit Using a Low-Pressure and Short-Pulse Laser-Induced Plasma Process,” *Appl. Spectrosc.*, Vol. 67, no. 11, pp. 1242–1251, 2013.

[25] D. A. Cremers, L. J. Radziemski, and T. R. Loree, “Spectrochemical Analysis of Liquids Using the Laser Spark,” *Appl. Spectrosc.*, Vol. 38, no. 5, pp. 721–729, 1984.

[26] X. Jiang, P Hayden, J T Costello and E T Kennedy Dual-Pulse Laser Induced Breakdown Spectroscopy with Ambient Gas in the Vacuum Ultraviolet: Optimization of Parameters for Detection of C and S in Steel, Spectrochim. Acta Part B: At. Spectrosc. Vol 901 pp. 106-113, 2014.

[27] H. Shakeel, S. U. Haq, Q. Abbas, A. Nadeem, and V. Palleschi, “Quantitative analysis of Ge/Si alloys using double-pulse calibration-free laser-induced breakdown spectroscopy,” *Spectrochim. Acta Part B At. Spectrosc.*, Vol. 146, pp. 101–105, 2018.

[28] G. S. Senesi *et al.*, “Elemental and mineralogical imaging of a weathered limestone rock by double-pulse micro-Laser-Induced Breakdown Spectroscopy,” *Spectrochim. Acta Part B At. Spectrosc.*, Vol. 143, pp. 91–97, 2018.

[29] M. Cui, Y. Deguchi, Z. Wang, S. Tanaka, Y. Fujita, and S. Zhao, “Improved Analysis of Manganese in Steel Samples Using Collinear Long–Short Double Pulse Laser-Induced Breakdown Spectroscopy

(LIBS)," *Appl. Spectrosc.*, Sep. 2018. https://doi.org/10.1177/0003702818803943

[30] D. H. Zhang, X. X. Yuan, M. G. Su, Q. Min, C. Z. Dong, and D. X. Sun, "Shielding and diagnostics of laser-induced air plasmas generated in collinear double pulse configuration," *Phys. Plasmas*, Vol. 25, no. 6, Art. No. 63112, 2018.

[31] M. Burger, P. J. Skrodzki, L. A. Finney, J. Hermann, J. Nees, and I. Jovanovic, "Isotopic analysis of deuterated water via single- and double-pulse laser-induced breakdown spectroscopy," *Phys. Plasmas*, Vol. 25, no. 8, Art. No. 083115, 2018.

2. Theoretical Background

2.1. Plasma Definition

Plasma is normally designated as the 4th state of matter; it is an electrically neutral gas which contains positive and negative species which are both bound and unbound. These species are made up of free electrons, partially or wholly ionised atoms, and ionised molecules and in some cases, neutral, excited atoms and molecules. The bulk neutrality of a plasma is expressed in Equation 1 [1].

$$n_e = \sum_z n_z Z \qquad \text{Equation 1}$$

where n_e is the electron density and n_z is the density of ions of charge Z.

There are three criteria which an ionised gas must satisfy if it is to be considered plasma. The first two criteria ensure that the plasma undergoes collective behaviour, while the third ensures the ionised gas acts like a plasma rather than a neutral gas [2].

- The Debye screening length must be short compared to the size of the plasma.

$$\lambda_D << L \qquad \text{Equation 2}$$

where L is the dimension or extent of the plasma.

- The density of the plasma must be such that the number of charge carriers within the Debye sphere must be greater than unity, to ensure collective behaviour of the charged particles.

$$N_D >> 1 \qquad \text{Equation 3}$$

- The (electron) plasma frequency is high compared to the electron-neutral collision frequency.

$$\omega_p > \omega_{e-n} \qquad \text{Equation 4}$$

The first criterion requires that the size of the plasma must be much larger than the Debye length, λ_D, the distance over which plasma shielding, the redistribution of plasma species in space to achieve quasi neutrality, takes place. Plasma shielding occurs as the negatively charged electrons tend to accumulate around positively charged ions and in so doing shield the rest of the plasma from the electric field of the ion by preventing it from penetrating into the plasma beyond the Debye length [2].

$$\lambda_D = \left(\frac{\varepsilon_0 k_B T_e}{n_e e^2}\right)^{\frac{1}{2}} \qquad \text{Equation 5}$$

where n_e is the electron density, e is the charge on the electron or the electronic charge, m_e is the mass of an electron, T_e is the electron temperature, k_B is Boltzmann's constant and ε_0 is the permittivity of free space. The Debye length is more commonly thought of in three dimensions as the Debye sphere. If a positive ion was placed at its centre, at a distance greater than its radius the Columbic field from this ion would not be felt [2].

The second criterion relates to the plasma parameter, N_D, and is essentially equal to the number of particles contained within the Debye sphere; it is a check that there are enough particles in the Debye sphere to ensure that the concept of plasma shielding is still statistically valid [2].

$$N_D = \frac{4}{3}\pi n_e {\lambda_D}^3 \qquad \text{Equation 6}$$

The first two criteria ensure the quasi neutrality and collective movement of the plasma while the third ensures that it acts like plasma and not just a hydrodynamic fluid, the principal difference being that the motion of plasma is controlled by electromagnetic forces. If ω is the frequency of a typical plasma oscillation and τ is the mean time between collisions with neutral atoms, $\omega\tau$ should be greater than unity to behave like a plasma rather than a neutral gas [2]. In this sense equation (4) becomes $\omega\tau > 1$.

Assuming that these three criteria hold, if there is a displacement of electrons within the plasma they will tend to return to their equilibrium positions. An oscillatory solution to the equation of the motion of these electrons exists, the frequency of which, ω_p, is known as the plasma frequency [1].

$$\omega_p = \left(\frac{n_e e^2}{m_e \varepsilon_0}\right)^{\frac{1}{2}} \qquad \text{Equation 7}$$

where n_e is the electron density, e is the charge of an electron, m_e is the mass of an electron and ε_0 is the permittivity of free space.

If an electromagnetic wave propagates through a plasma, it will undergo dispersion where the dispersion relation for an electromagnetic wave propagating in a plasma is given by [1]

$$\omega^2 = {\omega_p}^2 + c^2 k^2 \qquad \text{Equation 8}$$

$$k = \frac{2\pi}{\lambda} \qquad \text{Equation 9}$$

ω is the frequency of the propagating wave, ω_p is the plasma frequency and c is the speed of light.

From Equation 8 it is clear that when $\omega > \omega_p$, k is real and a wave will be able to propagate within the plasma. However if $\omega_p > \omega$, k is imaginary and the wave will not propagate through the plasma. If the value of ω_p is set to the value of the incident radiation field and combined with Equation 7 an expression for the critical density of plasma can be formed

$$n_c = \frac{\omega_p^2 \, m_e \varepsilon_0}{e^2} \qquad \text{Equation 10}$$

2.2. Laser Produced Plasma Formation in Vacuo

In the nanosecond regime plasma formation occurs due to the heating of the material onto which a high intensity laser is focused. High intensity is defined in this thesis as $10^8 - 10^{10}$ W/cm^2. The irradiated zone initially melts and then, as more laser energy is absorbed, vaporises to form a gas which contains ionised atoms which have been stripped of at least one electron. This happens during the leading edge of the laser pulse. Once the plasma has been formed, the remaining laser energy is absorbed by the expanding plasma via the process of inverse bremsstrahlung, as well as by the target. This occurs while the electron density of the plasma is below the critical density. Figure 2.1 gives approximate time scales for the various stages of the plasma formation and evolution which are based upon spectroscopic results.

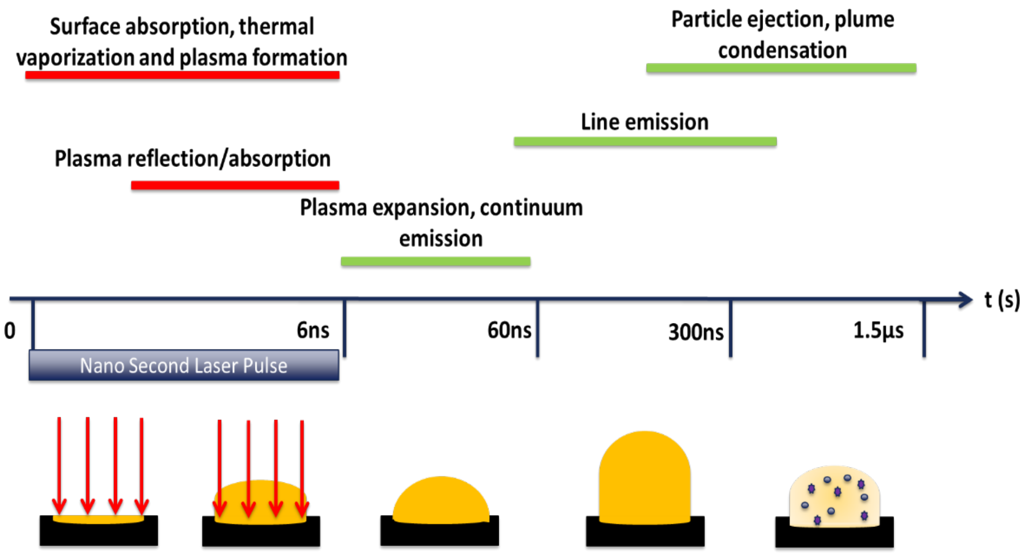

Figure 2.1: Laser produced plasma expansion in vacuo showing the different epoques from the formation on a nanosecond timescale to late phase plume condensation which can yield clusters for materials growth [3].

2.2.1 Laser-Matter Interaction

The depth that laser radiation penetrates into a solid target surface is typically less than a single optical wavelength and is referred to as the skin depth of the material. The skin depth of a material varies with the optical frequency of the incident electromagnetic radiation, as shown by Equation 11 [4].

$$\delta = (\pi \nu \mu_0 \sigma)^{-\frac{1}{2}} \qquad \text{Equation 11}$$

where δ is the skin depth of the material, v is the frequency of the incident radiation, μ_0 is the permeability of free space and σ is the conductivity of the target.

The primary target material used in this thesis is aluminium, which has a conductivity of 3.767×10^7 S/m, while the primary wavelength is the fundamental frequency of an Nd:YAG laser, 2.819×10^{14} Hz. For these parameters, the skin depth given by Equation 11 is approximately 5nm, significantly shorter than the 1064nm wavelength of the incident radiation, and much shallower than the crater depth for one laser shot, which is on the order of 10µm.

Even given this shallow skin depth, the incident radiation can still interact sufficiently with conduction band electrons to heat, and eventually, evaporate the target, forming a plasma at the leading edge of the laser pulse.

2.2.2 Laser-Plasma Interaction

Once this initial plasma is formed free electrons begin to absorb laser radiation via the inverse bremsstrahlung process, described in detail in section 2.3. This leads to an increase in the kinetic energy of free electrons which in turn further ionise plasma atoms and ions which drives the electron density of the plasma to even higher values.

While this density is below the critical density, a fraction of the laser light will be absorbed by the target leading to further evaporation and ionisation, adding more material to the plasma, while some of the remaining fraction will be absorbed by the plasma. However once the critical density is reached the plasma becomes opaque to the incident radiation and it will be reflected. The critical density, n_c, is calculated using Equation 10 above or more simply by using Equation 12 [5].

$$n_c \approx \frac{9.85 \times 10^{20}}{\lambda^2} \qquad \text{Equation 12}$$

where λ is units of μm and n_c has units of cm^{-3}. The electron density will cyclically increase and decrease to and from the critical density for the duration of the laser pulse.

2.2.3 Plasma Expansion

The plasma can be assumed to behave as a high-temperature; high pressure gas which expands isothermally for the duration of the laser pulse. In this isothermal regime the volume and density of the plasma self-adjust to ensure the thermal energy of the plasma remains constant. This is achieved by equilibrating the rate of thermal gain, through inverse bremsstrahlung and collisional excitation, with the rate of thermal loss to the environment. Equation 13 and Equation 14 can be used to model the three dimensional (3D) expansion of the plasma plume during and after the laser pulse and were developed by Singh and Narayan [6]. These authors treated the plasma as an ideal gas at high pressure and high temperature which is initially confined in small dimensions and then is allowed to expand rapidly in vacuum. The plasma processes are divided into three distinct phases, (i) the interaction of the laser beam with the bulk target, (ii) the plasma formation, heating and initial three-dimensional isothermal expansion, and (iii) adiabatic expansion. Narayan and Singh set up the equations of compressible gas dynamics to simulate the expansion of the plasma in the last two phases While most of the laser's energy is deposited in the thin layer around the critical density boundary (deflagration zone) the plasma in front of this zone expands isothermally, relatively transparent to the laser light due to its lower electron density. So the expansion can be considered to be isothermal at this stage because the plasma still has a small velocity and volume, therefore it can thermalise faster than the characteristic plasma expansion time. The time evolution of the coordinates of the expanding plasma plume are given by:

$$X(t)\left[\frac{1}{t}\frac{dX}{dt}+\frac{d^2X}{dt^2}\right] = Y(t)\left[\frac{1}{t}\frac{dY}{dt}+\frac{d^2Y}{dt^2}\right] = Z(t)\left[\frac{1}{t}\frac{dZ}{dt}+\frac{d^2Z}{dt^2}\right] = \frac{kT_0}{M} \qquad \text{Equation 13}$$

where *Z* is the direction normal to the target surface, while *X* and *Y* are parallel to the target surface and orthogonal to one another, T_0 is the isothermal temperature of the plasma, *k* is Boltzmann's constant, *M* is the atomic weight of the plasma species and *X(t)*, *Y(t)* and *Z(t)* are the plume dimensions as a function of time.

After the termination of the laser pulse the plasma can be viewed as expanding adiabatically. Adiabatic expansion is expansion in which no heat is transferred, in this case from the plasma to its surroundings; instead, as the plasma expands it cools by the conversion of thermal energy into kinetic energy [6].

$$X(t)\left[\frac{d^2X}{dt^2}\right] = Y(t)\left[\frac{d^2Y}{dt^2}\right] = Z(t)\left[\frac{d^2Z}{dt^2}\right] = \frac{kT_0}{M}\left[\frac{X_0Y_0Z_0}{X(t)Y(t)Z(t)}\right]^{\gamma-1} \qquad \text{Equation 14}$$

where γ is the ratio of the specific heat capacities at constant pressure and volume and *X, Y, Z,* T_0*, k*, *M*, *X(t)*, *Y(t)*, *Z(t)* are all as described for the case of Equation 13.

2.3. Stagnation Layers in Laser Produced Plasmas

When two laser plasmas are formed adjacent to each other, in an ambient gas at a pressure of less that $1\text{x}10^{-1}$ mbar, the plasmas will expand not just away from the target but also laterally into each other in a direction parallel to the target [7]. The plasmas will decelerate at the collision plane, with their kinetic energy being converted into excitation energy, forming what is known as a stagnation layer; the two initial plasmas are known as seed plasmas.

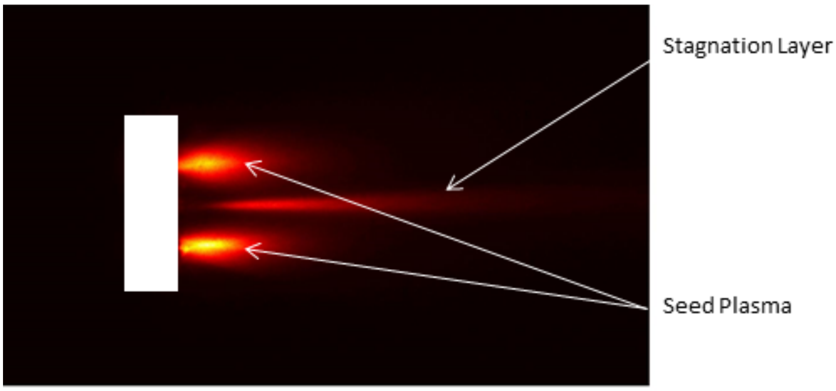

Figure 2.2: Time integrated broadband image of a stagnation layer formed between two seed plasmas created by splitting and focusing the 532nm second harmonic output of a nanosecond pulsed Nd:YAG laser with 235mJ pulse energy or ca. 120mJ per focus, onto a copper target.

Current interest in stagnation layers comes from the ability to manipulate their physical characteristics such as density, temperature, shape, etc. by varying target geometry [8] or by the laser-target interaction characteristics for the seed plasmas [3].

The interpenetration of the two seed plasmas has been modelled by Rambo et al. [9] who used a one-dimensional planar multifluid model to describe the characteristics of the stagnation layer; the main equation from this model is given below:

$$\xi = \frac{D}{\lambda_{ii}} \qquad \text{Equation 15}$$

where ξ is the collisionality parameter, D is the distance between the two seed plasmas and

$$\lambda_{ii}(1-2) = \frac{4\pi\epsilon_0 {m_i}^2 {v_{12}}^4}{e^4 Z^4 n_i \ln(\Lambda_{12})} \qquad \text{Equation 16}$$

where λ_{ii} is the ion-ion mean free path, m_i is the ion mass, v_{12} is the relative velocity between the two plasma plumes, e is the charge state of the ion, n_i is the ion density of the plasma, ϵ_0 is the permittivity of free space and $\ln(\Lambda_{12})$ is the so called Coulomb parameter [10].

The stagnation layer shown in Figure 2.2 was created using the simplest and most common experimental set up in which a wedge prism is used to split the laser beam into two parts; these beams are then focused onto the target with a simple single lens as shown in Figure 2.3.

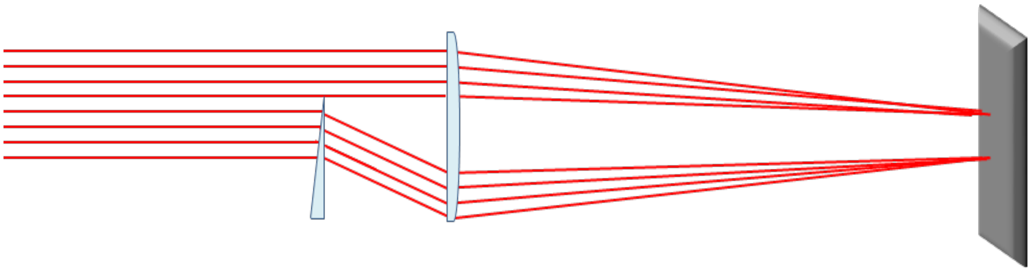

Figure 2.3: Traditional stagnation layer generation using a wedge prism.

This system while useful for quickly and easily generating stagnation layers does have some drawbacks, principally the inherent asymmetry of the set up. Most importantly the deflected beam gives rise to a focal spot which is partially elliptical due to astigmatism and hence potentially to a seed plasma with different characteristics than the one formed by the undeflected portion of the laser beam. Consequently the resulting stagnation layer can also become asymmetric [11]. It is proposed here that the generation of a more symmetric stagnation layer will lead to more uniform temperature and density distributions within stagnation layers. To generate a symmetric stagnation layer the wedge prism in the above set up was replaced with an axicon and a biprism, in separate experiments.

2.4. Atomic Processes

There are a plethora of atomic processes which involve atoms, ions and electrons in a LPP. These processes can be separated into three categories: free – free, free – bound and bound – bound. Each of these processes can be further classified as being either radiative or collisional. The classification of each of the processes is given in Table 2.1.

Table 2.1: Atomic processes present in Laser Produced Plasmas [12].

Process	Type	Excitation	De-Excitation
Free – Free	Collisional	Inverse Bremsstrahlung	–
	Radiative	–	Bremsstrahlung
Free – Bound	Collisional	Electron Impact Ionisation	3–Body Recombination
	Radiative	Photoionisation	Radiative Recombination
Bound – Bound	Collisional	Electron Impact Excitation	Electron Impact De–excitation
	Radiative	Photoabsorption	Spontaneous Decay

Both photoabsorption and photoionisation are responsible for the initial excitation of the target material, arising from which a laser produced plasma is subsequently formed. Bremsstrahlung contributes to the background continuum of the plasma which is present in the early stages of the plasma, while inverse Bremsstrahlung plays an important role in the absorption of laser radiation by the plasma. Once the plasma is established the remaining processes occur at varying rates until the plasma returns to a non-excited state. A description of each of these processes is given below [12].

2.4.1 Free – Free Processes

There are two free – free processes which occur in a laser produced plasma, namely Bremsstrahlung, which is a radiative de-excitation process, and Inverse Bremsstrahlung, which is a collisional excitation process.

The term 'Bremsstrahlung' comes from a combination of the German words for braking and radiation. The process occurs when an electron is decelerated, by the Coulomb field of an ion from which it is scattered. During this deceleration the electron loses kinetic energy, which is released in the form of a photon. A schematic diagram of this process is shown in Figure 2.4 and the process equation is given by Equation 17 [12].

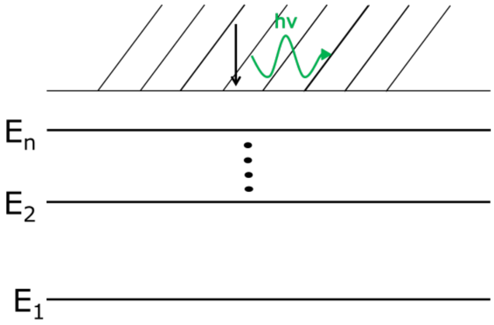

Figure 2.4: Schematic diagram of the Bremsstrahlung atomic process [12].

$$e(\varepsilon_2) + A \rightarrow e(\varepsilon_1) + A + \gamma \qquad \text{Equation 17}$$

where *e* is the free electron, ε_2 and ε_1 are the energies of the electron before and after the process while *A* represents the atom or ion and γ is the photon.

The inverse Bremsstrahlung process occurs when a photon is absorbed by a free electron which increases in kinetic energy by an amount equal to photon energy. In order for momentum to be conserved this absorption must take place in the presence of an ion which carries away the extra momentum gained. A schematic of this process is shown in Figure 2.5 and is given by Equation 18 [12].

$$e(\varepsilon_1) + A + \gamma \rightarrow e(\varepsilon_2) + A \qquad \text{Equation 18}$$

where *e*, ε_1, ε_2, *A* and γ are defined above.

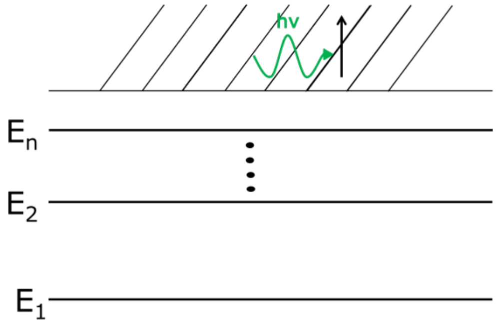

Figure 2.5: Schematic diagram of the Inverse - Bremsstrahlung atomic process [12].

2.4.2 Free – Bound Processes

There are four free – bound processes which manifest themselves within laser produced plasmas, two collisional, namely electron impact ionisation and 3-body recombination, and two radiative, photoionisation and radiative recombination.

Electron impact ionisation is one of the most important processes in hot, optically thin plasmas. It takes place when a free electron collides with an atom or ion and one or more bound electrons are promoted into the continuum. The kinetic energy of the ejected electron will be equal to the energy lost by the free electron minus the binding energy of the atom or ion.

3-body recombination takes place when two free electrons enter the volume of an ion. One of the electrons is captured by the ion and enters a bound state while the other electron takes up the excess energy lost by the captured electron. Figure 2.6 is a schematic diagram illustrating both of these processes. Equation 19 and Equation 20 describe electron impact ionisation and 3-body recombination [12].

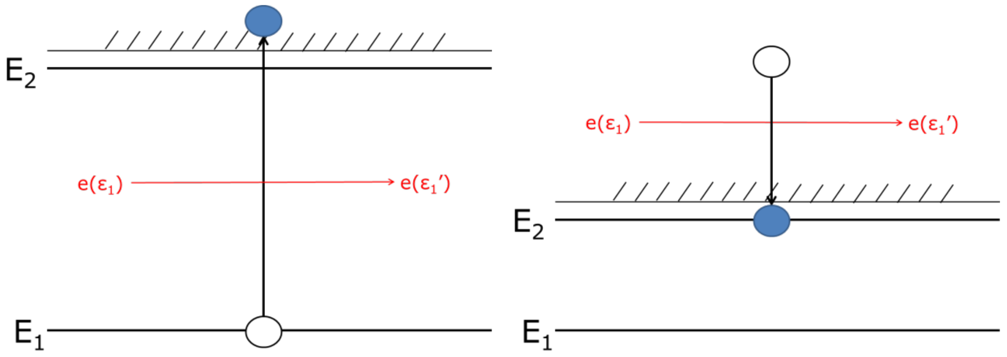

Figure 2.6: Schematic diagram of the electron impact ionisation atomic process (left) and of the 3-body recombination atomic process (right) [12].

$$A^{z} + e_1 \rightarrow A^{z+1} + e_1{}' + e_2 \qquad \text{Equation 19}$$

where A^z is the ion in the charge state z, A^{z+1} is the ion in the charge state z+1, e_1 is the free electron before the collision, e_1' is the free electron, with lower energy, after the collision and e_2 is the ionised electron.

The three body recombination process is given by:

$$A^{z+1} + e_1(\varepsilon_1) + e_2(\varepsilon_2) \rightarrow A^{z} + e_1(\varepsilon_1') \qquad \text{Equation 20}$$

where A^z and A^{z+1} are described above, $e_1(\varepsilon_1)$ and $e_2(\varepsilon_2)$ are the free electrons before the process and $e_1(\varepsilon_1')$ represents the free electron with increased energy after the capture of the other free electron by the ion.

In the process of photoionisation a photon is absorbed by a bound electron in an atom or ion, which promotes the electron into the continuum with a kinetic energy which is equal to the energy of the absorbed photon minus the binding energy of the atom or ion concerned. The inverse process is radiative recombination whereby a free electron is captured into one of the bound states of an ion and a photon is emitted by the ion to account for excess energy. Figure 2.7 is a schematic of both of these processes; Equation 21 and Equation 22 represent photoionisation and radiative recombination respectively [12].

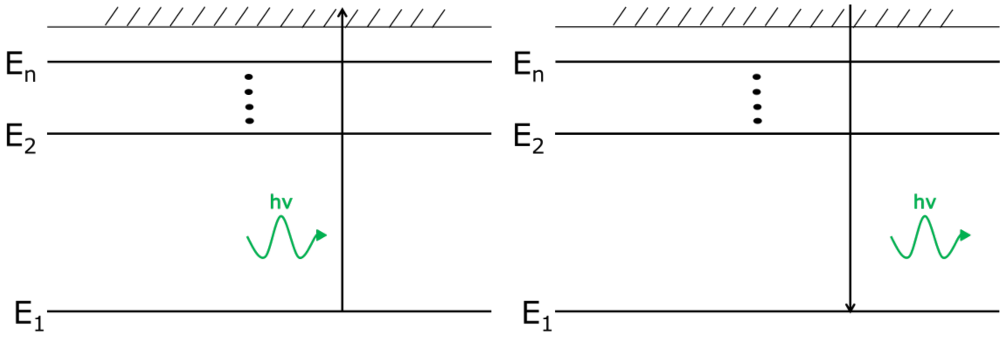

Figure 2.7: Schematic diagram of photoionisation process (left) and of the radiative recombination process (right) [12].

$$A^{z} + \gamma \rightarrow A^{z+1} + e \qquad \text{Equation 21}$$

where A^{z} and A^{z+1} are described above, γ is the absorbed (or emitted) photon and e is the ionised free electron.

$$A^{z+1} + e \rightarrow A^{z} + \gamma \qquad \text{Equation 22}$$

where A^{z} and A^{z+1} are described above, γ is the emitted photon and e is the captured free electron.

2.4.3 Bound – Bound Processes

Similarly there are four bound – bound processes, two collisional, electron impact excitation and electron impact de-excitation, and two radiative, photoabsorption and spontaneous decay.

Electron impact excitation is the result of a collision between an electron and an atom or ion in the plasma. When the electron collides with an atom or ion, energy is transferred to a bound electron which is promoted to a higher, but still bound, energy level within the atom or ion. As a result the colliding electron loses an amount of energy equal to that which the bound electron gains. The inverse process is electron impact de-excitation. In this case an electron collides with an excited atom or ion, which is de-excited and the excess energy is emitted in the form of a photon. Figure 2.8 is a schematic of both of these processes, Equation 24 gives the equation for electron impact excitation while Equation 23 represents electron impact de-excitation [12].

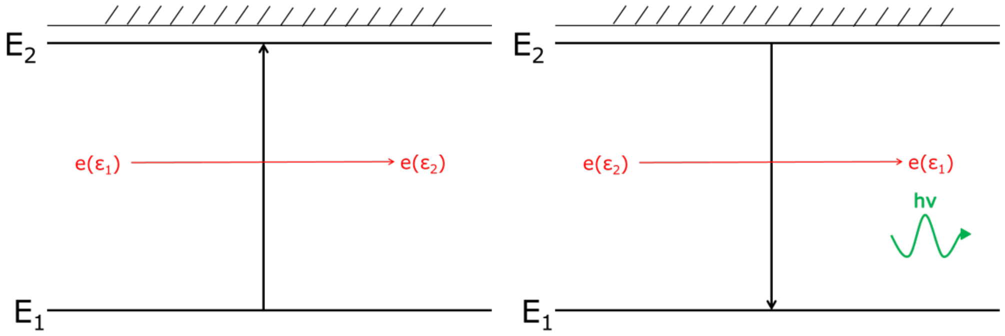

Figure 2.8: Schematic diagram of electron impact excitation atomic process (left) and of the electron impact de-excitation atomic process (right) [12].

$$A + e(\varepsilon_1) \rightarrow A^* + e(\varepsilon_2)$$ Equation 24

where $A*$ is an atom/ion in an excited state, A is the atom/ion in a lower energy state, e is a free electron and ε_1 and ε_2 are the kinetic energies of the free electron before and after the collision, where $\varepsilon_1 > \varepsilon_2$.

$$A^* + e(\varepsilon_1) \rightarrow A + h\nu + e(\varepsilon_2)$$ Equation 25

Photoabsorption is a process in which an atom or ion absorbs a photon and a bound electron is excited to a higher atomic state. The inverse process is spontaneous decay, in which an excited bound electron relaxes with the emission of a photon. Figure 2.9 is a schematic of both of these processes, while Equation 26 represents both photoabsorption and spontaneous decay [12].

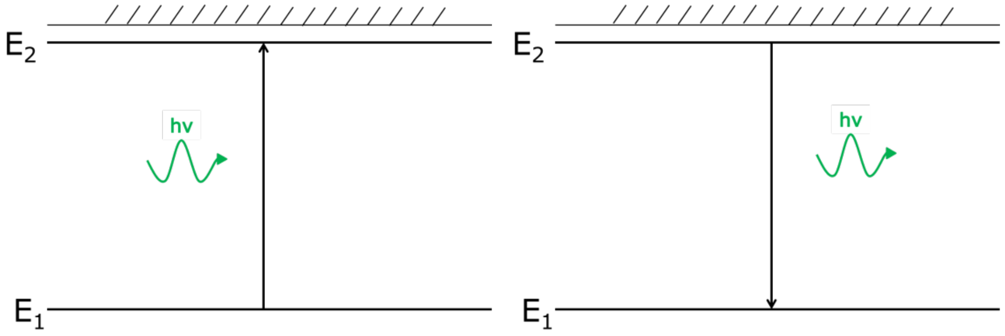

Figure 2.9: Schematic diagram of photoabsorption process (left) and of the spontaneous decay process (right) [12].

$$A + \gamma \leftrightarrow A^*$$ Equation 26

where A and $A*$ are described above and γ is the absorbed photon.

2.5 Equilibria in Plasmas

A plasma is considered to be in complete thermodynamic equilibrium (CTE) when the following four criteria [1] are met:

- All particles, electrons, neutral species and ions obey the Maxwell velocity distribution law.
- The population distribution amongst the states of any atom or ion is given by the Boltzmann formula.
- The intensity distribution of the radiation as a function of temperature and frequency is given by the Planck formula.
- The number of ions in a charge state z relative to the number of ions in the state (z-1) is given by the Saha equation.

If a plasma is in CTE the atomic processes within the plasma are balanced by their inverse processes, e.g. the rate of photoionisation is equal to the rate of radiative recombination. This is known as the principle of detailed balancing [13]. Plasmas in CTE are effectively never achieved in laboratory conditions, although suitable conditions may be approached in stellar interiors [5].

Due to these unobtainable conditions for laboratory plasmas further equilibrium models have been developed. And the most applicable models to laser produced plasmas are:

- Local Thermodynamic Equilibrium (LTE)
- Coronal Equilibrium (CE)
- Collisional Radiative Equilibrium (CRE)

Figure 2.10 shows the plasma parameter spaces for which these equilibrium models are valid. It also shows the critical density for both a CO_2 laser ($\sim 10^{19}$ cm^{-3}) and a Nd:YAG laser ($\sim 10^{21}$ cm^{-3}).

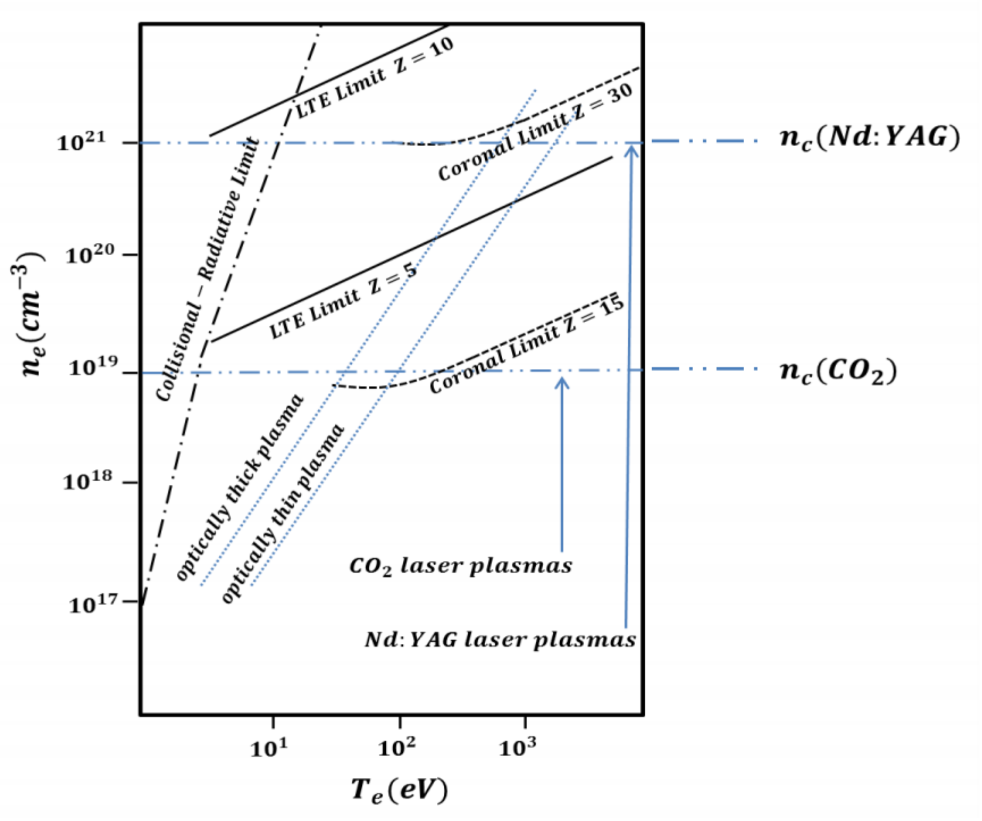

Figure 2.10: Validity of different plasma equilibrium models as a function of electron temperature and density (adapted from [14]). The dashed horizontal lines indicate the critical density for both CO_2 and Nd:YAG laser produced plasmas. The region of validity is on the labelled side of each curve.

2.5.1 Local Thermodynamic Equilibrium

Local thermodynamic equilibrium (LTE) is the name given to a plasma which is dominated by collisional excitation and de-excitation. When collisional de-excitation is dominant an ion in an excited state is more likely to return to the ground state through collisional de-excitation rather than spontaneous emission. LTE differs from complete thermal equilibrium in that the plasma need not have the same temperature everywhere, nor does it have the emission profile of a perfect black body. The following conditions must be met for LTE to hold [15]:

- The electron and ion distribution should obey a Maxwell-Boltzmann distribution written as:

$$f(v)dv = 4\pi n_e v^2 \left\{\frac{m_e}{2\pi k_b T_e}\right\} \exp\left\{-\frac{m_e v^2}{2k_B T_e}\right\} dv \qquad \text{Equation 27}$$

where *f(v)dv* is the density of the electrons with velocity between *v* and *v+dv*, n_e is the electron density and T_e is the electron temperature.

- The electron density should be sufficiently high that the ratio of collisional de-excitation to radiative decay rates is greater than 10:1 [16]. McWhirter [15] derived the following relationship between electron density and temperature to check this ratio:

$$n_e \gg 10^{19}(T_e)^{\frac{1}{2}}(\Delta E)^3 \qquad \text{Equation 28}$$

where n_e is the electron density (cm^{-3}), T_e is the electron temperature in electron volts and ΔE is the transition energy, again in electron volts [5].

2.5.2 Coronal Equilibrium

Coronal equilibrium (CE) is used to describe plasmas with a low electron density (typically $<10^{12}$ cm^{-3}), such as those found in the outer regions of stars (the corona). As collision rates scale with electron density the collisional excitation rate in CE plasmas is low and thus the spontaneous decay lifetimes of electrons in excited states tend to be shorter than the time between collision events. Consequently the majority of the ions in the plasma are in their ground states. The low rate of collisional processes can be attributed to the fact that collision rates scale with density. In CE plasmas radiation emitted from species within the plasma is not reabsorbed as it travels through it, signalling that photoexcitation and photoionisation are both negligible. Thus we can assume that collisional processes can excite the atoms and ions but, given the low electron density, rarely de-excite them.

2.5.3 Collisional Radiative Equilibrium

Collisional radiative equilibrium (CRE) is the name given to the model that describes the intermediate state between LTE and CE (typically $n_e \approx 10^{19} - 10^{21}$ cm^{-3}) [14]. Here both collisional and radiative processes have to be taken into account. The following conditions must be satisfied in order for CRE to hold:

- The velocity distribution of the electrons must be Maxwellian to ensure that the electron-electron relaxation time is smaller than the electron heating time.
- The population density of ions of charge Z+1 must not change significantly during the period when the quasi-steady state population distribution is being established among the ions of charge Z.
- The plasma must be optically thin to its own radiation.

For a quite high temperature plasma in collisional radiative equilibrium Colombant and Tonon [14] have shown that for $T_e > 30\,eV$, $z \sim [A.T_e(eV)]^{\frac{1}{3}}$ where z is the dominant ion stage and A is the atomic number of the target metal. They have also shown that, assuming collisional radiative equilibrium to pertain in a plasma, the electron temperature can be approximated by [14]:

$$\mathrm{T(eV)} \approx 5.2 \times 10^{-6} m^{\frac{1}{5}} (I\lambda^2)^{\frac{3}{5}} \qquad \text{Equation 29}$$

where *m* is the atomic mass, λ the laser wavelength (μm), and I the irradiance on target (W/cm^2). This approximation is seen to be valid for the duration of the laser pulse and provides an estimate of the initial plasma temperature.

2.6 Optical Transition Broadening

Observed spectral lines do not have an infinitesimally narrow line profile; they are broadened by several mechanisms. Those relevant to laser plasma spectroscopy are described below [17].

2.6.1 Natural Broadening

Natural broadening originates from the Heisenberg uncertainty principle which is described by the following expression for the energy spread of a quantum state with a spontaneous emission lifetime, $\tau = \Delta t$:

$$\Delta E \Delta t \geq \frac{\hbar}{2} \qquad \text{Equation 30}$$

Natural broadening yields a Lorentzian line profile and has a full width half maximum (FWHM) given by Equation 31 [5]:

$$\Delta v_N = 2\Delta v = \frac{1}{2\pi\tau}$$ Equation 31

2.6.2 Doppler Broadening

Doppler broadening arises from the so-called Doppler shift, which is the shift in the frequency of emitted light due to motion of an emitter with respect to the detector. If the distribution of particle velocities is Maxwellian this gives rise to a Gaussian line profile. The FWHM of this line profile is given by Equation 32:

$$\Delta v = 7.16 \times 10^{-6} \lambda_0 \sqrt{T_a/m_a}$$ Equation 32

Where v_0 (Hz) is the central frequency, T_a (K) is the temperature of the emitting atom and m_a (kg) is its mass [5].

2.6.3 Pressure (Stark) Broadening

Stark broadening has two contributions one due to collisions with highly mobile electrons in the plasma and another due to the residual ion microfield. In dense laser produced plasmas it is the former that tends to dominate. In much the same way that the lifetime of an upper state is progressively shortened by collisions between atoms as the pressure is increased in a gas discharge, the excited state of a transition decays more rapidly as the plasma density, and consequently the electron-atom or electron-ion collision frequency, increases. By appropriate analysis of the line profile the electron density may be extracted from the Stark component of the full experimental line profile. In laser plasmas the Stark broadening contribution to the line width far exceeds the natural line width. The full width at half maximum (FWHM) of a Stark broadened line is given by Equation 33:

$$\Delta\lambda_{width} = 2\omega\left(\frac{n_e}{10^{16}}\right) + 3.5A_i\left(\frac{n_e}{10^{16}}\right)^{\frac{1}{4}}\left[1 - 1.2{N_D}^{-\frac{1}{3}}\right]\omega\left(\frac{n_e}{10^{16}}\right)$$ Equation 33

Where ω is the Stark broadening parameter, n_e is the electron density (cm^{-3}), A_i is the ion broadening parameter and N_D is the number of particles in the Debye sphere [5].

Since Stark broadening is dominated by electron collisions the second term in Equation 33, namely the residual ion field contribution to Stark broadening, is usually omitted and we are left with the following simple linear equation for the Stark broadened full width at half maximum FWHM [5], [16] :

$$\Delta\lambda_{width} = 2\omega\left(\frac{n_e}{10^{16}}\right) \qquad \text{Equation 34}$$

2.6.4 Instrumental Broadening

If a monochromatic light source with a single narrow spectral line is passed through a perfect spectrometer then the output of the spectrometer should be identical to the input and an undistorted line should be recorded. However, in reality no spectrometer is perfect and it will make an additional broadening contribution to each discrete spectral line. In practice it is found that a Gaussian profile is a good approximation to the instrumental function for grating spectrometers.

When light is passed through the slit of a real spectrometer and focused onto a plane it is found that discrete spectral lines will normally have a Voigt profile, which is a convolution of Lorentzian and Gaussian profiles. In this, the simplest case, the Lorentzian profile will have originated from natural broadening of the atomic lines and the Gaussian profile will have originated from instrumental broadening due to the spectrometer. These and further broadening mechanisms are described below.

A Lorentzian and Gaussian profile can be represented by Equation 35 [18] and Equation 36 [19] respectively, the variable *x* in both of these cases is given by Equation 37 ;

$$L = \frac{1}{1 + x^2} \qquad \text{Equation 35}$$

$$G = e^{-(\ln(2))x^2)} \qquad \text{Equation 36}$$

$$x = \frac{p_0 - p}{\frac{w}{2}} \qquad \text{Equation 37}$$

where *w* is the full width at half maximum (FWHM), p_0 is the position of the line intensity maximum and p is any arbitrary position along the x axis. An example of both a Lorentzian and Gaussian profile, as well as their convolution, is shown in Figure 2.11, in which the convoluted Voigt profile has been normalised to its maximum to allow easier comparison between the line profiles.

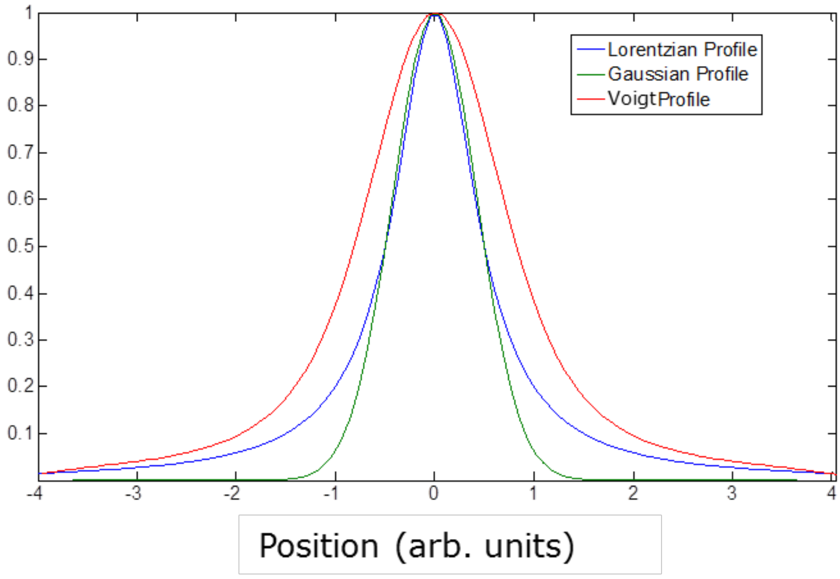

Figure 2.11: Sample Lorentzian, Gaussian and corresponding Voigt profiles. The x-axis corresponds to the reduced coordinate 'x' in equation 36 above.

2.7 Laser Induced Breakdown Spectroscopy

Laser induced breakdown spectroscopy (LIBS) exists in a number of formats (e.g., single or double pulse, UV-Vis-NIR or VUV) and is used in many environments (e.g., in air, other gases at high pressure or in liquids) [20]–[23]. In this thesis LIBS is employed in vacuo, for the generation of calibration curves from certified reference materials. These calibration curves allow the limit of detection, the ultimate figure of merit for the technique, to be extracted from experimental results.

The IUPAC definitions of the limit of detection, expressed as either a concentration, c_L, or as a quantity, q_L, is calculated from the smallest signal, x_L, which can be detected with reasonable certainty for an analytical technique. The value of x_L is given by the equation [24]

$$x_L = \bar{x}_{bi} + ks_{bi} \qquad \text{Equation 38}$$

where $\bar{x}_{bi}$ is the mean signal of a blank measure, s_{bi} is the standard deviation of the signal of a blank measure and k is a numerical factor, and in general, for LIBS a value of 3 is employed, chosen according to the desired confidence levels.

Through the generation of a calibration curve of an analyte signal intensity versus concentration we can extract the slope

$$m = \frac{\Delta x_L}{\Delta c_L} \qquad \text{Equation 39}$$

which gives the relationship between the analyte concentration and the signal it produces. Combining this with Equation 38 we obtain

$$c_L = \frac{c_{bi}}{m} + \frac{\sigma s_{bi}}{m} \qquad \text{Equation 40}$$

but c_{bi} is typically zero (no analyte concentration in a blank sample), so the value of the concentration limit becomes

$$c_L = \frac{k\sigma_{bi}}{m} \qquad \text{Equation 41}$$

more commonly written as

$$L.O.D. = \frac{3\sigma_{bi}}{S} \qquad \text{Equation 42}$$

Where σ_{bi} is the standard deviation of the background signal and S is the slope of the calibration plot (i.e., $k = 3\ and\ m = S$) in Equation 40.

2.8 Beam Shaping Optics

2.8.1 Biprism

A biprism is a triangular prism with a vertex angle which is, usually, between 179° and 180°. Biprisms were devised by Fresnel as a wave front splitting system which could be used to observe interference from a single source. However they can also be employed as beam splitters, which is the case in this thesis.

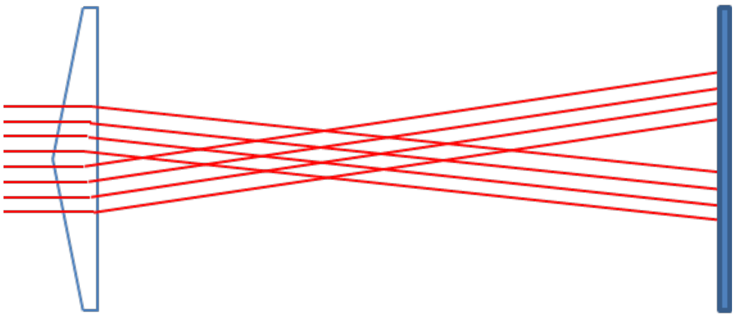

Figure 2.12: Biprism beam shaping. In the case of this work the beam diameter is 10 mm. It is centred by measuring the far field spot intensities.

Figure 2.13 on the following page shows the deflection of a collimated laser beam as it passes through a biprism, this deflection can be calculated using Equation 43 [25],

$$\delta = (n-1)\alpha \qquad \text{Equation 43}$$

where δ is the deflection of the beam in radians, *n* is the refractive index of the biprism and α is the biprism angle in radians.

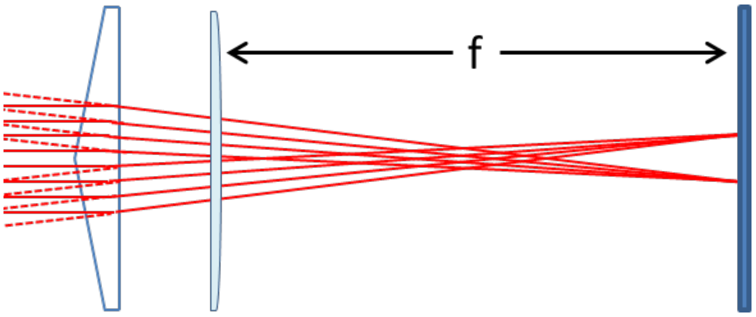

Figure 2.13: Biprism with focusing provided by a plano-convex lens..

Using a combination of trigonometry and Equation 43 an expression for the separation between the two beams at a distance *L* can be derived.

$$d_r = 2Ltan[(n-1)\alpha] \qquad \text{Equation 44}$$

When a lens is placed after the biprism Equation 44 becomes.

$$d_r = 2ftan[(n-1)\alpha] \qquad \text{Equation 45}$$

where *f* is the focal length of the lens and d_r is now the separation between the two focal spots.

2.8.2 Axicon

An axicon can be defined as either a plano-conical lens or a rotationally symmetric prism which in turn can be either convex or concave.

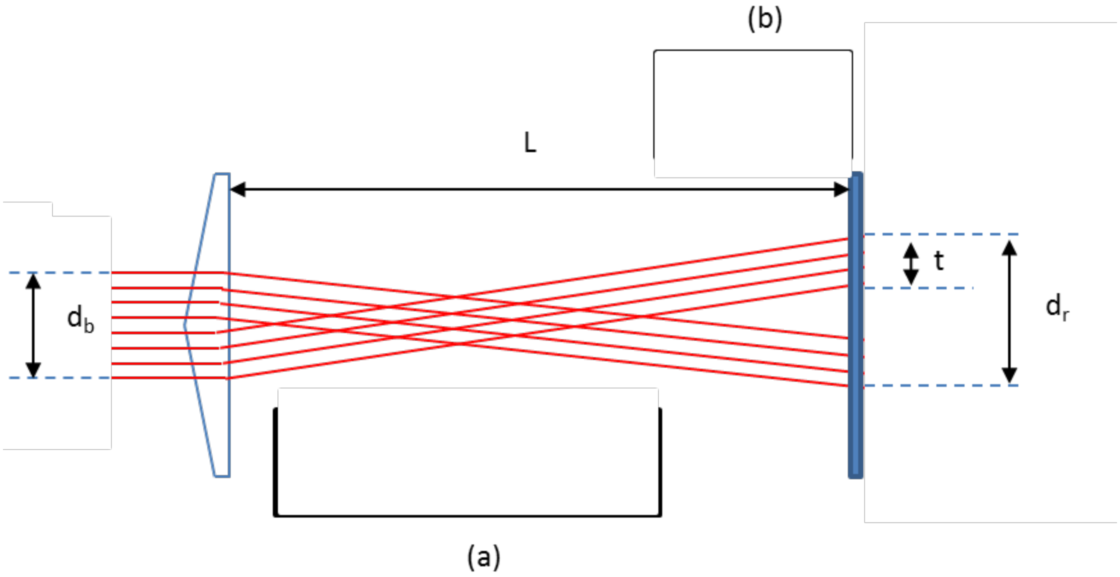

Figure 2.14: Axicon beam shaping.

Axicons create two areas of interest along the optic axis, (a) a long region of almost constant intensity and (b) an area of annular intensity distribution in the far field. The beam formed within the area marked (a) is known as a Bessel beam. An ideal Bessel beam is a beam with an intensity profile that remains constant in the plane normal to the propagation axis 'z' of the beam, as the beam propagates. This constant intensity profile leads to ideal Bessel beams being described as being diffraction free [26]. Although a diffraction free beam may seem to violate diffraction theory, non-diffracting solutions exist for the free space wave equation, an example of which is given by Equation 46 [26]:

$$E(x, y, z \geq 0, t) = \exp\left[i(\beta z - \omega t)\right] \int_0^{2\pi} A(\varphi) \exp[i\alpha(x\cos\varphi + y\sin\varphi)]\, d\varphi \qquad \text{Equation 46}$$

Where $\alpha^2 + \beta^2 = \left(\frac{\omega}{c}\right)^2$ and $A(\varphi)$ is an arbitrary complex function of φ. This field is said to be non-diffracting as its time averaged intensity profile at all values of positive z is equal to its time averaged intensity profile at z = 0 [26]:

$$I(x, y, z \geq 0) = \frac{1}{2}|E(r, t)|^2 = I(x, y, z = 0) \qquad \text{Equation 47}$$

The only non-diffracting field having axial symmetry is one in which $A(\varphi)$ is independent of φ; such a field is given by Equation 48:

$$\begin{aligned} &E(r, t) \\ &= \exp\,[i(\beta z - \omega t)] \int_0^{2\pi} \exp[i\alpha(xcos\varphi + ysin\varphi)] \frac{d\varphi}{2\pi} \qquad \text{Equation 48} \\ &= \exp\,[i(\beta z - \omega t)] J_0(\alpha\rho) \end{aligned}$$

Here $\rho^2 = x^2 + y^2$ and J_0 is a Bessel function of the first kind. When $\alpha = 0$ the solution to equation 45 is simply a plane wave, but when $0 < \alpha < \frac{\omega}{c}$ the solution is a non-diffracting beam with an intensity decays at a rate inversely proportional to $\alpha\rho$. The central peak of a Bessel beam and each of its surrounding rings each contain the same energy. It would therefore require an infinite amount of energy to fill a plane with a Bessel beam, for this reason ideal Bessel beams cannot be formed [26].

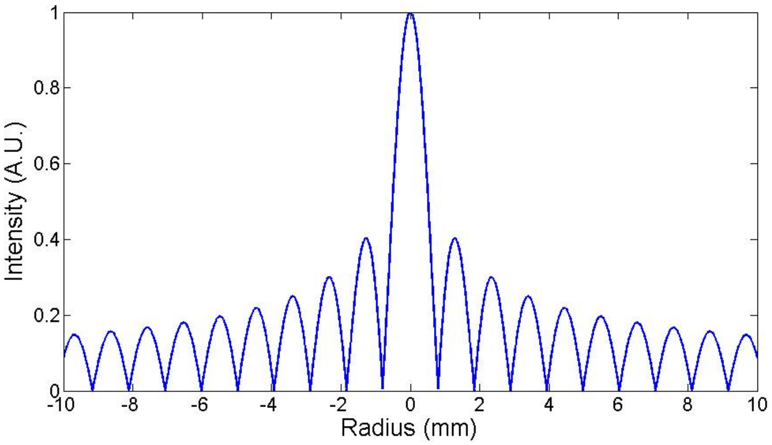

Figure 2.15: Intensity profile of an ideal Bessel beam showing the decrease in intensity with radius of the Bessel beam.

However approximations of Bessel beams may be formed over a finite area. One such approximation is formed when a Gaussian beam is passed through an axicon. This approximation is known as a Bessel-Gauss beam and is formed in the region marked (a) in Figure 2.14. The length of the region in which the Bessel-Gauss beam is formed is the depth of focus (DOF) of the axicon and is given by Equation 49.

$$DOF = \frac{R}{(n-1)\alpha}$$

Equation 49

Where *R* is the radius of the beam passing through the axicon. On the other hand annulus formation is defined by Equation 50 and Equation 51. The thickness, *t*, of the annulus remains constant as the diameter, d_r, increases while moving along the optic axis, *L*:

$$t = \frac{d_b}{2}$$

Equation 50

$$d_r = 2Ltan[(n-1)\alpha]$$

Equation 51

Where *α* is the vertex angle of the axicon and *n* is the refractive index of the axicon. This annulus is formed beyond the depth of focus of the axicon [27].

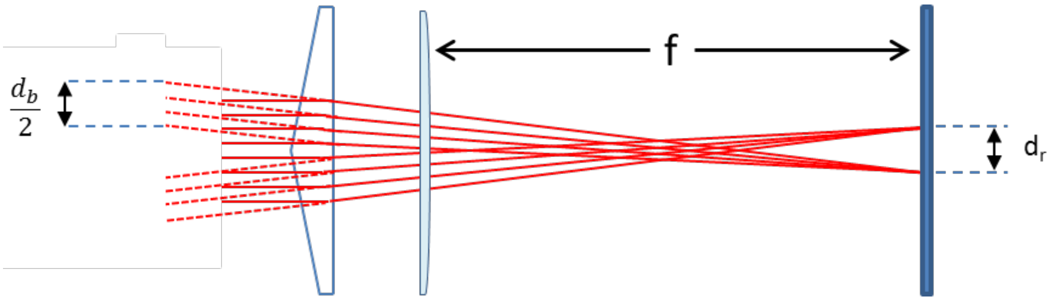

Figure 2.16: Axicon and lens focusing schematic.

When a lens is placed after an axicon, as shown in Figure 2.16, the laser beam can be considered as a ring of virtual sources which has a diameter of half of the input beam diameter. These virtual sources are then focused down by the lens after passing through the axicon. This configuration allows the diameter of the ring being investigated to be varied by selection of the focal length of the lens. The outer diameter of the annulus produced from the set up in Figure 2.16 is given by Equation 52 [28].

$$d_r = 2ftan[(n-1)\alpha] \qquad \text{Equation 52}$$

Although the equations for the focused beam through a biprism and an axicon are identical, it is worth noting that due to the rotational symmetry of the axicon the beam profiles are very different, one yielding two point foci and the other yielding an annular focus.

2.8. Summary

In this chapter the basic theory of laser produced plasma is outlined. The evolution of stagnation layers has also been explained. The atomic processes which underpin plasma formation and the thermodynamic models which apply have been described. Line broadening mechanisms within laser produced plasma have been discussed and will be expanded upon, for plasma density extraction, in Chapter 3. Laser induced breakdown spectroscopy has been covered as have the optical components employed in this work to generate stagnation layers.

Bibliography

[1] P. K. Carroll and E. T. Kennedy, "Laser-produced plasmas," *Contemp. Phys.*, Vol. 22, no. 1, pp. 61–96, 1981.

[2] F. F. Chen, *Introduction to Plasma Physics*. New York: Plenum Press, 1974.

[3] R. E. Russo, "Laser Ablation," *Appl.Spectrosc.*, Vol. 49, no. 9, p. 14A–28A, Sep. 1995.

[4] D. R. Corson and P. Lorrain, *Electromagnetic Fields and Waves*. New York: Freeman, 1988.

[5] I. H. Hutchinson, *Principles of Plasma Diagnostics*, 2nd ed. Cambridge University Press, 2002.

[6] R. K. Singh and J. Narayan, “Pulsed-laser evaporation technique for deposition of thin films: Physics and theoretical model,” *Phys.Rev.B*, Vol. 41, no. 13, pp. 8843–8859, 1990.

[7] P. T. Rumsby, J. W. M. Paul, and M. M. Masoud, “Interactions between two colliding laser produced plasmas,” *Plasma Phys.*, Vol. 16, no. 10, p. 969, 1974.

[8] C. Fallon, P. Hayden, N. Walsh, E. T. Kennedy, and J. T. Costello, “The Effect of Wedge Angle on the Evolution of a Stagnation Layer in a Colliding Plasma Experiment,” *J. Phys. Conf. Ser.*, Vol. 548, no. 1, p. 12036, 2014.

[9] P. W. Rambo and J. Denavit, “Interpenetration and ion separation in colliding plasmas,” *Phys. Plasmas*, Vol. 1, no. 12, pp. 4050–4060, 1994.

[10] F. Chen, *Introduction to Plasma Physics and Controlled Fusion*. Springer U.S., 1984.

[11] P. Hough, C. McLoughlin, S. S. Harilal, J. P. Mosnier, and J. T. Costello, “Emission characteristics and dynamics of the stagnation layer in colliding laser produced plasmas,” *J. Appl. Phys.*, Vol. 107, no. 2, p. 24904, 2010.

[12] D. Salzmann, *Atomic Physics in Hot Plasmas*. New York: Oxford University Publishers, 1998.

[13] J. A. M. van der Mullen, “On the atomic state distribution function in inductively coupled plasmas—I. Thermodynamic equilibrium considered on the elementary level,” *Spectrochimica Acta Part B: Atomic Spectroscopy*, Vol. 44, no. 11. pp. 1067–1080, 1989.

[14] D. Colombant and G. F. Tonon, “X-ray emission in laser-produced plasmas,” *J. Appl. Phys.*, Vol. 44, no. 8, pp. 3524–3537, 1973.

[15] R. W. P. McWhirter, *Plasma Diagnostic Techniques*. Acedemic Press, 1965.

[16] H. R. Griem, “Validity of Local Thermal Equilibrium in Plasma Spectroscopy,” *Phys.Rev.*, Vol. 131, no. 3, pp. 1170–1176, 1963.

[17] H. R. Griem, *Principles of Plasma Spectroscopy*. Cambridge University Press, 2005.

[18] E. W. Weisstein, “Gaussian Function,” *MathWorld--http//mathworld.wolfram.com/GaussianFunction.html*, 2019.

[19] E. W. Weisstein, “Lorentzian Function,” *Mathworld, http//mathworld.wolfram.com/LorentzianFunction.html*, 2019.

[20] D. N. Stratis, K. L. Eland, and S. M. Angel, “Dual-Pulse LIBS Using a Pre-ablation Spark for Enhanced Ablation and Emission,” *Appl. Spectrosc.*, Vol. 54, no. 9, pp. 1270–1274, 2000.

[21] D. Sun, Y. Ma, Y. Wang, M. Su, Q. Lu, and C. Dong, “Determination of the limits of detection for aluminum-based alloys by spatially resolved single- and double-pulse laser-induced breakdown spectroscopy,” *Anal. Methods*, Vol. 10, no. 22, pp. 2595–2603, 2018.

[22] S. S. Zehra, J. T. Costello, P. Nicolosi, and P. Hayden, “Time-integrated and time-resolved VUV LIBS: a comparative study,” in *Proc.SPIE*, 2018, Vol. 10674, no.

[23] D. A. Cremers, L. J. Radziemski, and T. R. Loree, “Spectrochemical Analysis of Liquids Using the Laser Spark,” *Appl. Spectrosc.*, Vol. 38, no. 5, pp. 721–729, 1984.

[24] A. D. McNaught and A. Wilkinson, *Compendium of Chemical Terminology*, 2nd ed. Oxford: Blackwell Scientific Publications, 1997.

[25] E. Hecht, *Schaum’s Outline Series Theory and Problems of Optics*. New York: McGraw Hill, 1975.

[26] J. Durnin, J. J. Miceli, and J. H. Eberly, “Diffraction-free beams,” *Phys.Rev.Lett.*, Vol. 58, no. 15, pp. 1499–1501, 1987.

[27] M. Rioux, R. Tremblay, and P. A. B\'elanger, "Linear, annular, and radial focusing with axicons and applications to laser machining," *Appl.Opt.*, Vol. 17, no. 10, pp. 1532–1536, 1978.

[28] M. Duocastella and C. B. Arnold, "Bessel and annular beams for materials processing," *Laser Photon. Rev.*, Vol. 6, no. 5, pp. 607–621, 2012.

3. Experimental Systems and Analysis Techniques

3.1. Laser and Vacuum Systems

3.1.1 Surelite Nano Second Laser

The laser used for this work was a Continuum Surelite^{TM} model III-10 [1], which is a Q-switched Nd:YAG system that can produce laser pulses with a width of 4-6 ns FWHM carrying an energy of up to 800mJ per pulse, at a pulse repetition frequency up to and including 10 Hz. In the work reported in this thesis the fundamental wavelength of the laser, i.e., 1064 nm, was used; although the lasers can also operate at the 2nd, 3rd and 4th harmonic wavelengths of 532 nm, 355 nm and 266 nm respectively. The pulses generated by this laser are linearly polarized and exhibit a Gaussian beam profile. The laser was operated in single shot mode, controlled by the laser synchronisation electronics described in section 3.1.2. The laser pulses were attenuated to the levels required for various experiments using the combination of a half wave plate and a cube polariser, as shown in sections 3.2.2. and 3.3.2.

The principle of Q-switching is to keep the gain of the resonator low whilst the gain medium is being pumped. Once the gain medium achieves population inversion the Quality Factor of the resonator is restored to a high value allowing the lasing to take place. The short duration of the switching process allows for pulses on the order of nano seconds to be produced. Q-switching can be effected in either passive or active mode. In passive mode a saturable absorber, such as Cr:YAG, is used within the resonator, in active mode an electronic modulator is used, usually an acousto-optic or an electro-optic device.

The Surelite laser used for these experiments employs active Q-switching to produce laser pulses. The combination of a Pockels cell, quarter waveplate and a polariser are used to control the Q of the resonator. A Pockels cell is an optically active crystal with a birefringence that is voltage controlled. At the quarter wave or '$1/4\lambda$' voltage a phase shift of 90 degrees is introduced between the ordinary and extraordinary rays passing through the cell. Hence, an initially linearly polarised beam is converted to a circularly polarised beam. In operation, the laser medium is pumped, in this case by a pair of flash lamps, creating a population inversion. The Q-switch prevents optical feedback by resonator until the population inversion within the laser medium has reached its maximum value. Once that has occurred, the Q-switch is triggered and laser oscillation may take place.

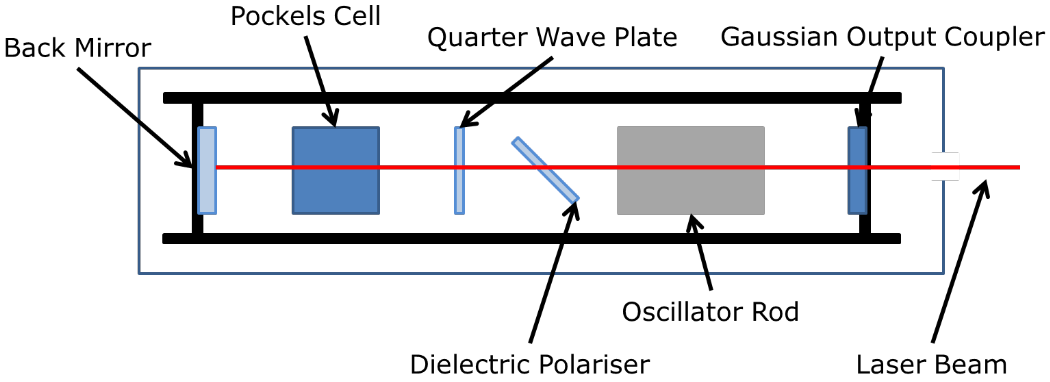

Figure 3.1: Continuum Surelite^{TM} III-10 Laser Schematic

In greater detail, the beam propagates within the cavity making a double pass through the Pockels cell and quarter wave plate. With no bias on the Pockels cell the cavity remains closed, the original horizontally polarised beam is rotated through 90 degrees by the double pass through the ¼ wave plate and is therefore rejected by the polariser. When a high (¼ wave) voltage (typically 3 kV for 1064 nm with a KDP crystal) is applied to the birefringent Pockels cell crystal, the laser field undergoes a double pass through the Pockels cell and a double pass through the ¼ wave plate so that the beam polarisation is returned to its original horizontal state and hence it is no longer rejected by the polariser and is allowed to exit the cavity, via the output coupler. A schematic of the laser is show in Figure 3.1. The cavity is built on a graphite structure to ensure thermal and mechanical stability.

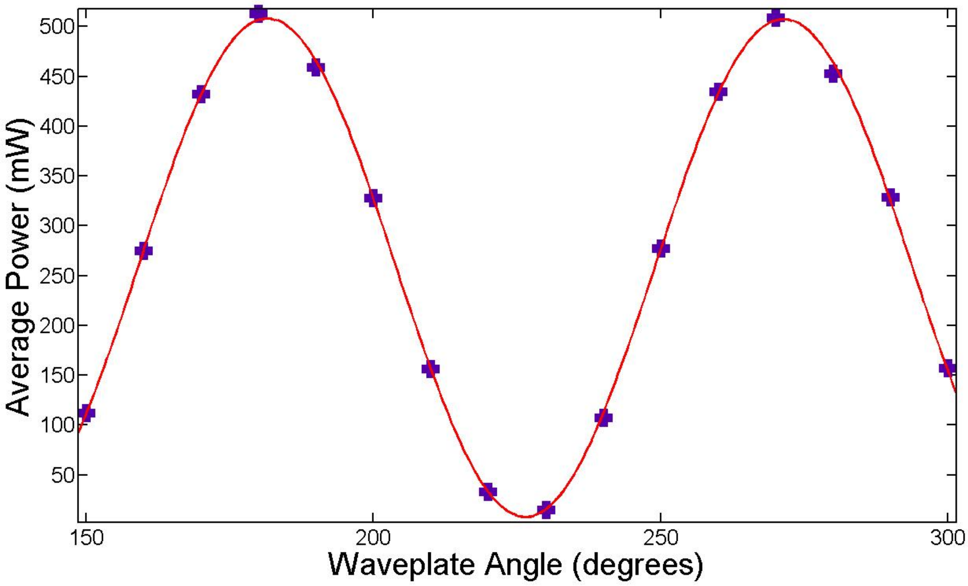

Figure 3.2: Measured variation in average laser power delivered to the target with half-waveplate angle for a pair of attenuators.

In order to undertake realistic LIBS experiments, where minimal target damage is necessary, the output of the laser requires attenuation. This attenuation is carried out using a combination of a half-wave plate and a beam splitting cube polariser. In fact, for all the presented experiments, two attenuators were used in each experimental set up in order to ensure fine control over the laser pulse energy. The first attenuator is used to bring the average laser power down to the few hundred milliwatt level (from typically 8 watts). This output beam is then passed through a second attenuator array, which is used to vary the energy delivered to the target through rotation of its half-wave plate. The dependence of energy on half-wave plate angle for the second attenuator is shown in Figure 3.2.

3.1.2 Laser Synchronisation

Synchronisation of laser firing and data acquisition was by means of two delay generators (Quantum Composer Plus 9514 and Stanford Research Systems Inc. DG535) and two AND gates. An active low TTL signal running at 10Hz with a 10μs pulse width drives the laser flash lamps. When the acquire button is pressed on the computer a signal is sent to the iStar ICCD, the iStar then sends a TTL signal from its fire port. This signal is split and sent to both AND gates.

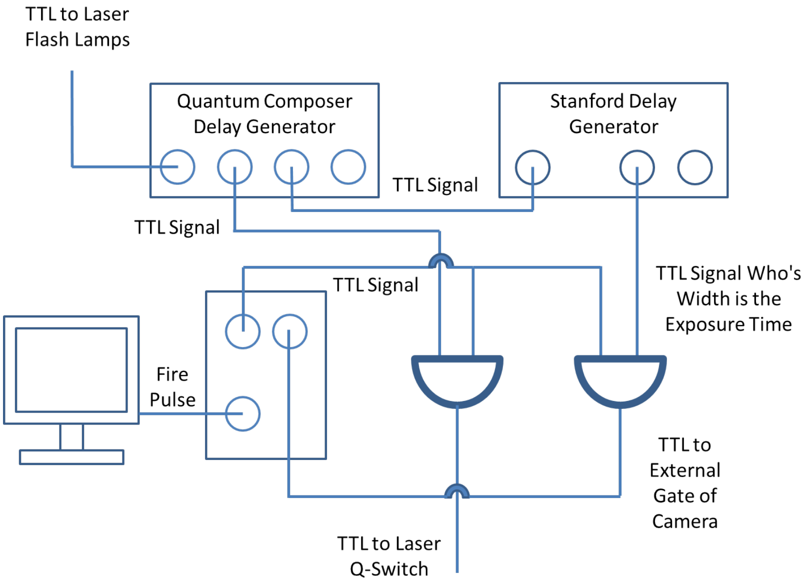

Figure 3.3: Electronic wiring diagram for synchronisation of the Surelite laser system and Andor iStar ICCD.

The first AND gate also has an active high TTL signal running at 10Hz with a 10µs pulse width input onto its other terminal, when TTL signals are present a 10µs pulse is passed to the laser activating the switch and allowing the laser to output a 6 ns optical pulse.

The second AND again receives the TTL signal from the camera fire port as well as a TTL pulse with a varying width and delay depending on the required acquisition; for time integrated measurements it has no delay from T_0 and a width on the order of microseconds whereas for time resolved measurements it has a selected delay from T_0 and a gate width on the order of nanoseconds.

Note: There is a 75ns delay between the triggering of the Q-switch and the laser pulse arriving at the target, T_0, this has been excluded from this discussion and the relevant figures for the sake of clarity. Figure 3.4 below shows a timing diagram illustrating the laser/camera pulse synchronisation.

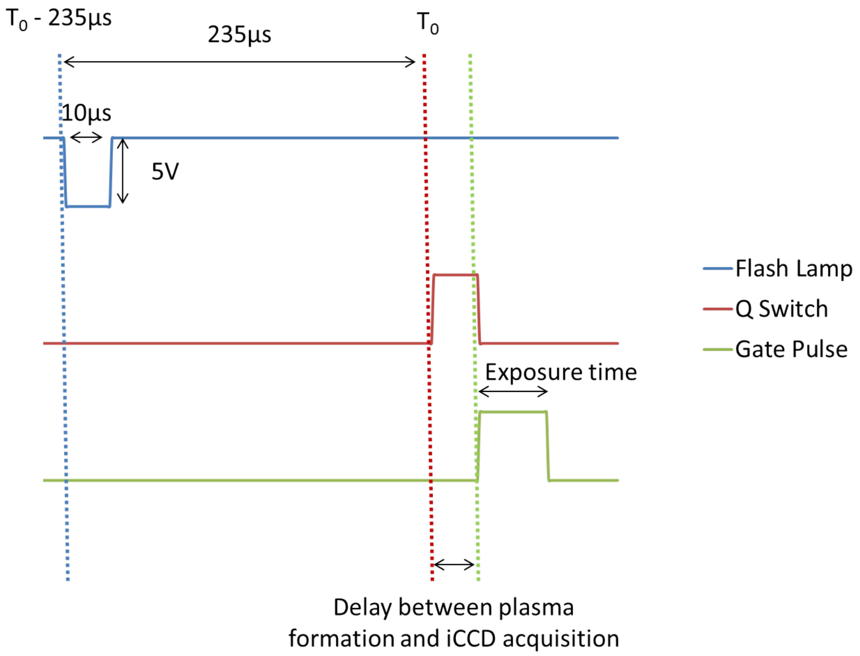

Figure 3.4: Timing diagram showing synchronisation of the laser and camera for imaging and spectroscopic experiments.

3.1.3 Vacuum System

To allow for stagnation layer generation the initial plasmas need to be created in a low pressure environment, which allows them to expand freely and collide. This low pressure environment was ensured by carrying out all experiments in a vacuum chamber from which the air was evacuated using a combination of a rotary and turbomolecular pump. The rotary pump is used to evacuate the air down to a pressure of $1x10^{-3}$ mbar at this point the turbomolecular pump is started allowing for pressures of below $1x10^{-6}$ mbar to be achieved.

Pressures were monitored using a combination of a Pirani gauge and a Penning gauge, the former used for measuring pressures above $1x10^{-4}$ mbar and the latter used for pressures between $1x10^{-4}$ and $1x10^{-9}$ mbar. The pressure inside the chamber was maintained at those values used for experiment using a variable leak valve.

3.1.4 Crater Profiles

In this work comparisons of plasma evolution, electron temperature, electron density, LIBS signal-to-background ratio (SBR) and LIBS limit-of-detection (LOD) will be drawn for three focusing geometries. These geometries are illustrated in sections 3.2 and 3.3; they consist of a single plasma, a stagnation layer formed between two seed plasmas and a stagnation layer formed at the centre of an annular plasma.

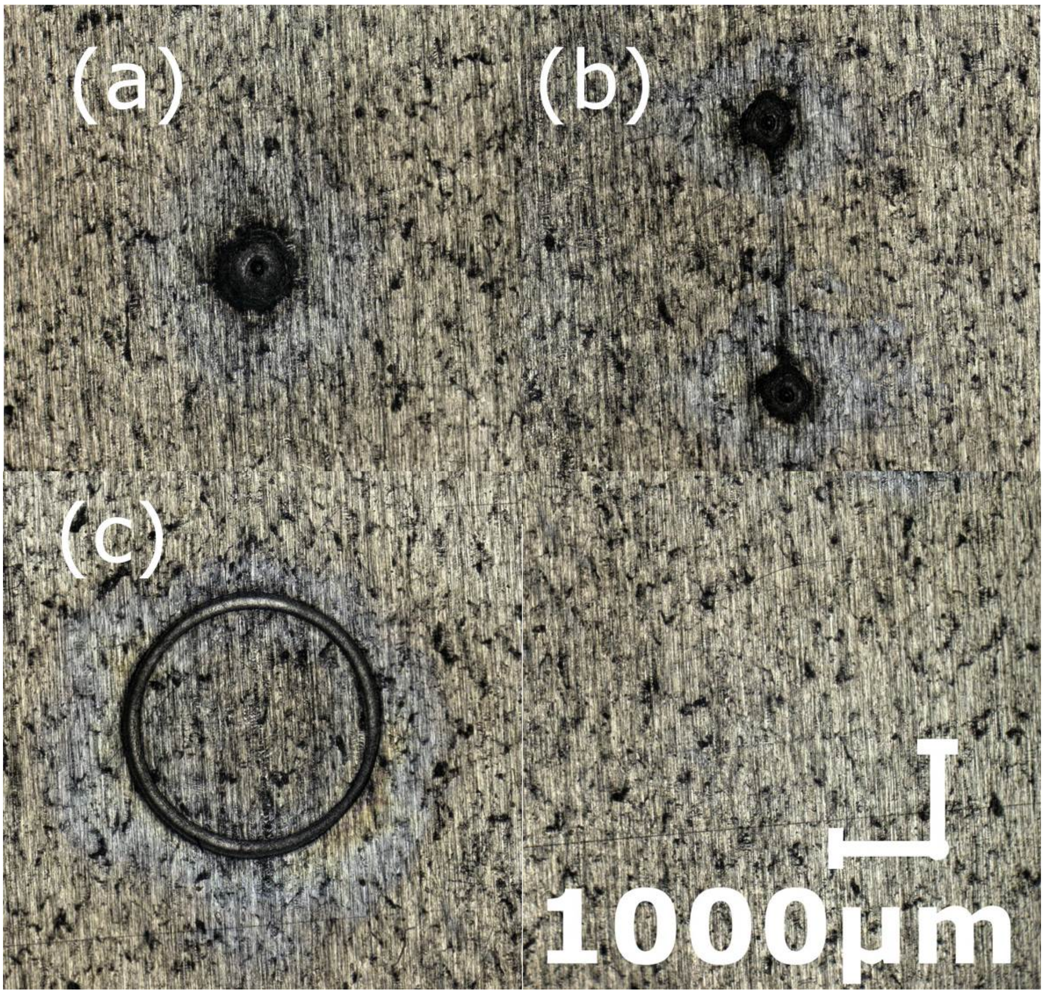

Figure 3.5: Composite image of the crater profile for each focussing geometry. (a) a single plasma plume, (b) a pair of seed plasmas and (c) an annular plasma.

Figure 3.5 is a composite image from images of each crater which were acquired using a Keyence VHX 5000 optical microscope. The craters were formed from ten laser shots, with a laser energy of 28mJ/pulse.

The power density for the annular focusing geometry was calculated using the area extracted using these images. Using the inside and outside diameters of 2.4mm and 2.0 mm respectively, the area is ~ 1.4 X 10^{-2} cm^2. For the single and dual colliding systems the theoretical minimum focal area was calculated for the fundamental frequency of the Nd:YAG laser and a 400 mm focal length lens.

The, diffraction limited, minimum $1/e^2$ diameter for a gaussian beam focused by a thin lens is given by the following formula.

$$w_0 = \frac{4\lambda f}{\pi D}$$

where λ is the wavelength of the light to be focused, f is the focal length of the lens and D is the diameter of the input beam. For the experimental parameters used in the single and dual colliding plasma experiments we have the following lower limit for focal spot size.

$$w_0 = \frac{4(1.064 \times 10^{-6})(0.4)}{\pi(0.1)}$$

$$w_0 = 54\,\mu m$$

The M^2 value for high energy nano-second pulsed Nd:YAG lasers is generally between 2 and 3. The M^2 value of the laser can be combined with this calculated focal spot diameter to yield the expected diameter

$$w_0{}' = w_0 \times M^2$$

$$w_0{}' = 54 \times 3\,\mu m$$

$$w_0{}' = 162\,\mu m$$

The pulse energy is divided equally between each seed beam for the dual colliding plasma experiment. Since the seed beams are halved in area, it is assumed that each gives rise to a focal spot area half that of the single (full) beam focal spot size. The measured pulse width is 6 ns. The focal spot areas for each geometry are given in table 3.1.

Table 3.1: Focal area (cm^2) of each focussing geometry

	Annular	Single	Dual Colliding
Focal Area (cm^2)	1.4x10^{-2} ± 20%	2.0x10^{-4} ± 20%	1.1x10^{-4} ± 20%

Table 3.2: Power densities (in W.cm^{-2}) for each focusing geometry.

	28 mJ	38 mJ	52 mJ
Axicon	3.3x10^{8} W.cm^{-2}	4.5Ex10^{8} W.cm^{-2}	6.1x10^{8} W.cm^{-2}
Biprism (per seed)	2.1x10^{10} W.cm^{-2}	2.9x10^{11} W.cm^{-2}	3.9x10^{11} W.cm^{-2}
Single	2.3x10^{10} W.cm^{-2}	3.2x10^{10} W.cm^{-2}	4.3x10^{10} W.cm^{-2}

The power densities given in Table 3.2 were used for all experiments carried out within this thesis.

3.2. Time and Space Resolved Imaging Setup

3.2.1 Andor iStar DH334T Intensified CCD

An Andor iStar DH334T [2] intensified charge coupled device (ICCD) with 1024x1024 pixels was used for the entirety of the work presented. Each pixel is 13 μm x 13 μm resulting in a total active image area of 13.31 mm x 13.31 mm for the chip. Before light reaches this chip it passes through the intensifier, which is an assembly of a photocathode, a micro channel plate (MCP) and a phosphor screen. The function of this intensifier assembly, as its name suggests, is to increase the number of photons falling onto the CCD relative to the number which enter the assembly, a schematic of which is shown in Figure 3.6. The photons incident onto the intensifier are first converted to electrons by a photocathode. These photons then pass through a MCP which multiples the number electrons with a gain that is dependent on the voltage applied across it. After the electrons are multiplied they collide with a phosphor screen, leading to the production of photons which then fall onto the CCD and an intensified image signal is registered.

The level of intensification achieved by an intensifier is given the term ‘gain’. Gain, as alluded to above, depends on the voltage applied across the MCP and is controlled using the Andor Solis^{TM} software. To allow for comparison of images acquired using different gain levels a gain curve was produced. The range of gain available to an iStar, varies from zero to four thousand.

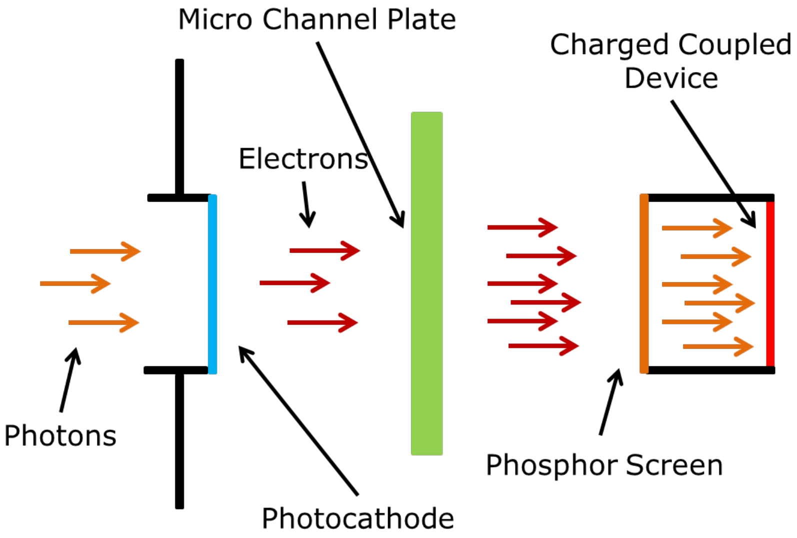

Figure 3.6: Schematic diagram of an ICCD.

To quantify this gain the sodium doublet at 589.0 nm and 589.6 nm were imaged through the Chromex 501s spectrometer at gain setting increments of two hundred between zero and four thousand. The intensity of both peaks, at every gain level, was divided by the intensity of the same peak at zero gain. The values from both peaks were then averaged to produce that data for Figure 3.7. From the y-axis of Figure 3.7 the factor by which a signal needs to be divided in order to be corrected for gain can be extracted.

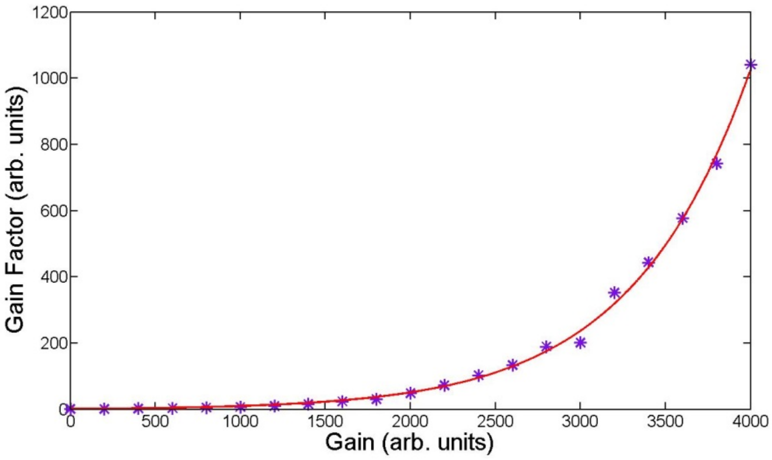

Figure 3.7: Gain response of the Andor iStar^{TM} ICCD.

Another parameter which needed to be calibrated was the magnification of the imaging setup. This calibration allows for plasma expansion dynamics to be studied, most notably expansion velocities. In order to identify the conversion between number of pixels, given by the camera software, and absolute length in millimetres, a transparent ruler with one millimetre graduations was backlit and its image was focused onto the ICCD using the collection optics which were used for all side on imaging experiments. The same scale finding technique was employed for all imaging set ups. Figure 3.8 contains the back lit image, in which the graduations are clearly identifiable.

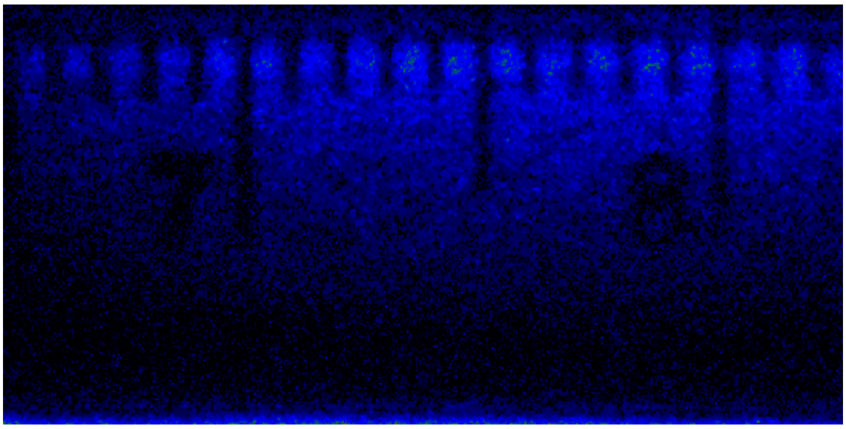

Figure 3.8: Image of a back lit, millimetre graduated ruler.

A partial vertical bin of the area containing the graduated marks was taken, which resulted in the intensity profile shown in Figure 3.9.

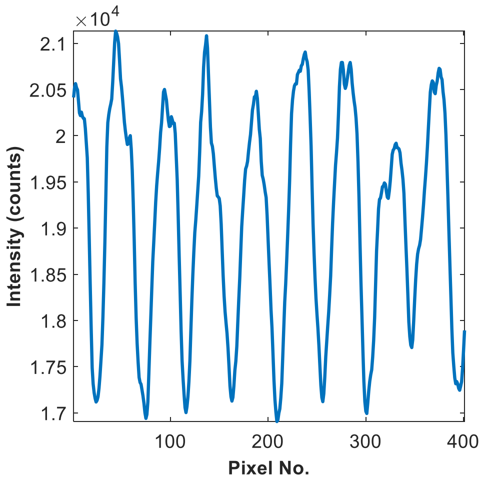

Figure 3.9: Partial vertical bin of Figure 3.8 used to calculate magnification of the imaging system.

The minima of this intensity profile are a result of the graduation marks on the ruler. The pixel number where these minima manifested were plotted against distance (mm), with the left most minimum point being taken as the origin. A plot of pixel number versus distance is shown in Figure 3.10. A linear fit to these points yielded a slope of 46 pixels per mm.

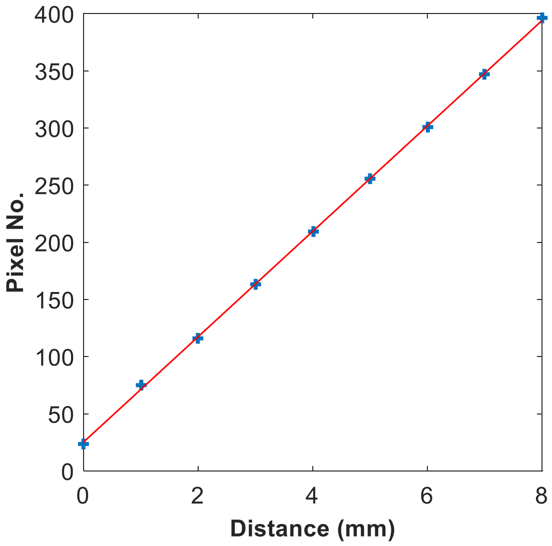

Figure 3.10: Calibration curve extracted from Figure 3.9.

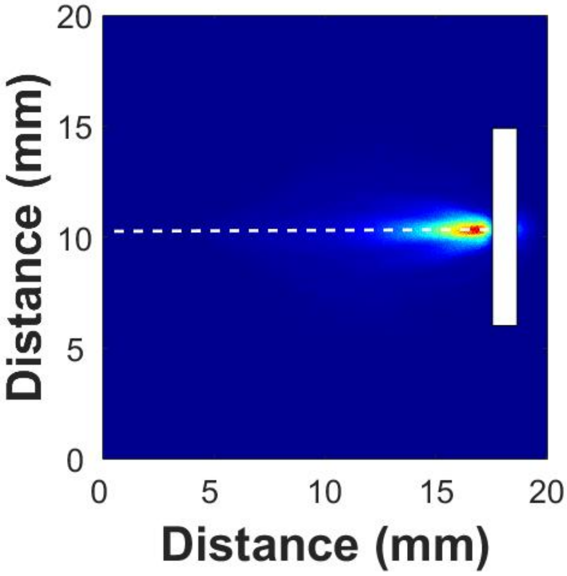

Figure 3.11: Example of lineout over laid on a time resolved image of a laser produced aluminium single plasma.

From imaging data the physical dimension and expansion dynamics of the plasma can be obtained by taking lineouts along the expansion direction (Figure 3.11). During this work the plume front position of the plasma was defined as the position at which the ICCD count dropped below 10% of its maximum value in the expansion direction normal to the target surface (Figure 3.12).

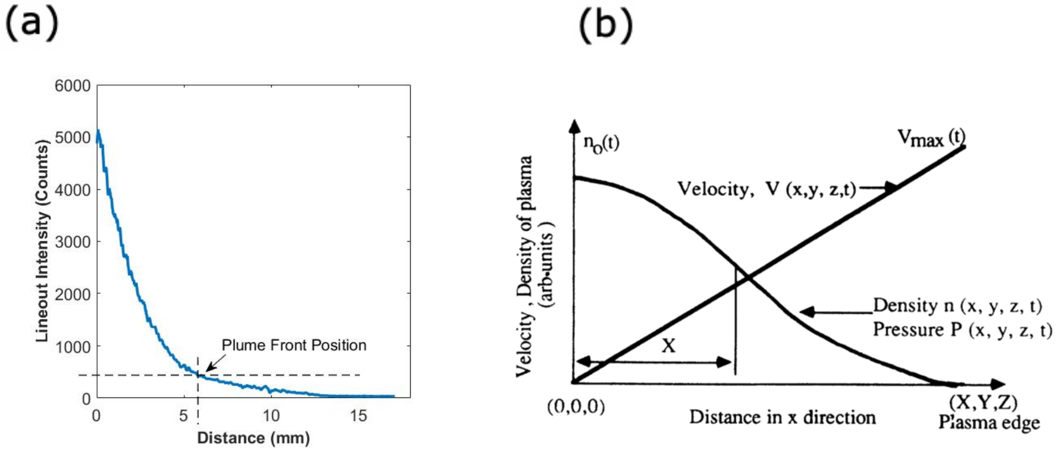

Figure 3.12: (a) Vertical bin of the lineout shown in Figure 3.11 from which plume front positions are taken. (b) Theoretical plasma (fluid) density profile taken from Singh and Narayan [3].

The emission profile in figure 3.12(a) exhibits a profile determined by the fall off in the density of emitting species in the plasma plume. As it is a broadband image, the profile is somewhat reflective of the whole plasma density. In this sense it can be compared with the theoretical density plot shown in figure 3.12(b) for the region away from the target surface where the density begins to fall off quickly. Differences are due to the fact that our data contains only a signal from excited species and only for a narrow range of charge states (mainly neutral to doubly charged).

3.2.2 Imaging Setup

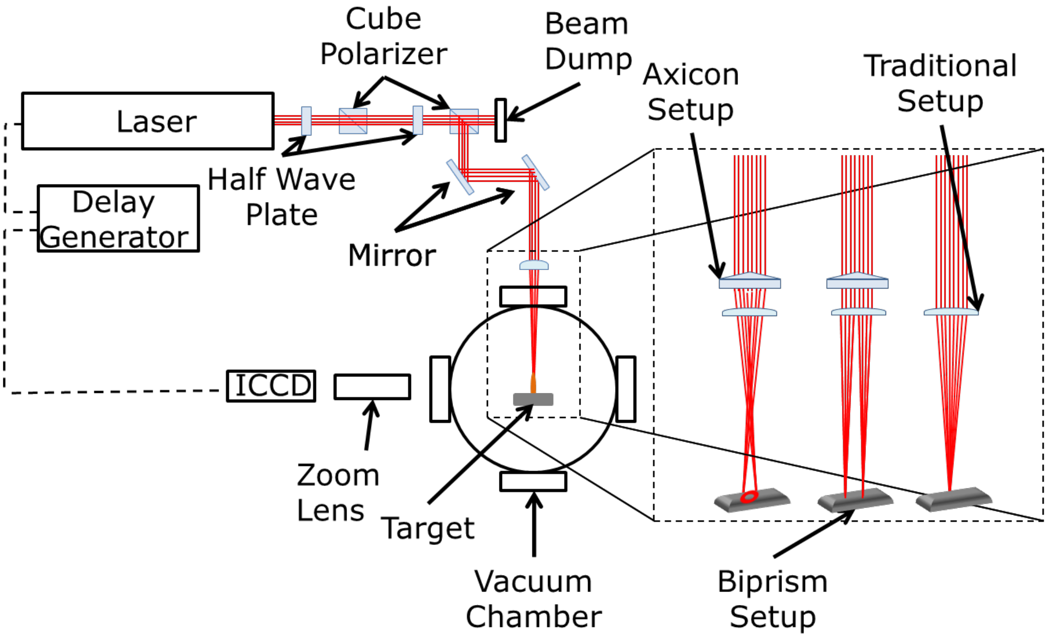

Figure 3.13: Side on time resolved imaging experimental set up, with exploded view of the three focusing geometries.

Both head on and side on imaging systems are shown in Figure 3.13 and Figure 3.14 respectively, the difference between the two being the off axis parabolic mirror through which allowed for head on imaging. An exploded view of the three focusing geometries is included in each figure. A rail system was used to ensure consistent placement of the axicon and biprism. Imaging experiments were carried out using the Andor iStar^{TM} ICCD with a gate width of 10ns. Camera saturation was avoided at early plasma lifetimes using neutral density filters, while at late times the gain of the camera was used to increase the signal to allow for evolution diagnostics.

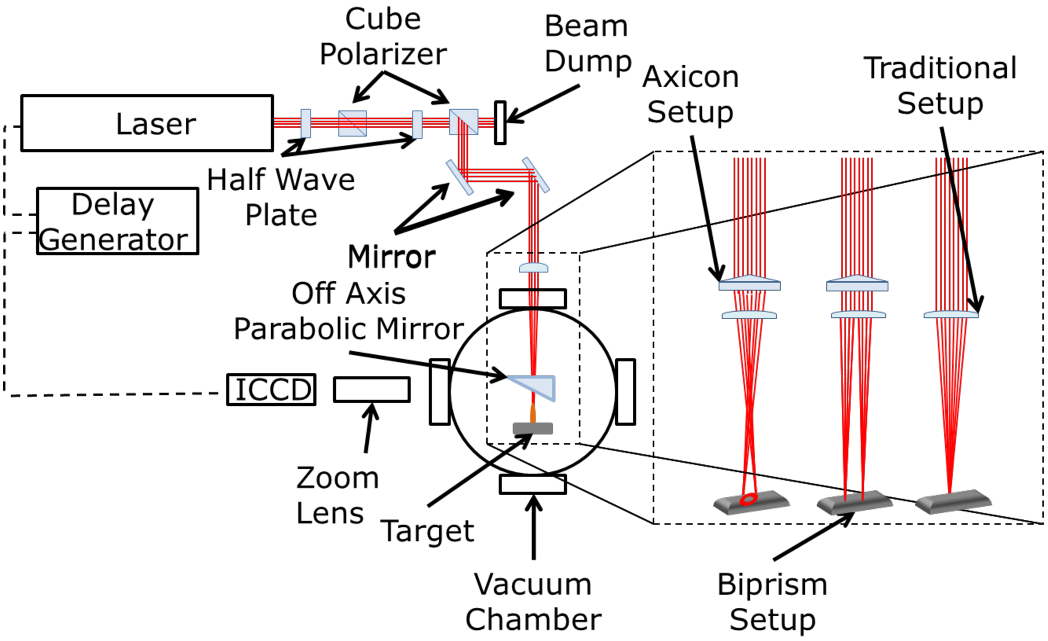

Figure 3.14: Head on time resolved imaging experimental set up, with exploded view of the three focusing geometries.

Head on imaging was achieved using a cutom drilled protected silver off axis parabolic (OAP) mirror. A schematic daigram of the mirror is given in Figure 3.15. The focusing laser beam was passed through a tapering hole drilled in the mirror, the beam then struck the target at its focal point, inducing a laser plasma which can be treated as a point source which radiates isotropically.

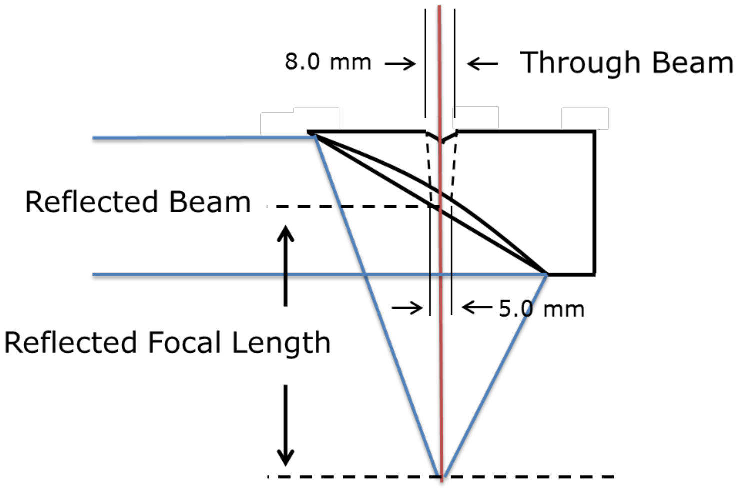

Figure 3.15: Drilled off axis parabolic mirror schematic.

The OAP was placed at the distance of its reflected focal length from the target, giving a reflected beam which is collimated. This collimated beam is then focused onto the target using the same zoom lens as the side on imaging case.

3.3. Time and Space Resolved Spectroscopy Setup

3.3.1 Chromex 501s Czerny Turner Spectrometer

The spectrometer used for all measurements was a 0.5m focal length Czerny Turner mount (Table 3.3). The entrance slit width for all measurements was set at 60µm, while a 1200 lines/mm diffraction grating, with a blaze wavelength of 400 nm providing a maximum resolution of 0.07 nm (FWHM) [4], was used for all experiments, which results in a spectral window of 22nm across the full width of the ICCD. The instrumental broadening was measured by passing radiation from a monochromatic light source, a He-Ne laser, through the spectrometer and onto the Andor iStar^{TM} ICCD which recorded the spectrum.

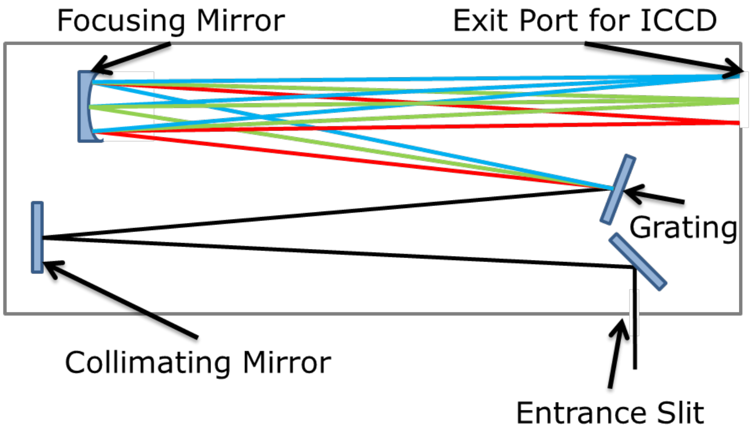

Figure 3.16: Schematic of a Chromex 501s Czerny Turner 0.5m spectrometer.

A Voigt profile was then fitted to the resulting spectral line, this Voigt profile was deconvolved and the instrumental broadening of the spectrometer was taken as the FWHM of the Gaussian component of the Voigt profile, giving a value of 0.16nm. Spectral resolution is usually measured by resolving a pair of close lying emission lines. We did not have such a spectrum available and so the resolution was taken as the equivalent spectral width of 3 pixels based on the Nyquist criterion that the highest spatial frequency in an image that can be reproduced by a CCD of pixel width p (mm) is $< 1/2p$ mm^{-1}. Hence one must sample at more than 2 pixels per spatial frequency cycle which is traditionally taken as 3 pixels. The equivalent spectral window width captured by the 1024-pixel width of CCD is 22 nm. Hence the 3 pixels 'sample' a spectral width of 3 x 22nm/1024 = 0.064 nm rounded up to 0.07 nm. This value is in good agreement with that supplied by the manufacturer, namely 0.07 nm.

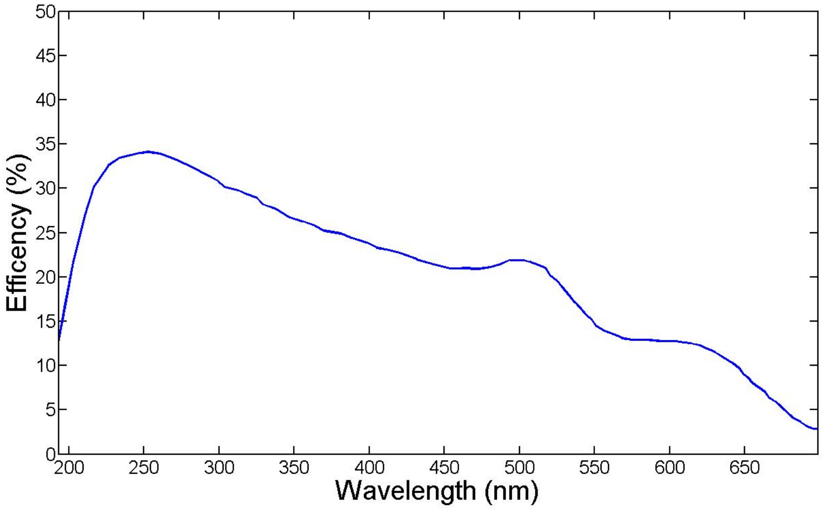

Figure 3.17: Quantum efficiency of the Chromex 501s Czerny Turner half metre spectrometer.

Table 3.3: Chromex 501s 0.5m focal length Czerny Turner spectrometer specifications.

Configuration	Czerny-Turner
Aperture Ratio	f/8
Wavelength Range	180-900 nm
Reciprocal linear dispersion	1.6 nm/mm
Resolution	~0.07 nm
Slit Width	10 – 2000 µm
Wavelength Accuracy	±0.15 nm
Grating	1200 grooves/mm
Focal Length	0.5 m

3.3.2 Atomic Emission Spectroscopy Setup

The experimental set ups used for head on and side on spectroscopy were practically identical to the systems used for imaging experiments. The only difference was that the light collected from the plasma was focused down onto the spectrometer slit rather than the ICCD, which was placed in the imaging plane of the spectrometer. The plasma plume imaging optics comprised a pair of lenses acting as a relay system. The light collecting lens was f/4 and was located at a distance 'f' from the plasma plume. The quite well collimated beam of light from this lens was incident on an f/8 lens and focused onto the spectrometer entrance slit so that an image of the plume was formed on it. This f/8 lens was chosen to match the aperture of the spectrometer. An iris placed just before this lens could be used to stop down the beam and increase the f/no of the system, improving depth of focus and avoiding any accidental overfilling of the grating.

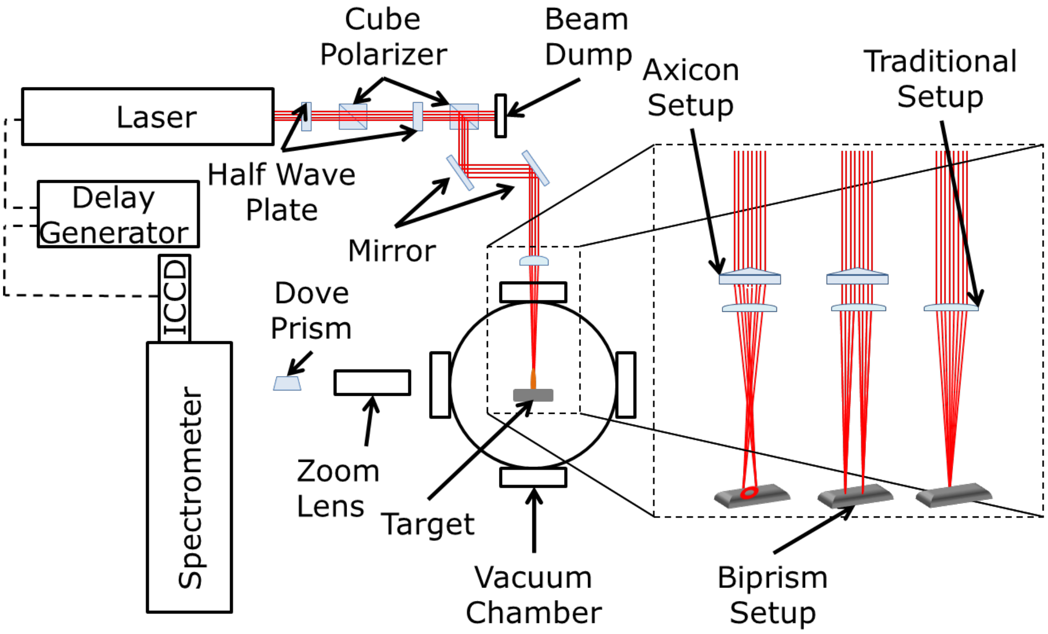

Figure 3.18: Side on time resolved spectroscopy experimental set up, with exploded view of the three focusing geometries.

For side on spectroscopic measurements a dove prism was inserted between the zoom lens and the spectrometer. The dove prism, when set at the correct angle, will rotate the image passing through it by ninety degrees. This allows the stagnation layer, or indeed a single plasma, to expand upwards, along the slit, adding space resolution to the measurements. This rotation is illustrated in Figure 3.19.

The experimental set up used for acquisition of LIBS spectra was identical to that used for side on spectroscopy, although the acquisition settings were not. These acquisition settings are outlined within the relevant results chapters. The focus here was on studying SBR and LOD for a single plume and the stagnation layers formed at the locus of the collision between two point plasmas and an annular plasma.

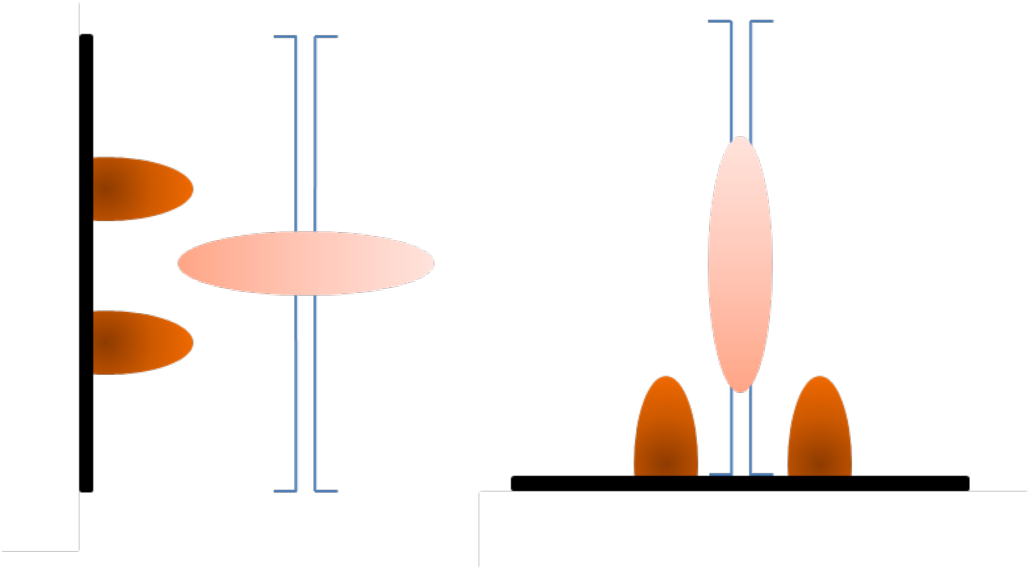

Figure 3.19: Schematic showing the rotation of a stagnation layer by a dove prism.

A dove prism was not used for the head on spectroscopy as rotation of the image would not have yielded any additional space resolution.

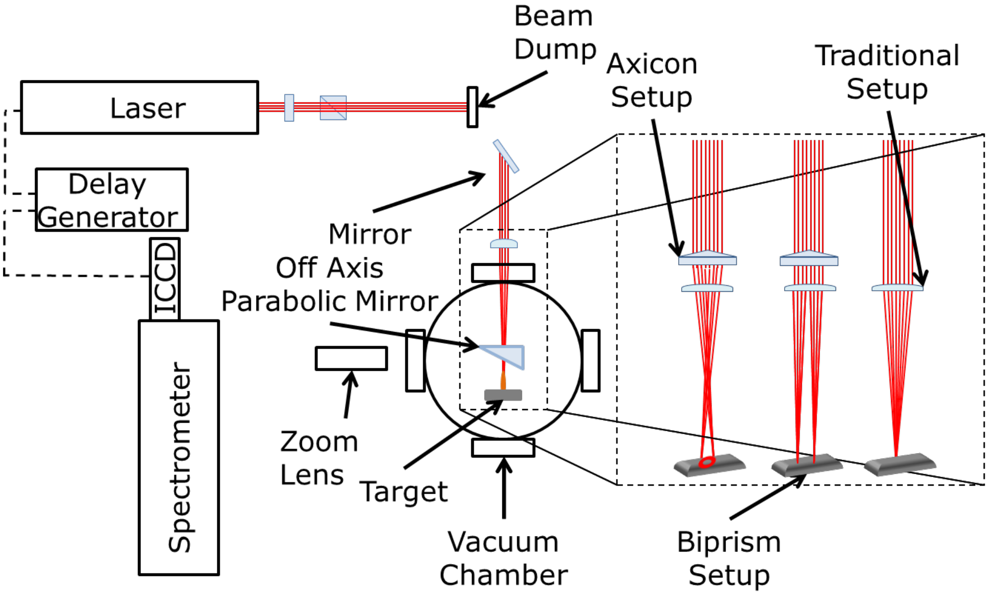

Figure 3.20: Head on time resolved spectroscopy experimental set up, with exploded view of the three focusing geometries.

3.4. Plasma Diagnostic Techniques

The plasma diagnostic techniques carried out in this work are all based on spectroscopy. While other diagnostic techniques revolve around ion measurements they will not be covered here. The primary plasma parameters for laser plasmas are spatio temporal evolution of the plasma plume, electron density and electron temperature. The processes undertaken to extract these parameters are outlined below.

3.4.1 Spatio Temporal Plasma Expansion Dynamics

The study of broadband emission imaging is widely applied to laser produced plasmas. Fast electronic control of ICCD cameras allows for detailed mapping of the evolution of laser plasmas in both time and space. Typical gate widths for the imaging diagnostics contained within this thesis are on the order of tens of nanoseconds which allows for a good balance of temporal resolution and signal level captured on the ICCD. Various gain settings were used throughout the experiments which were corrected for using the data in Figure 3.7. Neutral density filters were also employed to avoid saturation of the camera; these were also taken into account during data analysis and accounted for.

3.4.2 Pressure (Stark Broadening): Density Calculations

The broadening phenomena discussed in section 2.6 are all present within the spectroscopic measurements presented; this convolution of Gaussian and Lorentzian line shapes leads to the measured lines having Voigt profiles. In order to measure the Stark broadening of a particular line the spectral images were partially binned in Matlab. These partially binned spectra were then transferred to Origin, background subtracted and normalised to their respective maxima. Voigt profiles, with a Gaussian component fixed to the HWHM of the instrumental broadening of the Chromex spectrometer, were then fitted to the 466.3 nm Al II line of each spectrum. The Lorentzian components of these fitted Voigt profiles were then extracted and used with Equation 53 [5] to calculate the electron density at the respective time delay of each spectrum. The HWHM of the 466.3 nm line used for these calculations was 0.45 Å at a density of 10^{17} cm^{-3} [6]. This provides the Stark parameter 'ω' in equation 52 below.

$$\Delta\lambda_{width} = 2\omega\left(\frac{n_e}{10^{16}}\right) \qquad \text{Equation 53}$$

3.4.3 Boltzmann Plot Method: Temperature Calculation

Under LTE conditions, the electrons and ions (in this case we focus only on electron temperature) obey a Maxwell-Boltzmann distribution and the distribution of two atomic states can be related by means of the Boltzmann factor by:

$$\frac{N_a}{N_b} = \frac{g_a}{g_b}\exp\left(-\frac{E_a - E_b}{k_b T}\right) \qquad \text{Equation 54}$$

where N_a is the number of atoms (or ions) in the upper energy state, N_b is the number of atoms (or ions) in the lower energy state, g_a and g_b are the degeneracies of the upper and lower levels respectively, $E_a - E_b$ is the difference in energy between the upper and lower energy states [7], T is the electron temperature and k_b is Boltzmann's constant. Providing the plasma is optically thin the integrated intensity of a line (I_{ab}) can be related to the excited state population N_a and the length of the line of sight, l_{sight} by:

$$I_{ab} \approx \frac{h\omega_{ba}}{8\pi^2} A_{ab} N_a l_{sight} \qquad \text{Equation 55}$$

where A_{ab} is the transition probability for spontaneous emission for the transition, ω_{ba} is the frequency of the emitted radiation and h is Planck's constant [7]. Combining Equation 55 with Equation 54 we obtain that:

$$\frac{I_1}{I_2} = \frac{\omega_1 A_1\, g_1}{\omega_2 A_2\, g_2}\exp\left(-\frac{E_1 - E_2}{k_b T}\right) \qquad \text{Equation 56}$$

where 1 and 2 refer to two different spectral lines. Thus by rearranging Equation 56 we are left with an expression for the temperature of the plasma:

$$k_b T = \frac{E_2 - E_1}{\ln\left(\frac{\omega_1 A_1\, g_1 I_1}{\omega_2 A_2\, g_2 I_2}\right)} \qquad \text{Equation 57}$$

This method rarely permits temperature calculations with errors of less than 10% [7]. It can be improved upon by measuring the intensity of a number of lines and plotting the logarithm of this intensity versus the upper energy level of the transition, with the appropriate constants:

$$\ln\left(\frac{I\lambda}{gA}\right) = -\frac{1}{k_bT}E$$

Equation 58

The value of the slope from this so-called Boltzmann plot can be used to calculate the electron temperature [8], [9].

3.4.4 Successive Charge State Ratio Method: Temperature Calculation

Given the relatively small differences between excited energy levels within an ion their ratios do not lend themselves to very precise temperature measurements [7]. The precision of temperature measurements can be improved by measuring the ratio of two line intensities from successive charge states. This increases the energy separation by the ionisation energy of the atom of interest which usually leads to the energy difference being greater than k_BT.

$$\frac{I_1}{I_2} = \left(\frac{\omega_1 g_1 A_1}{\sqrt{\pi}\,\omega_2 g_2 A_2}\right)\left(4\pi {a_0}^3 N_e\right)^{-1}\left(\frac{kT_e}{E_H}\right)^{\frac{3}{2}}\exp\left(-\frac{E_1 + E_\infty - E_2 - \Delta E_\infty}{kT_e}\right)$$

Equation 59

where the higher charge state is denoted by the subscript 1 and the constants have the same meaning as above. E_H is represents the ionisation energy of the hydrogen atom and a_o is the Bohr radius. E_∞ and ΔE_0 are the ionisation energy of the lower ion stage and the high density correction factor which accounts for the difference in ionisation energy due to a strong electric field, and is given by Equation 60.

$$\Delta E_{\infty} = 3z\frac{e^2}{4\pi\varepsilon_0}\left(\frac{4\pi N_e}{3}\right)^{\frac{1}{3}} \qquad \text{Equation 60}$$

The error in the slope of a Boltzmann plot is usually greater than the error present in the line ratio, therefore the use of the successive charge state method will provide better precision than the Boltzmann plot method.

In order to extract electron temperature values from spectroscopic measurements a combination of the density, extracted using Equation 53 and Equation 59 is required. The ratio of the measured line intensities is compared to the right hand side of Equation 59, into which the electron density for the same experimental conditions is inserted, while the temperature is varied. The electron temperature is the value, which when inserted allows the right hand side of the equation to equal the left hand side. This process is illustrated graphically in Figure 3.21 for ease of understanding.

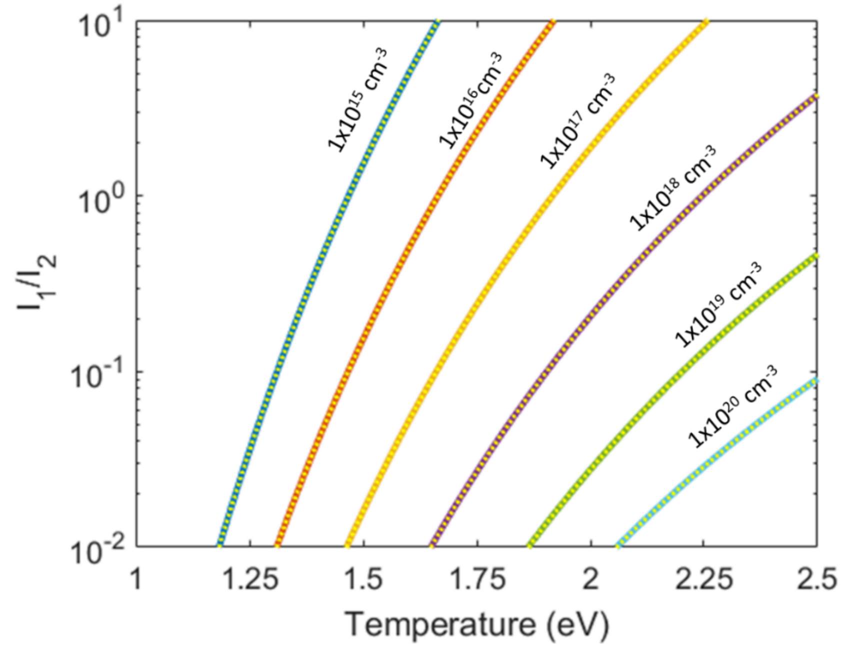

Figure 3.21: Theoretical intensity ratio for the Al^{2+} 451.3nm and Al^{+} 466.6nm transitions, calculated using Equation 59 for a number of electron densities across the range of 1 eV to 2.5 eV. The inset refers to electron density (cm^{-3}).

Figure 3.21 contains calculated, using Equation 59 and the relevant constants [10], values for the intensity ratio of the 451.38 nm and the 466.3 nm aluminium lines, the former being doubly ionised and the latter being singly ionised.

Two final points on the above are worth noting. Firstly it is assumed that the plasma exists in a state of local thermodynamic equilibrium (LTE) or at least that part of the plasma (plume or stagnation layer) that is imaged onto the spectrometer exists in LTE. To check for LTE the well-known McWhirter criterion (Equation 29 on page 26) is employed $n_{e\,(cm^{-3})} > 1.6\,x\,10^{12}(T_e)^{\frac{1}{2}}\,(\Delta E)^3$ [11] with temperature T_e in Kelvin and transition energy ΔE in eV. The condition is relaxed for optical and IR transition (small ΔE) and hence these are often preferred in plasma diagnostics. For example, for the 466.3 nm line of Al^+ ($\Delta E = 2.66\,eV$), for $T_e = 1eV\,(11{,}600\,K)$ $n_e > 3.2\,x\,10^{15}$ cm^{-3} while for $T_e = 2\,eV\,n_e > 3.8\,x\,10^{15}$ cm^{-3}. As the electron density varies in the 10^{16} – 10^{17} cm^{-3} range in our studies we can state that the criterion is satisfied here.

Secondly, plasma opacity can alter the shape and/or intensity of emission lines to determine electron densities and/or temperatures. It can be quite prevalent in laser plasma plumes which have a hot core surrounded by material which rapidly cools due to radiation emission For this reason checks on plasma opacity should be carried out to determine at a minimum its presence or absence, and ideally to quantify it. It is particularly a problem for transitions ending on the ground, or a low lying state of the atom or ion under consideration. One way to check for opacity is to measure the line intensity ratio for a doublet, e.g., the 3p ($^2P_{1/2,3/2}$) to 4s ($^2S_{1/2}$) transitions in atomic Al at 394.40 nm and 396.15 nm. In the absence of opacity the line ratio should equal the statistical value of 2:1. Any deviation from this value indicates the presence of opacity and the degree of deviation, points to the severity of the effect.

The effect can be estimated by simple application of the Beer-Lambert law, $I(\lambda) = I_0 e^{-\sigma NL}$ where σ is the photoabsorption cross section (units of cm^2) and *NL* is the column density (units of cm^{-2}). For the Al doublet the statistically weighted cross sections are 2×10^{-13} cm^2 for the 394 nm line and 4 x 10^{-13} cm^2 for the 396 nm line. The effect of increasing NL (opacity) on the line ratio is shown in Table 3.4 below.

Table 3.4. Effect of opacity on Al doublet ($^2P_{3/2,1/2}$ – $^2S_{1/2}$) line ratio.

NL (cm^{-2})	I/I_0 (394 nm)	I/I_0 (396 nm)	396 nm/394nm
10^{10}	0.998	0.996	1.996
10^{11}	0.980	0.960	1.959
10^{12}	0.819	0.670	1.638
2 x 10^{12}	0.670	0.449	1.340
5 x 10^{12}	0.368	0.135	0.734
10^{13}	0.135	0.018	0.267

It is clear that this doublet is highly sensitive to opacity and is hence a good indicator of a plume potentially having a temperature and density profile likely to exhibit opacity. Of course, it depends on the actual transition and it can be avoided in many cases by choosing emission lines connected by high lying states which will not be absorbed by plasma species in ground or low lying states. This the reason for selecting lines of Al^+ and Al^{2+} for measuring temperature using the line ratio method. Also, line profiles can be distorted by opacity and so we also use ion lines for the Stark broadening measurements.

3.5. Laser Induced Breakdown Spectroscopy

As outlined in section 2.7 the primary metric of figure-of-merit for LIBS is the LOD, which can be found for a system through the generation of calibration curves. These calibration curves are created for specific elements (or analytes) in specific host materials or matrices. In this work calibration curves for manganese and copper in aluminium have been constructed.

3.5.1 Calibration Curves

Calibration curves are constructed by measuring the line intensity from a sample with a known concentration of an analyte (element), repeating this measurement for a number of samples of varying analyte concentration and plotting this line intensity versus the concentration of the analyte [12], [13]. This plot will yield a straight line, the slope of which, combined with the standard deviation of the signal from a blank sample, can then be combined as in Section 2.7 to extract the limit of detection of the system, for the specific analyte.

3.5.2 Certified Reference Materials

The certified reference materials used for these experiments were supplied by MBH Analytical [14]. Four samples were purchased, each of which had aluminium as the bulk material and varying amounts of trace elements, which are listed in table 3.5.

Table 3.5: Elemental concentrations of interest contained within the certified reference materials.

Reference Material	Sample Number	Percentage Copper	Percentage Aluminium
511XG6082 (B)	1	0.014	97.64
511XG6082 (A)	2	0.018	97.71
511XG3000B4	3	0.086	96.87
511XG6061	4	0.26	97.5

3.6. Summary

An overview of the experimental systems used to make the measurements in this work has been presented. The purpose of this chapter was to describe the apparatus and experimental systems used for all the work contained within this thesis. For the presented work all laser plasmas were created in vacuo and the simple vacuum system used has been described. Detailed schematics of experimental setups have been provided. The theory and methods for extracting electron temperature and density from spectroscopic data is described. The practicalities of laser induced breakdown spectroscopy have been put presented. A brief description of the actual experimental setup used for a particular set of results will be given at the start of the respective results chapter.

Bibliography

[1] Continuum, “Continuum Surelight Specifications,” *http://www.continuumlasers.com/images/stories/products/specifications/High_Energy/Surelite_Series_Spec.pdf*, 2018.

[2] Andor, “Andor iStar Specifications,” *https://andor.oxinst.com/assets/uploads/products/andor/documents/andor-istar-ccd-spectroscopy-specifications.pdf*, 2018.

[3] R. K. Singh and J. Narayan, “Pulsed-laser evaporation technique for deposition of thin films: Physics and theoretical model,” *Phys.Rev.B*, vol. 41, no. 13, pp. 8843–8859, May 1990.

[4] H. Luna, K. D. Kavanagh, and J. T. Costello, “Study of a colliding laser-produced plasma by analysis of time- and space-resolved image spectra,” *J. Appl. Phys.*, Vol. 101, no. 3, Art. No. 033302, 2007.

[5] H. R. Griem, *Spectral line broadening by plasmas*. New York and London: Academic Press, 1974.

[6] A. W. Allen, M. Blaha, W. W. Jones, A. Sanchez, and H. R. Griem, “Stark-broadening measurement and calculations for a singly ionized aluminum line,” *Phys. Rev. A*, Vol. 11, no. 2, pp. 477–479, 1975.

[7] H. R. Griem, *Princples of Plasma Spectroscopy*. Cambridge University Press, 2005.

[8] R. S. Adrian, J. Watson, P. H. Richards, and A. Maitland, “Laser microspectral analysis of steels,” *Opt. Laser Technol.*, Vol. 12, no. 3, pp. 137–143, 1980.

[9] C. Fallon, P. Hayden, N. Walsh, E. T. Kennedy, and J. T. Costello, “Target geometrical effects on the stagnation layer formed by colliding a pair of laser produced copper plasmas,” *Phys. Plasmas*, Vol. 22, no. 9, Art. No. 093506, 2015.

[10] D. E. Kelleher and L. I. Podobedova, “Atomic Transition

Probabilities of Aluminum. A Critical Compilation," *J. Phys. Chem. Ref. Data*, Vol. 37, no. 2, pp. 709–911, 2008.

[11] R. W. P. McWhirter, *Plasma Diagnostic Techniques*. Acedemic Press, 1965.

[12] P. Devangad *et al.*, "Performance evaluation of Laser Induced Breakdown Spectroscopy (LIBS) for quantitative analysis of rare earth elements in phosphate glasses," *Opt. Mater. (Amst).*, Vol. 52, pp. 32–37, 2016.

[13] G. S. Senesi and N. Senesi, "Laser-induced breakdown spectroscopy (LIBS) to measure quantitatively soil carbon with emphasis on soil organic carbon. A review," *Anal. Chim. Acta*, Vol. 938, pp. 7–17, 2016.

[14] MBH Analytical, "Reference Materials Catalogue," *http://mbh.co.uk/_downloads/catalogues/MBH-Metals_Catalogue-2018.pdf*, 2018.

4. Stagnation Layer Formation in Dual and Annular Colliding Plasmas

The expansion of an aluminium plasma, formed with 1064 nm pulses, into ambient air pressures of both 1x10^{-2} mbar and 1x10^{-5} mbar was studied using a gated ICCD for both imaging and spectroscopy. Aluminium was chosen as it exhibits strong emission in the visible spectral range and due to a body of prior work [1–4] by previous group members that was available and which could be built upon. Although there is a substantial body of work in the literature on tracking plasma plume expansion dynamics using time gated CCD cameras e.g., [5 – 8], few view the plasma along the expansion axis [9, 10]. In this chapter imaging was carried out at both viewing angles; *'side on'*, where the target normal is parallel to the CCD sensor surface, and *'head on'*, where the target normal is orthogonal to the CCD sensor plane.

Although annular plasmas formed in air have been imaged using ICCD cameras in the past [11], to the best of my knowledge, the generation of a stagnation layer at the axis of symmetry of an annular plasma is shown here for the first time. The dynamics of this annular plasma, especially the formation of a stagnation layer along its axis of symmetry, are compared to those of a single point plasma and a pair of colliding point (seed) plasmas. The latter results in the formation of a stagnation layer as observed by many authors previously [12 – 16].

4.1 Time Integrated Broadband Imaging

Each image presented in this section has been normalised to its own maximum while the contrast for each image has also been kept fixed. These steps were taken to allow for comparisons between the various experimental parameters, as well as to ensure the visibility of the stagnation layer in the integrated images, where the intensity of the seed and annular plasmas can dominate.

4.1.1 Time Integrated, Broadband Imaging of a Single Plasma

Figure 4.1 and Figure 4.2 show time integrated, broadband images of a single plasma formed at the focus of a Nd:YAG laser on the surface of a flat Al target at three different laser pulse energies (28 mJ, 38mJ and 52mJ) and two different ambient air pressures (1x10-2 mbar and 1x10-5 mbar).

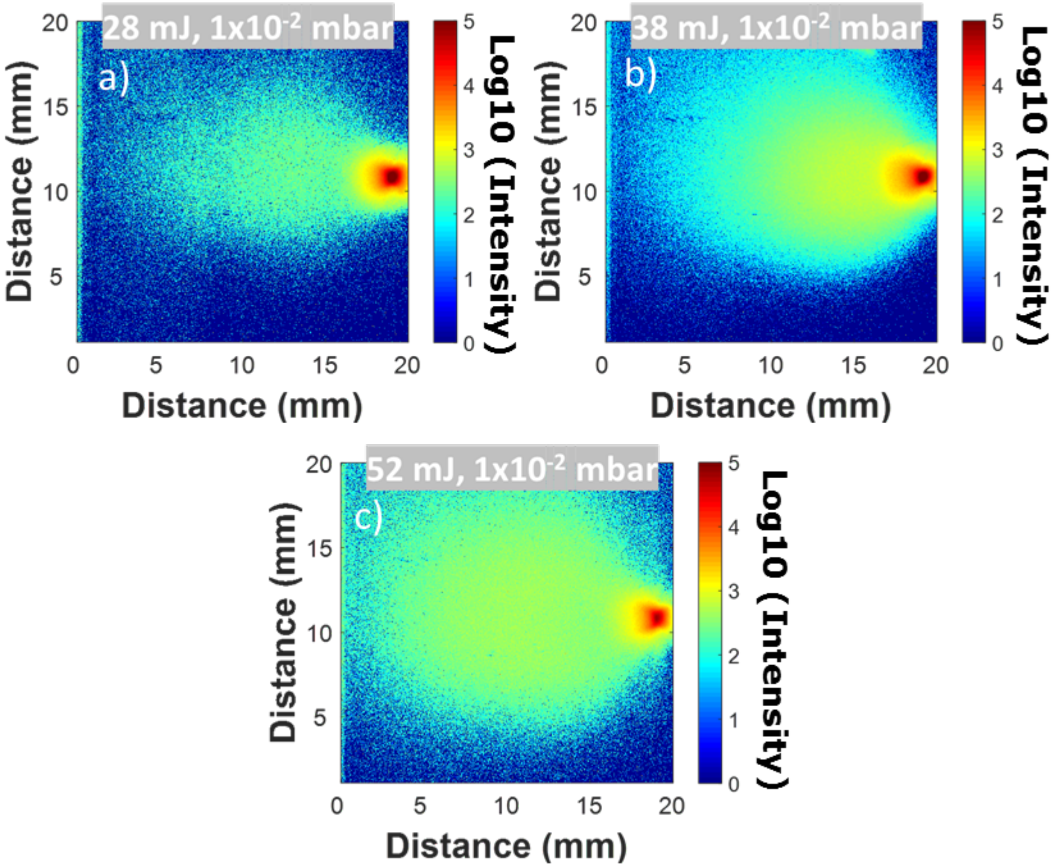

Figure 4.1 Side on time integrated broadband images of a single aluminium plasma plume at an ambient pressure of $1x10^{-2}$ mbar, with laser pulse energies of a) 28 mJ, b) 38 mJ and c) 52 mJ. The intensity scale corresponds to the Log_{10} of the raw ICCD counts.

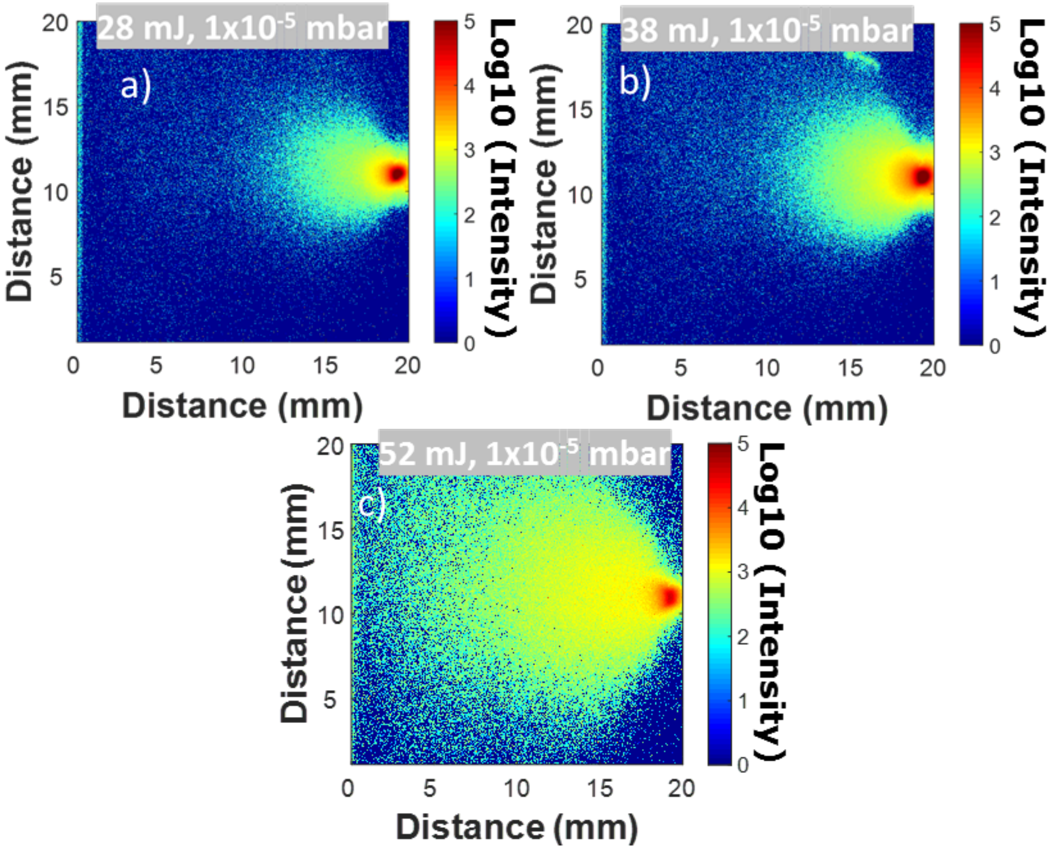

Figure 4.2: Side on time integrated broadband images of a single aluminium plasma plume at an ambient pressure of $1x10^{-5}$ mbar, with laser pulse energies of a) 28 mJ, b) 38 mJ and c) 52 mJ. The intensity scale corresponds to the Log_{10} of the raw ICCD counts.

In the higher pressure cases (Figure 4.1, 1×10^{-2} mbar) the emitting plasma size appears to be larger than in the low pressure (Figure 4.2, 1×10^{-5} mbar) cases. This is likely due to the plasma plume exciting the gas around it in the former case. It is also clear from the intensity scales on the unnormalized images (left hand side of each figure) that the peak counts do not vary much with laser pulse energy for the higher pressure case, from 2×10^5 to 3×10^5 for plasmas formed in air at 1×10^{-2} mbar. For the lower pressure (in vacuo) case the counts vary from 3×10^5 to 8×10^5 , i.e., for plasmas formed in air at 1×10^{-5} mbar. In relation to the dependence of physical extent of each plume on laser pulse energy, there appears to be little difference in the *relative* increase in size with laser pulse energy.

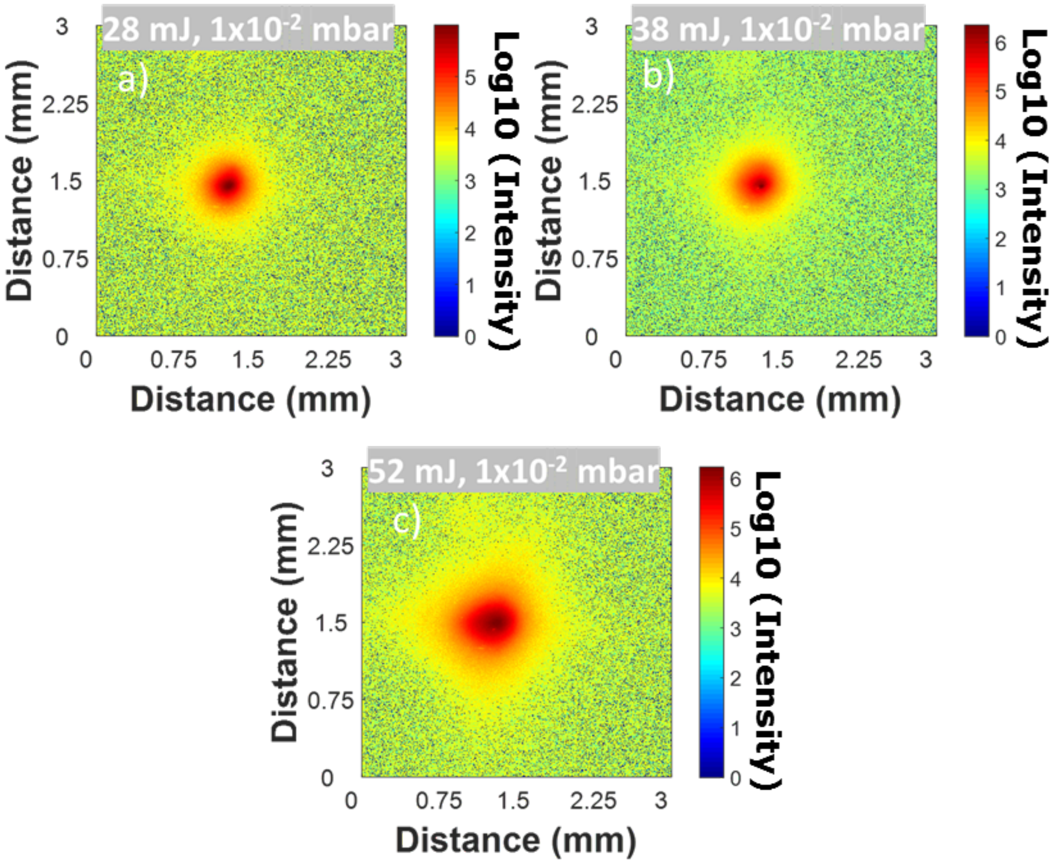

Figure 4.3: Head on time integrated broadband images of a single aluminium plasma plume at an ambient pressure of 1x10^{-2} mbar, with laser pulse energies of a) 28 mJ, b) 38 mJ and c) 52 mJ. The intensity scale corresponds to the Log$_{10}$ of the raw ICCD counts.

Time integrated images of single laser plasma plumes recorded head-on are shown in Figure 4.3 (1x10^{-2} mbar) and Figure 4.4 (1x10^{-5} mbar). The plasmas display a high degree of circular symmetry. It is also clear that the lateral extent of the cylindrically symmetric plumes do not change significantly with laser pulse energy in the 28 – 52 mJ range, albeit it can be seen that they do expand slightly in the saturated images to the right hand side of each of the figures for both the low and high air pressures.

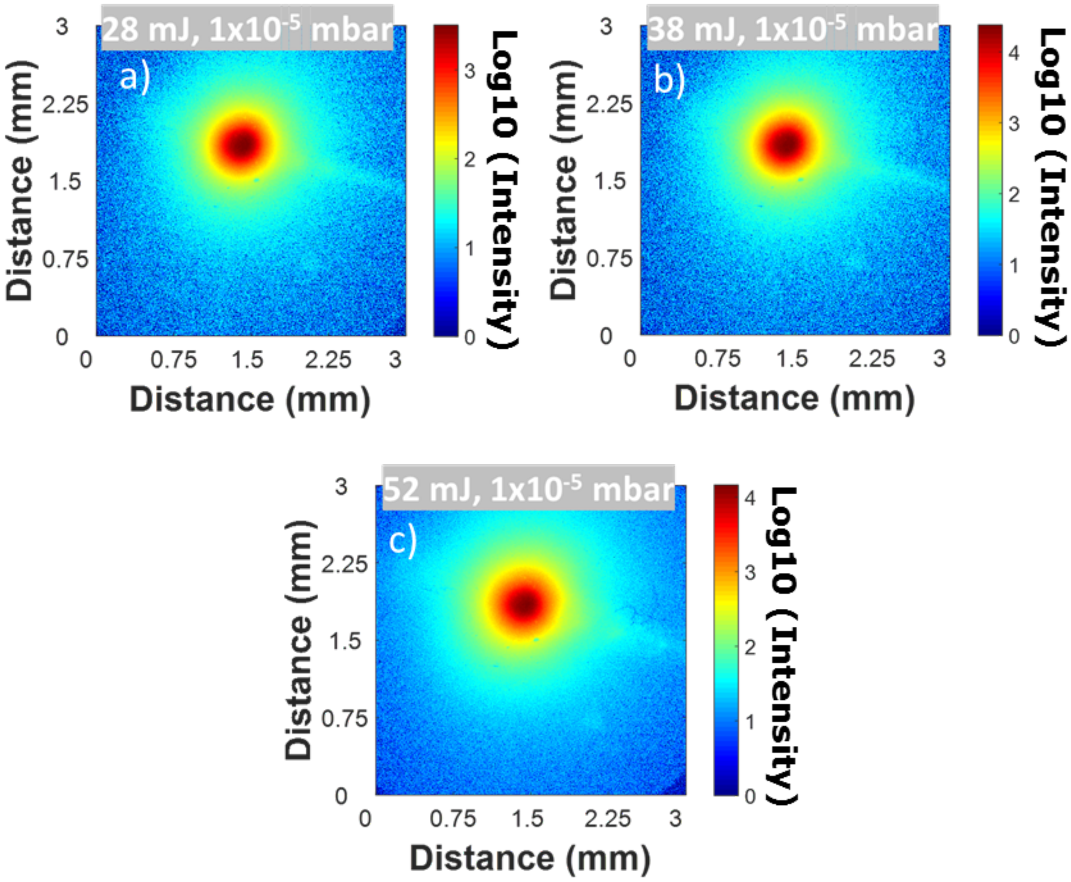

Figure 4.4: Head on time integrated broadband images of a single aluminium plasma plume at an ambient pressure of 1x10^{-5} mbar, with laser pulse energies of a) 28 mJ, b) 38 mJ and c) 52 mJ. The intensity scale corresponds to the Log$_{10}$ of the raw ICCD counts.

4.1.2 Time Integrated, Broadband Imaging of Two Seed Plasmas

Figures 4.5 and 4.6 show side-on, time integrated images of a pair of colliding plasma plumes at a chamber pressures of 1 x 10^{-2} mbar and 1 x 10^{-5} mbar) respectively. Figure 4.6 (1 x 10^{-5} mbar) clearly shows the difference between hard and soft stagnation, as defined in chapter 3.

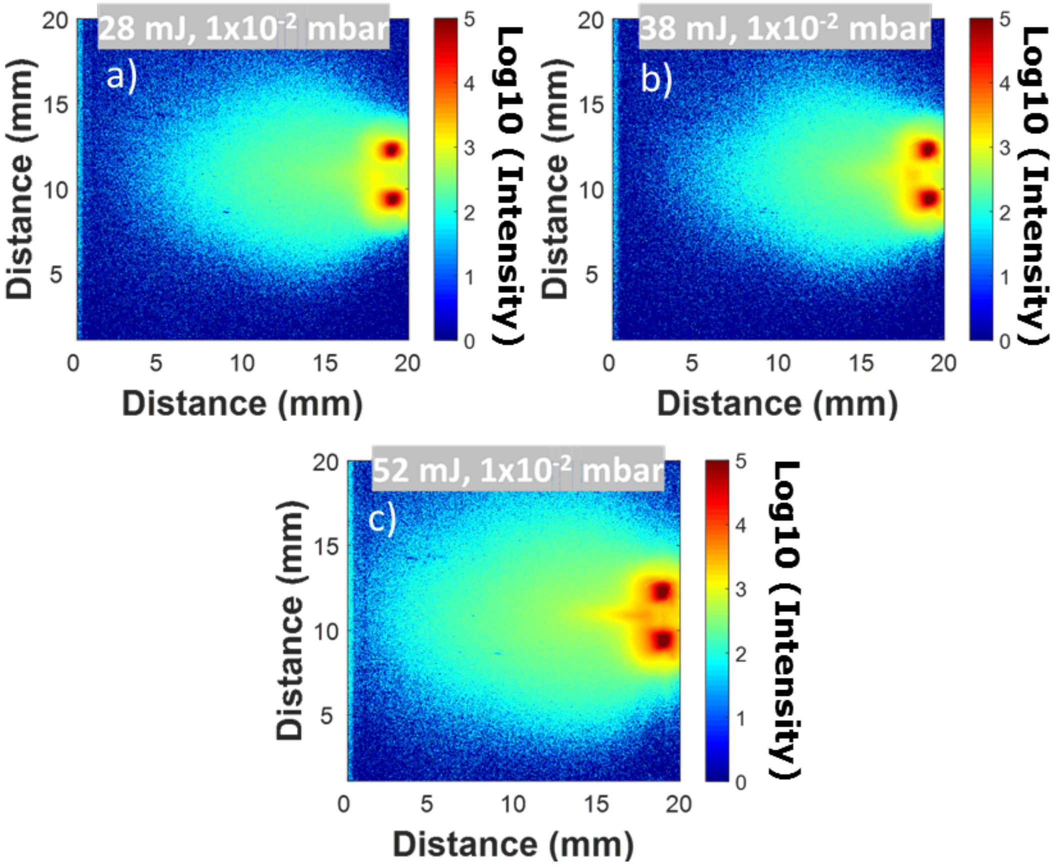

Figure 4.5: Side on time integrated broadband images of two aluminium seed plasmas, and resulting stagnation layer, at an ambient pressure of 1x10^{-2} mbar, with laser pulse energies of a) 28 mJ, b) 38 mJ and c) 52 mJ. The intensity scale corresponds to the Log$_{10}$ of the raw ICCD counts.

At higher energy and lower pressure the stagnation layer clearly forms and extends up to 15 mm from the target. On the other hand, at this distance, and at the higher ambient air pressure, quite diffuse and weak emission is observed. Also the stagnation layer is seen to be more confined in the direction normal to the target surface, extending only to a distance of 5 mm or so in Figure 4.5.

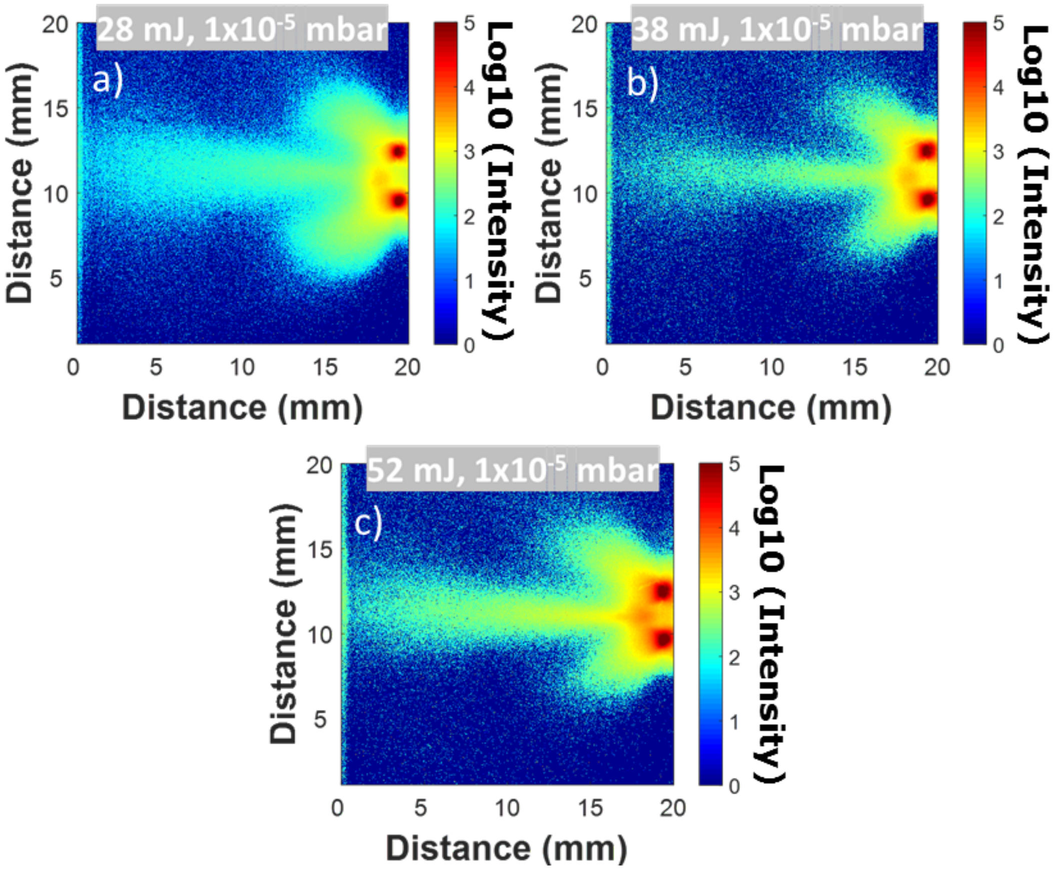

Figure 4.6: Side on time integrated broadband images of two aluminium seed plasmas, and resulting stagnation layer, at an ambient pressure of $1\text{x}10^{-5}$ mbar, with laser pulse energies of a) 28 mJ, b) 38 mJ and c) 52 mJ. The intensity scale corresponds to the Log_{10} of the raw ICCD counts.

The images also show clearly that the stagnation layer brightness does increase with increasing laser pulse energy at both pressures of 1×10^{-2} mbar and 1×10^{-5} mbar of air. What is also clear from the images in each figure is that most of the radiation emitted from this colliding plasma system comes from the seed plasmas and not the stagnation layer (which is not visible when the full dynamic range is displayed).

Figure 4.7 and Figure 4.8 show head-on, time integrated images of a pair of colliding plasma plumes at a chamber pressures of 1 x 10^{-2} mbar and 1 x 10^{-5} mbar) respectively. As the seed plasmas are so bright it is not possible to see the stagnation layers in the head on images shown in Figure 4.7.

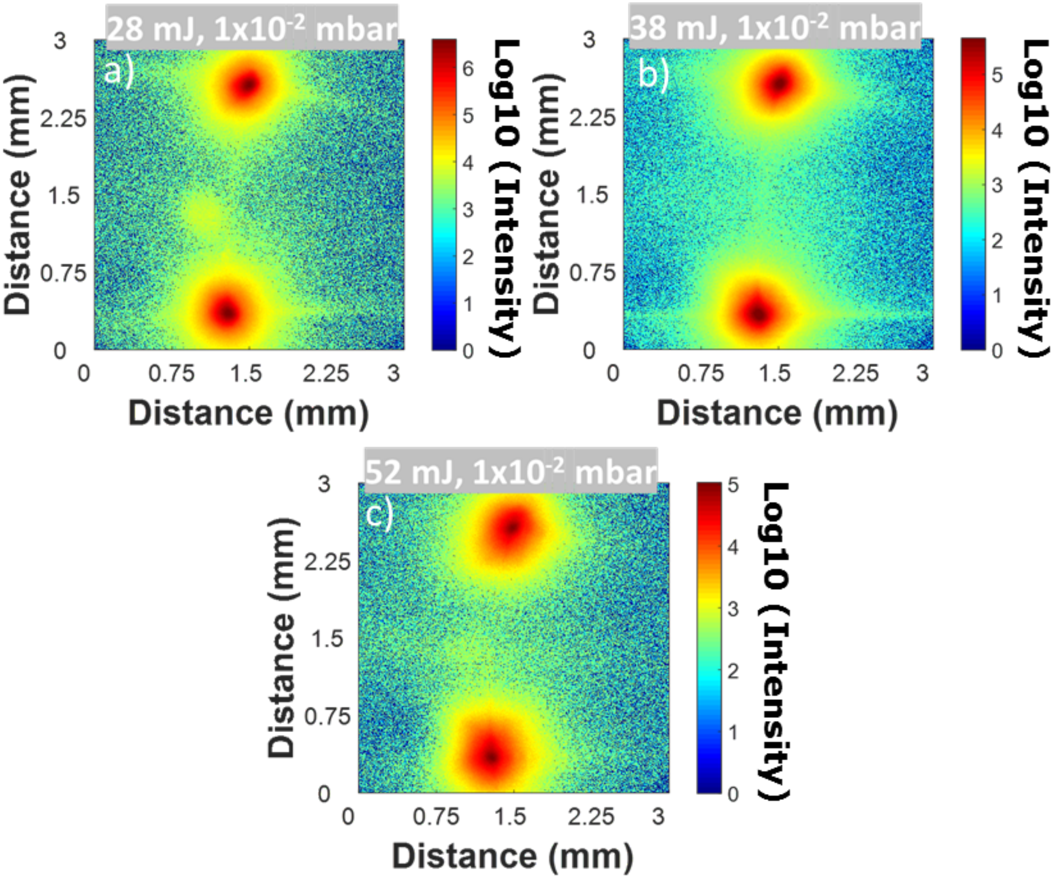

Figure 4.7: Head on time integrated broadband images of two aluminium seed plasmas, and resulting stagnation layer, at an ambient pressure of 1x10^{-5} mbar, with laser pulse energies of a) 28 mJ, b) 38 mJ and c) 52 mJ. The intensity scale corresponds to the Log_{10} of the raw ICCD counts.

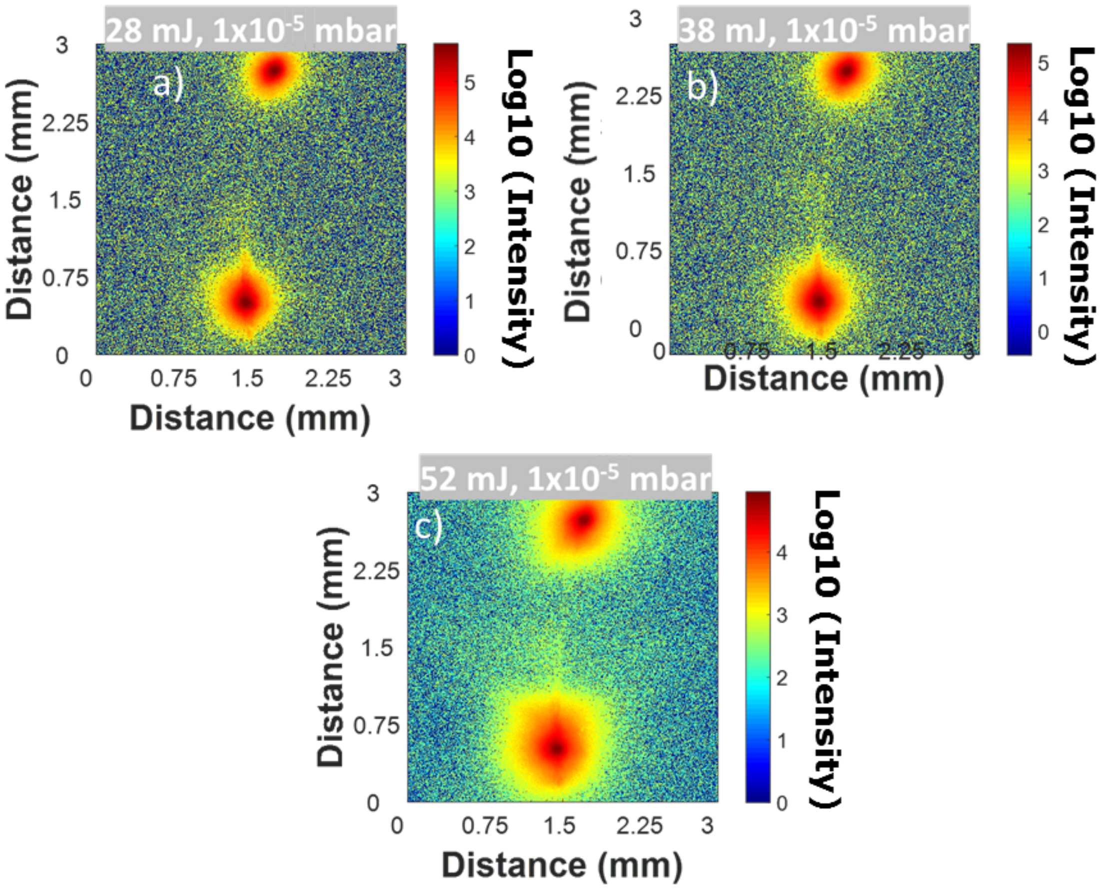
28 mJ, 1x10^{-5} mbar

38 mJ, 1x10^{-5} mbar

52 mJ, 1x10^{-5} mbar

Figure 4.8: Head on time integrated broadband images of two aluminium seed plasmas, and resulting stagnation layer, at an ambient pressure of 1x10^{-5} mbar, with laser pulse energies of a) 28 mJ, b) 38 mJ and c) 52 mJ. The intensity scale corresponds to the Log$_{10}$ of the raw ICCD counts.

4.1.3 Time Integrated, Broadband Imaging of an Annular Plasma.

The side on imaging in Figure 4.9 and Figure 4.10 shows the formation of a stagnation layer at the centre of an annular plasma for all energies at both high (1x10^{-2} mbar) and low (1x10^{-5} mbar) pressures.

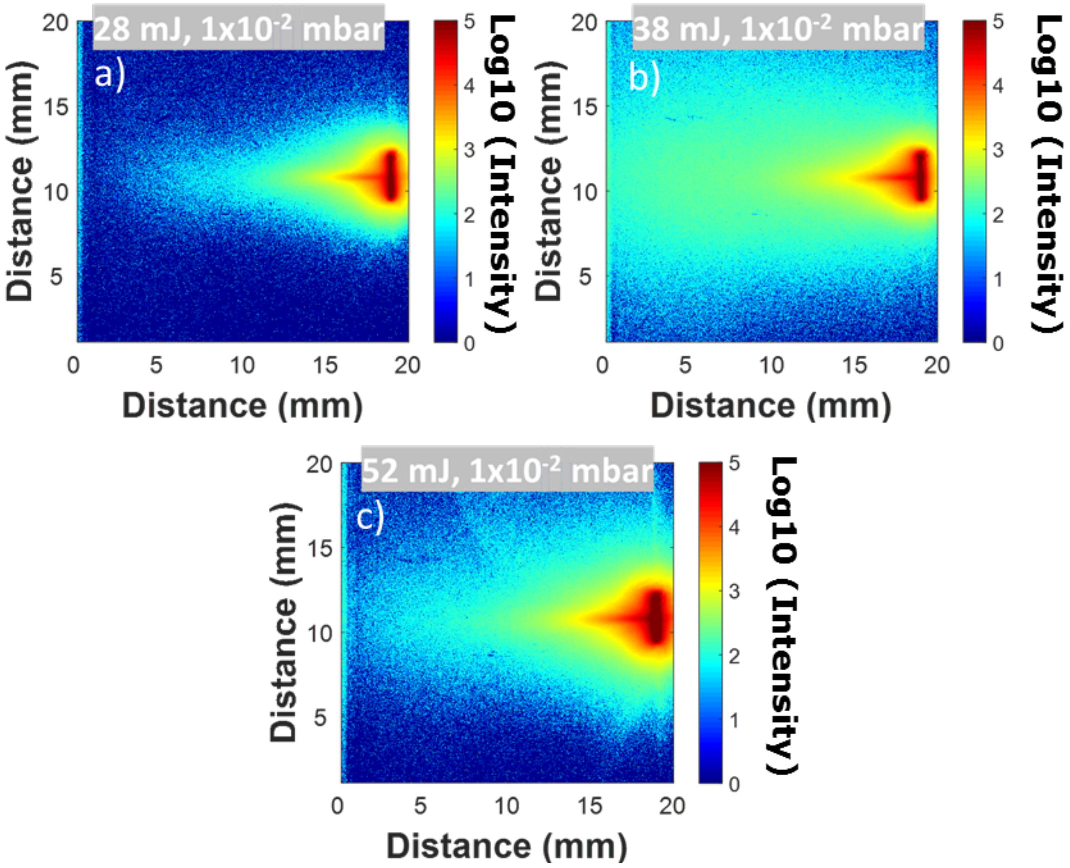

Figure 4.9: Side on time integrated broadband images of an annular aluminium plasma, and resulting stagnation layer, at an ambient pressure of 1x10^{-2} mbar, with laser pulse energies of a) 28 mJ, b) 38 mJ and c) 52 mJ. The intensity scale corresponds to the Log_{10} of the raw ICCD counts.

In this sense the brightness of the stagnation layer, relative to the seed (i.e., ring) plasma, is closer than in the case of the two point seed plasmas where they dominate the integrated images. This also clear from the images where the stagnation layer brightness and extent scales strongly with laser pulse energy. In relation to differences between the time integrated images with pressure (namely 1 x 10^{-2} mbar vs. 1 x 10^{-5} mbar) there are no very significant differences for the unsaturated images. It is clear, as in the case of two point plasmas, that the extent of the stagnation layer emission is greater at the high pressure (compare panels (c) in both figures) as it was in the case of a pair of colliding plasmas. Once again, interaction with the background air at the higher pressure is likely to be the underlying reason for this observation.

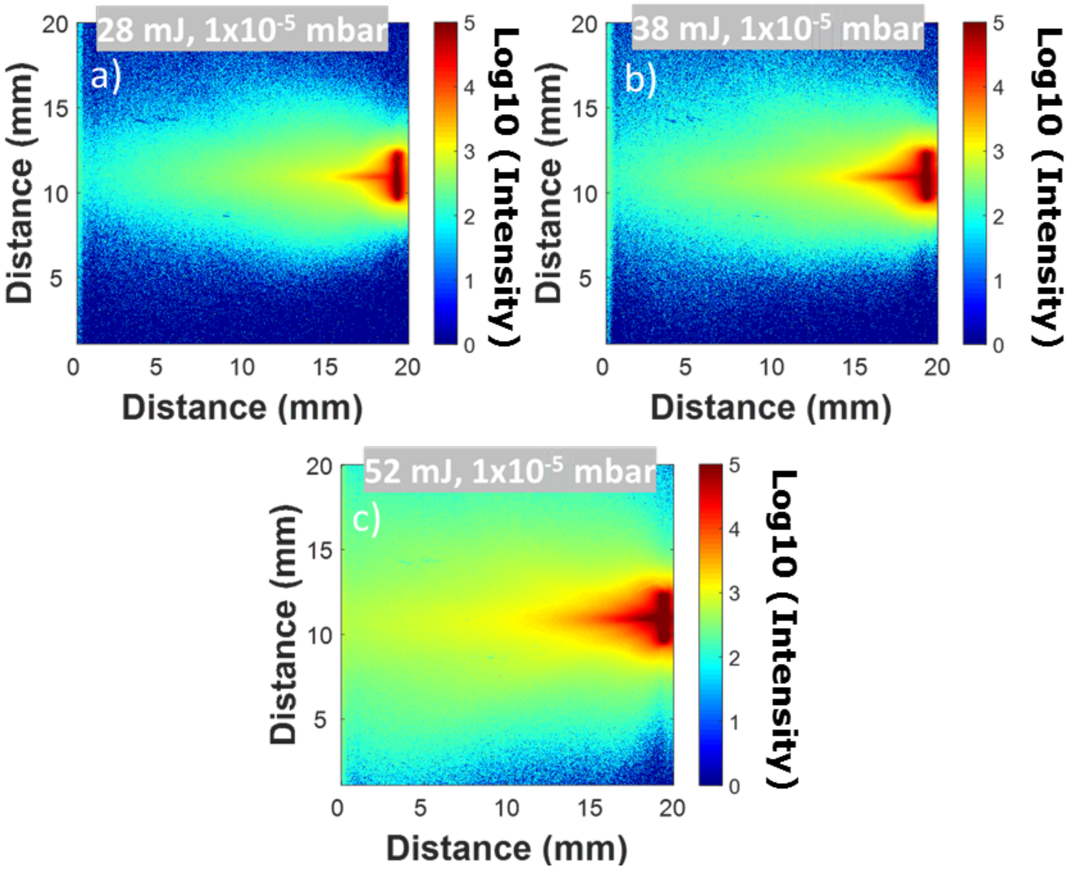

Figure 4.10: Side on time integrated broadband images of an annular aluminium plasma, and resulting stagnation layer, at an ambient pressure of $1x10^{-5}$ mbar, with laser pulse energies of a) 28 mJ, b) 38 mJ and c) 52 mJ. The intensity scale corresponds to the Log_{10} of the raw ICCD counts.

Figure 4.11 and Figure 4.12 show head-on time integrated images of the annular plasma in air pressures of $1x10^{-2}$ mbar and $1x10^{-5}$ mbar. The stagnation layer formed at the centre or axis of each annulus is evident in each case. It is clear from the images that the focused annuli are somewhat elliptical and hence stagnation layers do not possess perfectly circular cross sections.

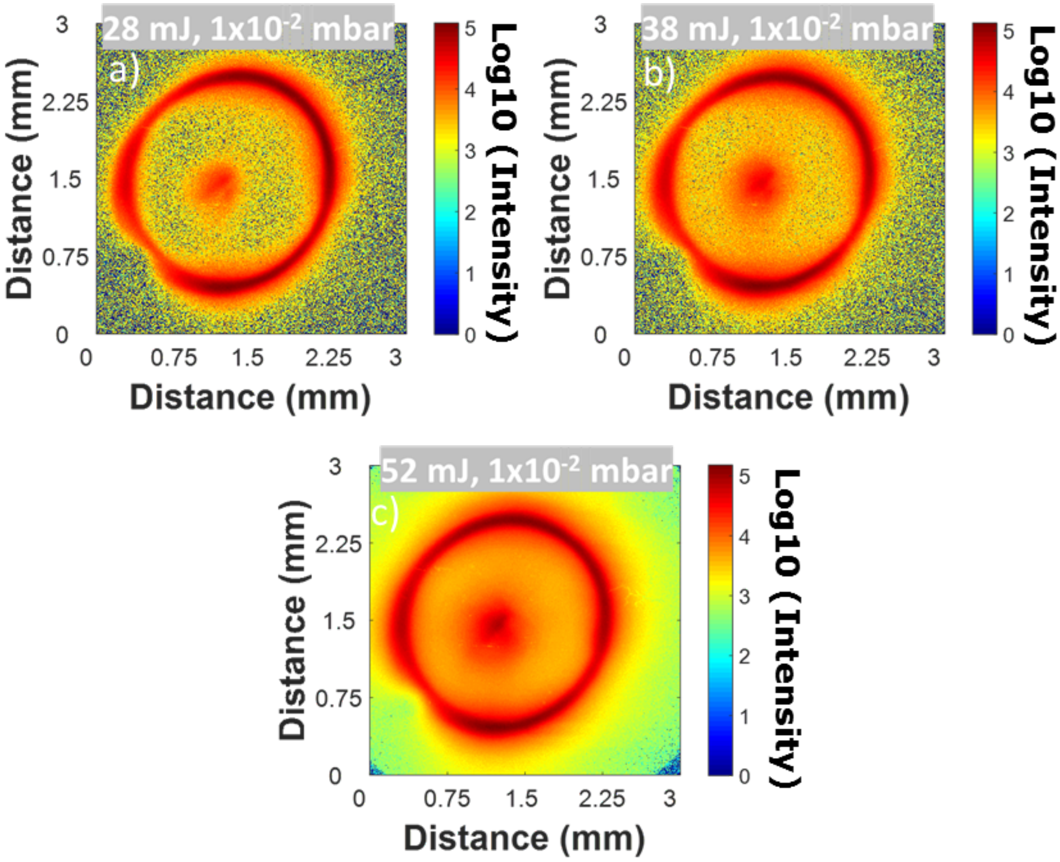

Figure 4.11: Head on time integrated broadband images of an annular aluminium plasma, and resulting stagnation layer, at an ambient pressure of $1x10^{-2}$ mbar, with laser pulse energies of a) 28 mJ, b) 38 mJ and c) 52 mJ. The intensity scale corresponds to the Log_{10} of the raw ICCD counts.

As for the side-on views the stagnation layers are visible in these time integrated images, in quite stark contrast to those formed at the collision plane between two point plasma plumes where the seed plasmas are so bright as to occlude the weaker stagnation layers.

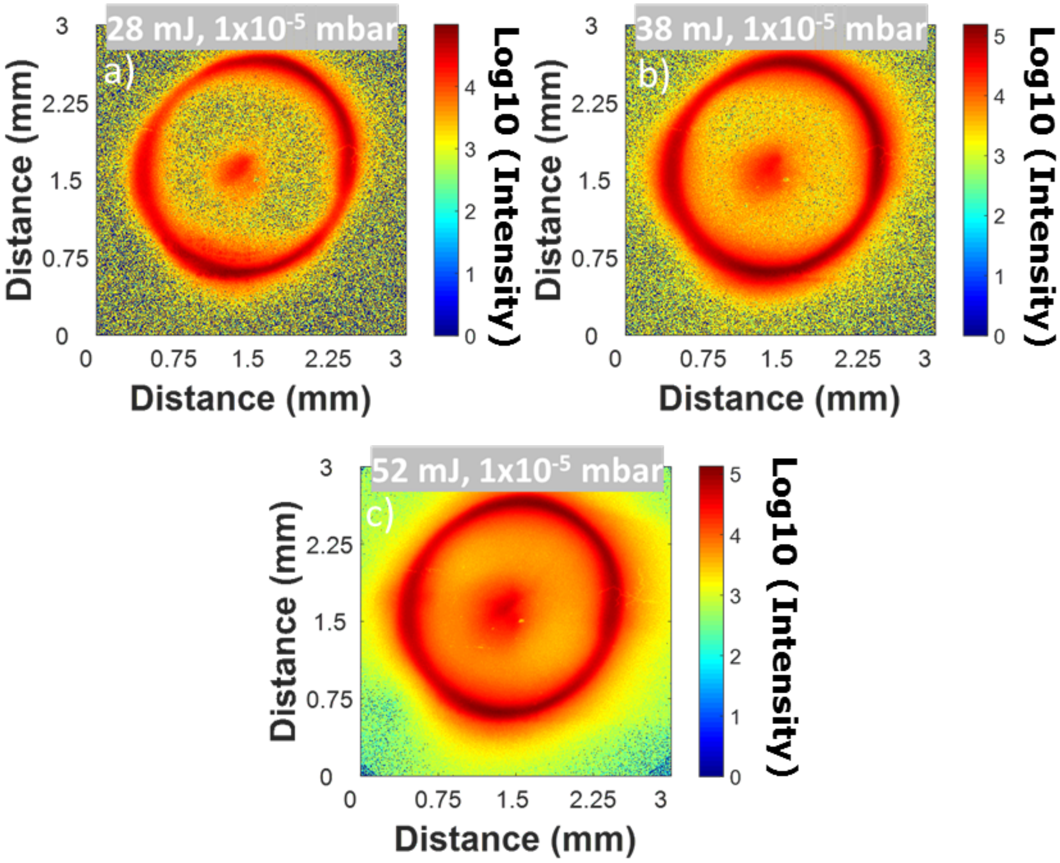

Figure 4.12: Head on time integrated broadband images of an annular aluminium plasma, and resulting stagnation layer, at an ambient pressure of $1x10^{-5}$mbar, with laser pulse energies of a) 28 mJ, b) 38 mJ and c) 52 mJ. The intensity scale corresponds to the Log_{10} of the raw ICCD counts.

4.1.4 Space Resolved, Time Integrated, Broadband Intensity Distributions

The intensity distribution of a time integrated image generated with each focusing geometry (single lens, biprism and axicon) is, from a side on perspective, shown in Figure 4.13. The respective curves were generated by binning the time integrated image for each focusing geometry, over the 2mm x 20mm area which falls between the two seed plasmas in the dual colliding geometry. This area was chosen to exclude the seed plasmas and allow for a comparison between the different expansion shapes of the stagnation layers. While viewing the curves it should be borne in mind that the lower intensity in the biprism case is due to the exclusion of any of the initial plasma, which has not been excluded for the other geometries.

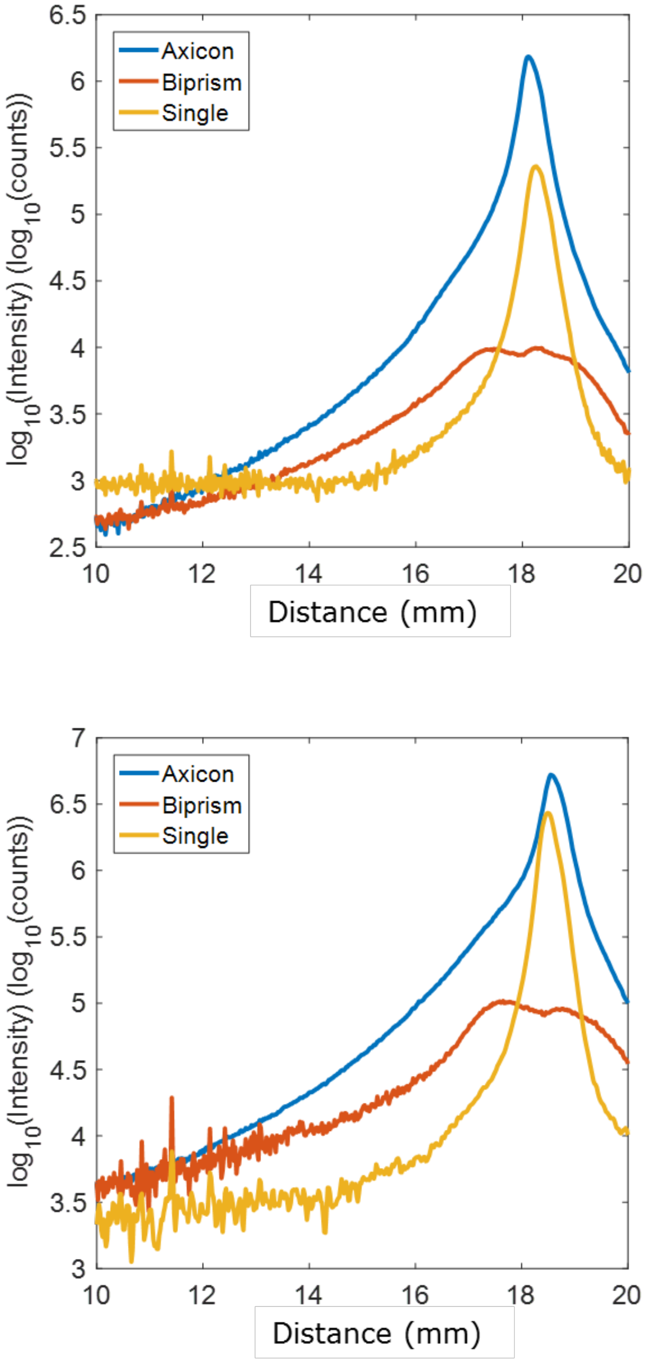

Figure 4.13: Side on, space resolved, time integrated broadband intensity distribution of each focusing geometry at an ambient pressure of 1x10^{-2} mbar (top) and 1x10^{-5} mbar (bottom) for each of the three plasma generation configurations. The laser energy was 52 mJ.

In both the higher (1x10^{-2} mbar) and lower (1x10^{-5} mbar) pressure environments the order of decreasing peak intensity is the annular plasma, single plasma and dual colliding case. However the luminous areas of both the annular and dual colliding case propagate further than the single plasma case, this is due to the emission from stagnation layer formation in the former cases. In the lower pressure environment all three plasma cases propagate further when compared to the same case at a higher pressure.

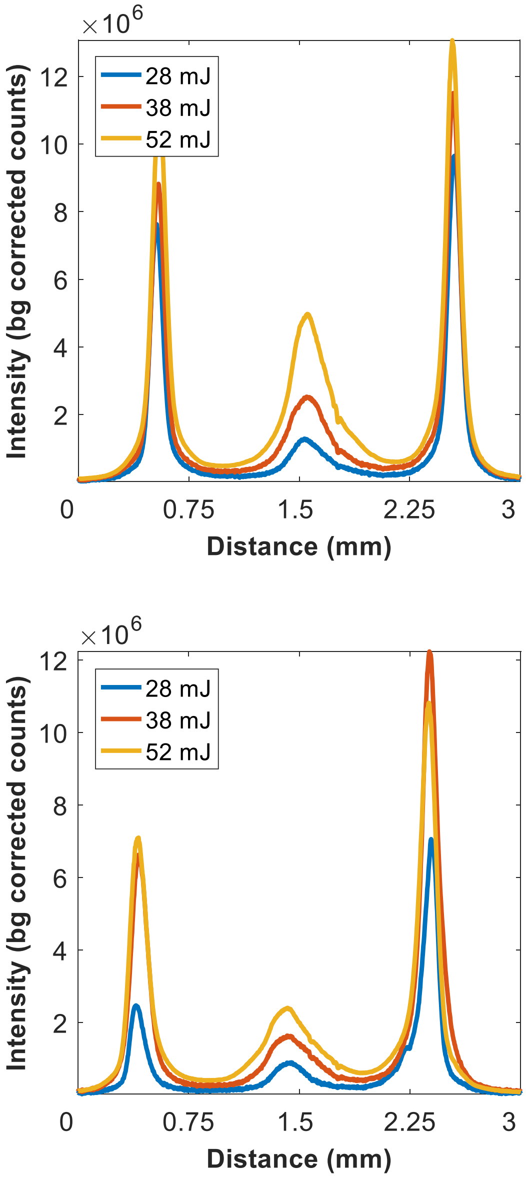

Figure 4.14: Head on, space resolved, time integrated broadband intensity distribution of an annular plasma at an ambient pressure of 1x10^{-2} mbar (top) and 1x10^{-5} mbar (bottom) for each laser pulse energy.

The head on intensity distribution curves, in Figure 4.14 show a tighter stagnation layer in the case of an annular plasma. This is attributed to the symmetry of the annular seed plasma which is to be compared to the two point seed plasma cases, which have already been shown to result in an asymmetric stagnation layer.

4.2 Time Resolved Broadband Imaging

4.2.1 Time Resolved, Broadband Imaging of a Single Plasma.

The time resolved imaging results shown in the section were taken at delay times of 10 ns, 50 ns, and 80 ns after plasma ignition. These delays were chosen as they correspond, respectively, to the époque of plasma formation, the time at which the stagnation layer begins to form and the time when the initial plasma has died away and the stagnation layer is the dominant emitting region of the colliding plasma system. The images are all taken at a fixed laser pulse energy of 52 mJ and for two different background air pressures, namely $1x10^{-2}$ mbar and $1x10^{-2}$ mbar. The point plasma images are shown in Figure 4. and Figure 4. as side on and head on viewpoints respectively. The dual colliding point plasma images are shown in Figure 4. and Figure 4. while the annular colliding plasmas are shown in Figure 4.19 and Figure 4.20

Side on time resolved imaging of a single plasma (Figure 4.) shows its free expansion from the target surface. At early times the emitting size of plasma is quite spherical and small in spatial extent (at least on an intensity scale with a peak counts of 10^3 or so). At longer time delays the plasma plume departs from a spherical shape and appears as a double lobe-like structure for both background air pressures. The image intensities in counts drop quickly over the time delay range from 10ns to 80 ns, from ca. 1000 to ca. low double digit values in both cases. The images c & f of Figure 4. show an extended and diffuse region of weak emission surrounding the plasma plume.

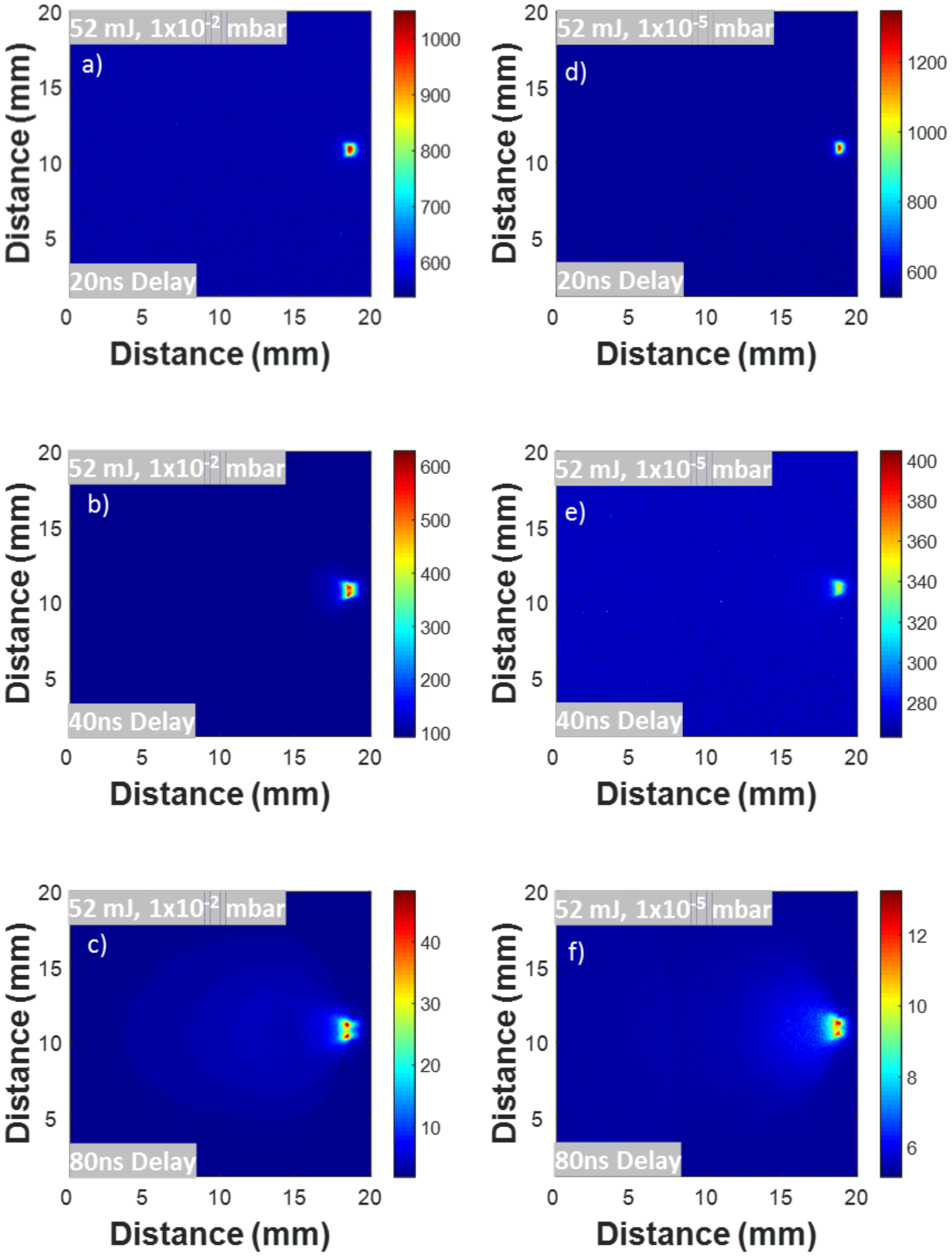

Figure 4.15: Side on time resolved broadband images of a single aluminium plasma at an ambient pressure of 1x10^{-2}mbar (left hand side) and 1x10^{-5} mbar (right hand side), with laser pulse energy of 52 mJ at a delay of a, d) 10 ns, b, e) 50 ns and c, f) 80 ns from plasma ignition.

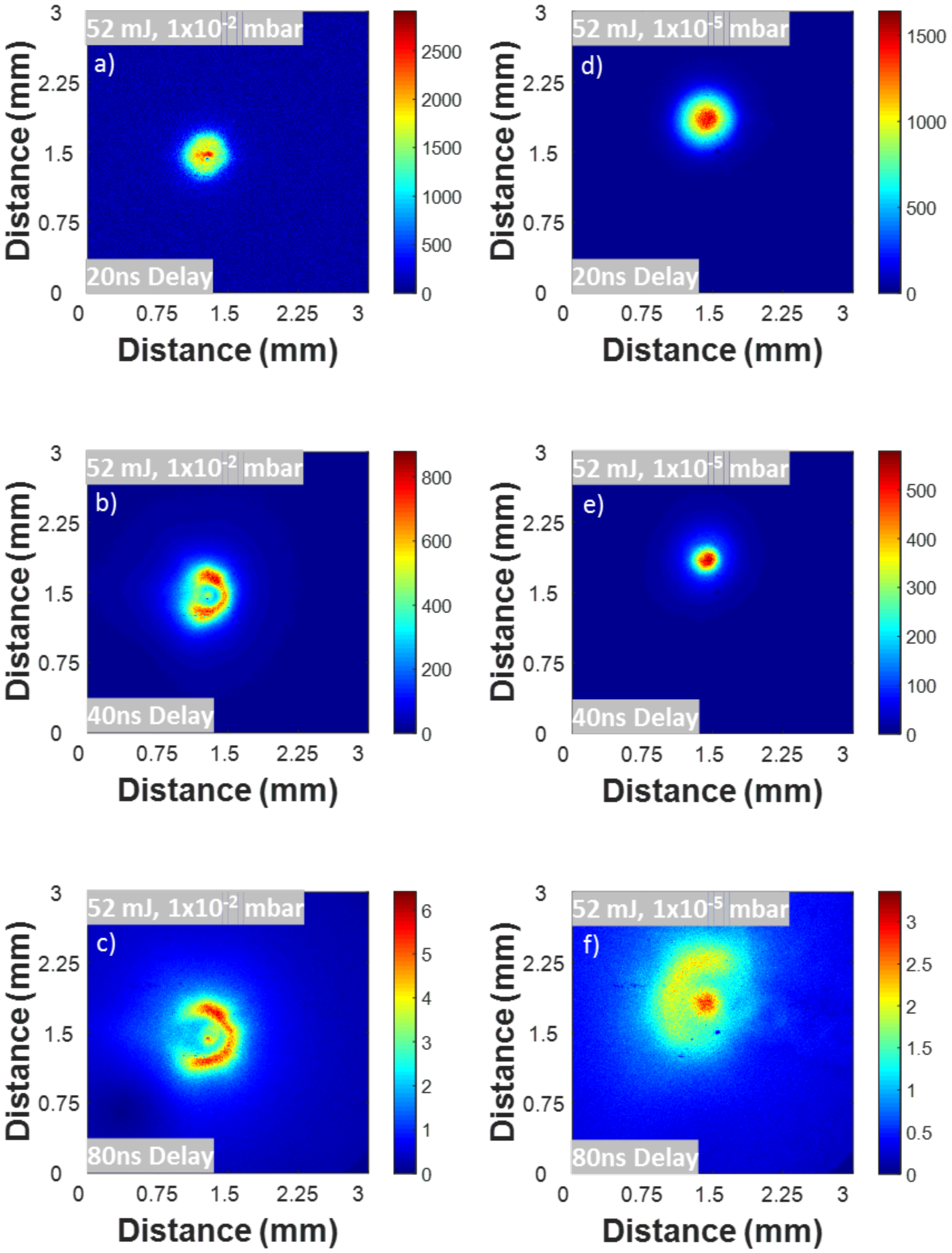

Figure 4.16: Head on time resolved broadband images of a single aluminium plasma at an ambient pressure of 1x10^{-2}mbar (left hand side) and 1x10^{-5} mbar (left hand side), with a laser pulse energy of 52 mJ at delays of a, d) 10 ns, b, e) 50 ns and c, f) 80 ns from plasma ignition.

This may be due to shockwave heating of the surrounding gas. In the higher pressure case the shock wave heated region is smaller than in the low pressure case (10^{-5} mbar) where the heated gas region appears to be weaker but larger in spatial extent. The origin of the asymmetry, which appears as a double lobe structure in the side-on images is as yet unclear. It could be due to the mode structure in the laser beam. The Nd:YAG laser used in this work had a cavity designed for optimal mode filling and the far field beam deviated <5% from Gaussian. However, it was clear that the beam profile was adversely affected by the double attenuator leading to hot modes in the output. Head-on imaging shows similarly bright emission and a similar rapid falloff in intensity. Although initially quite spherical in shape, the image become quite asymmetric as time proceeds, in contrast to stagnation layers for which tend to keep their shape tends as time proceeds.

4.2.2 Time Resolved, Broadband Imaging of Two Colliding Seed Plasmas.

The formation and expansion of the seed plasmas, which are separated by ca. 2.5 mm, is shown at both high and low pressures in Figure 4. and Figure 4. for time delays of 20 ns, 40 ns and 80 ns. Images are shown for a laser pulse energy of 52 mJ and for the usual pair of background gas pressures, namely 10^{-2} mbar and 10^{-5} mbar. It can be seen that they, as expected, exhibit similar stagnation layer formation times. It is clear that at 40 ns, although the point plasmas have expanded, they have not yet interacted and there is no clear evidence of a stagnation layer. By 80 ns the stagnation layers have formed in both cases (10^{-2} and 10^{-5} mbar) and the seed plasma emission is quite weak. At this early stage there appears to be little difference between the stagnation layers, save for a small difference in the peak intensity.

Once again the brightness (in counts) of the point seed plasmas falls away quite rapidly with time delay from above 3000 counts to below 30 counts going from 20 ns to 80 ns. In fact the stagnation layer emission exceeds that of the seed plasmas at 80 ns.

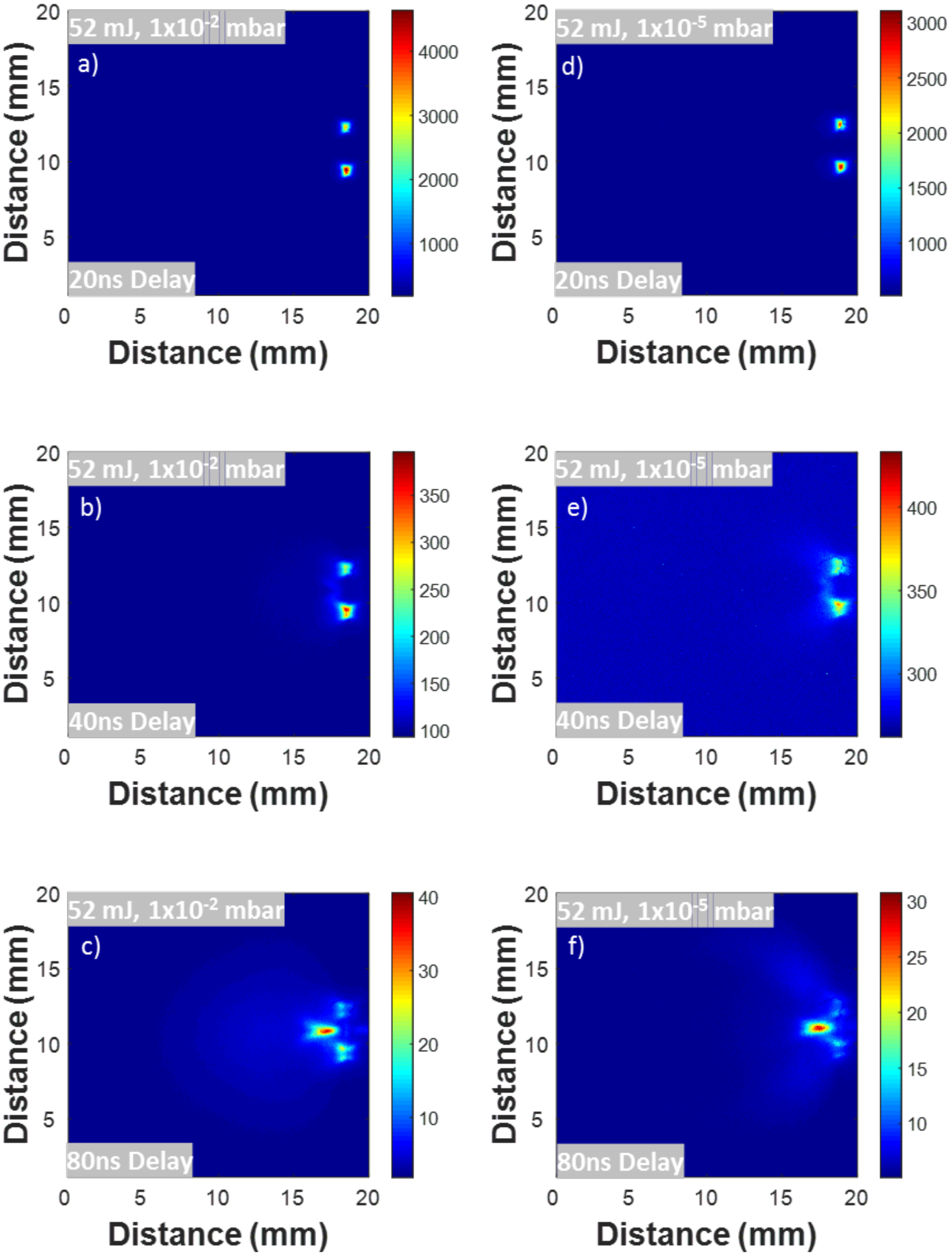

Figure 4.17: Side on time resolved broadband images of two aluminium seed plasmas, and resulting stagnation layer at an ambient pressure of $1x10^{-2}$mbar (left hand side) and $1x10^{-5}$ mbar (right hand side), for a laser pulse energy of 52 mJ at a delay of a, d) 20 ns, b, e) 40 ns and c, f) 80 ns from plasma ignition.

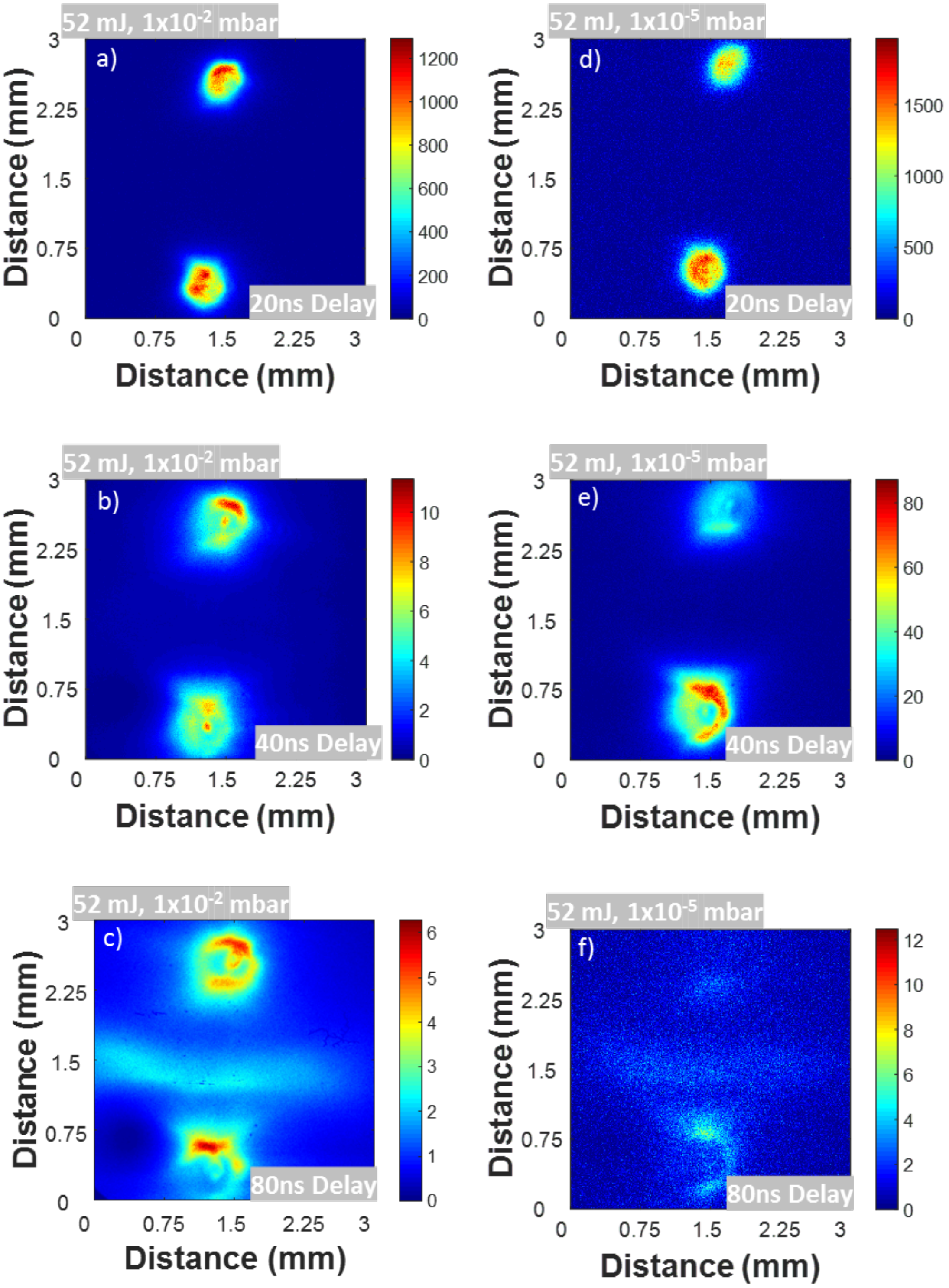

Figure 4.18: Head on time resolved broadband images of two aluminium seed plasmas, and resulting stagnation layer, at an ambient pressure of 1x10^{-2}mbar (left hand side) and 1x10^{-5} mbar (left hand side), for a laser pulse energy of 52 mJ at delays of a, d) 20 ns, b, e) 40 ns and c, f) 80 ns from plasma ignition.

Looking now to the image obtained by viewing the dual colliding plasma system head on, there is a somewhat rectangular shape to the stagnation layer formed between the two seed plasmas. In fact this is consistent with another measurement of the stagnation layer formed between two point-like seed plasmas that looked from both the side and the top of the collision [3]. In that study it was observed that the stagnation layer assumed an oblate shape as per for example Figure 4.17 (c and f). The images are consistent with Figure 4.18 where, although the seed plasmas have expanded, the stagnation layer does not appear at the 40 ns time delay. The seed plasma intensities again decrease by two orders of magnitude between 20 ns and 80 ns, again consistent with Figure 4.18.

4.2.3 Time Resolved, Broadband Imaging of an Annular Plasma.

Images for annular colliding plasmas are shown for a laser pulse energy of 52 mJ, time delays of 20, 40 and 80 ns for background air pressures of $1x10^{-5}$ mbar and $1x10^{-2}$ mbar for both side on (Figure 4.19) and head on (Figure 4.20) viewpoints. These images are clearly very different from the dual colliding point plasma cases, most especially the stagnation layer forms a good deal earlier in the case of annular colliding plasmas. It’s also clear that the intensity of the seed (ring) plasma falls away quite quickly and its expansion energy is converted quite efficiently into stagnation layer brightness by a time delay of 40 ns (compare annular plasma peak intensity of ca. 2500 counts with the stagnation layer intensity of 1500 counts, quite different to the dual point colliding plasma cases). As the irradiance on target is two orders of magnitude lower in the annular plasma compared to the point plasmas, one would expect the absolute emission intensity to be lower and closer to the stagnation layer brightness, as observed. The layer intensity only decays slowly between 40 ns and 80 ns highlighting one of the advantages of this stagnation layer, sustained emission over a considerable period.

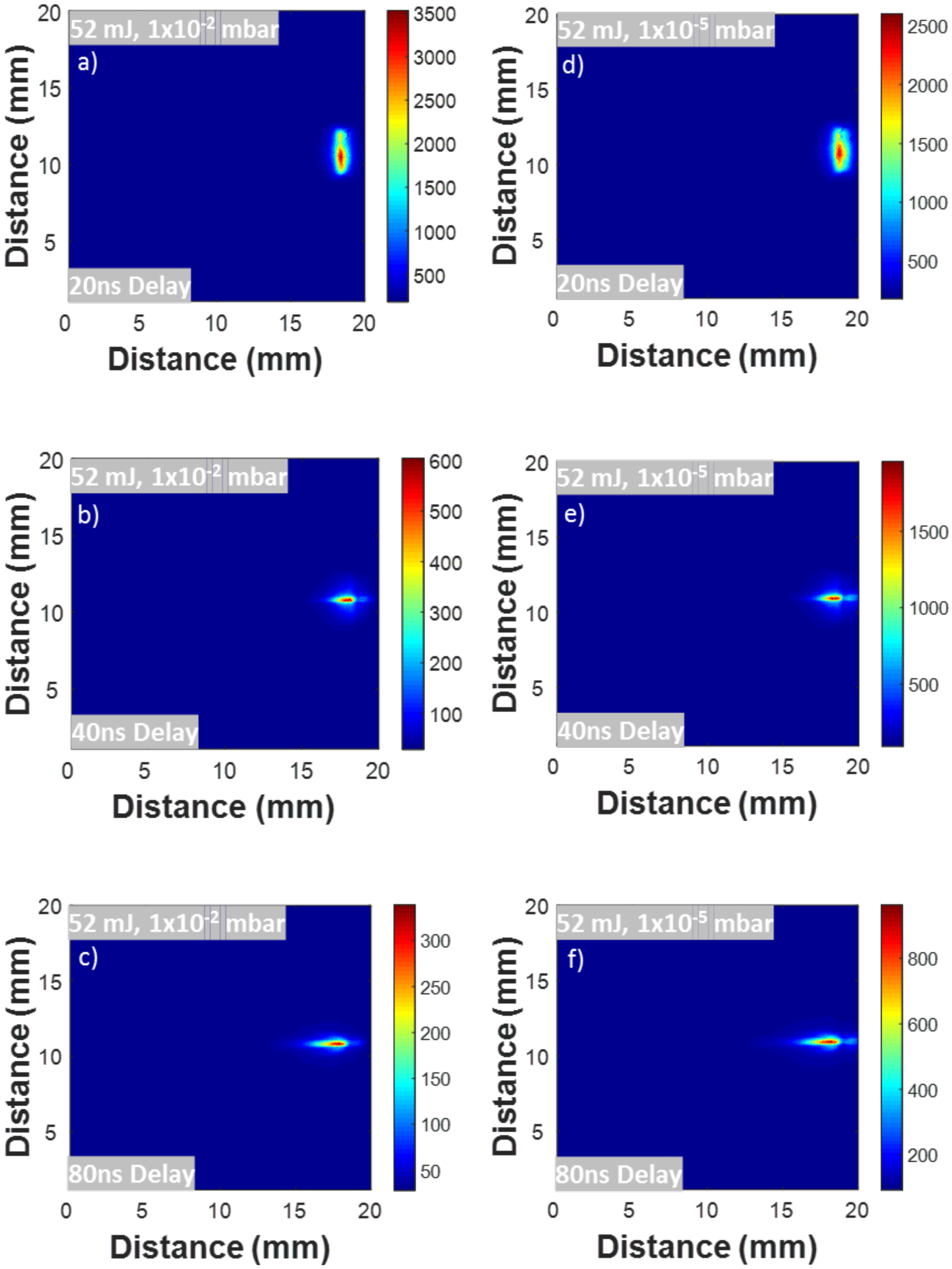

Figure 4.19: Side on time resolved broadband images of an annular aluminium plasma, and resulting stagnation layer, at an ambient pressure of 1x10^{-2}mbar (left hand side) and 1x10^{-5} mbar (right hand side), for a laser pulse energy of 52 mJ at delays of a, d) 20 ns, b, e) 40 ns and c, f) 80 ns from plasma ignition.

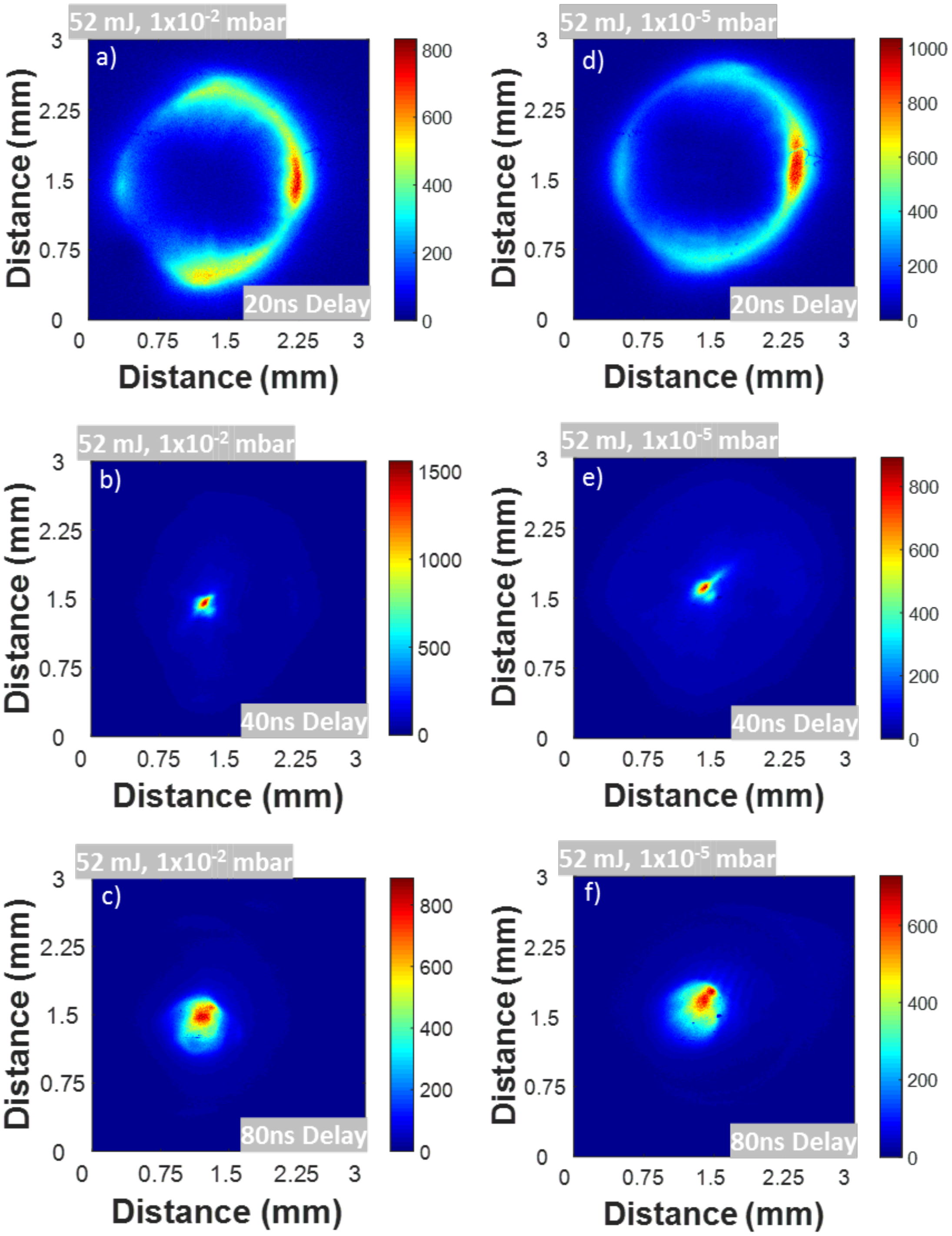

Figure 4.20: Head on time resolved broadband images of an annular aluminium plasma, and resulting stagnation layer, at an ambient pressure of $1x10^{-2}$mbar (left hand side) and $1x10^{-5}$ mbar (left hand side), for a laser energy of 52 mJ at delays of a, d) 20 ns, b, e) 40 ns and c, f) 80 ns from plasma ignition.

The formation of the stagnation layer early is perhaps somewhat surprising, even if the ring diameter is ca. 2 mm compared to the ca. 3 mm separation for the point plasmas. That is because the point plasmas should be hotter and hence reach the collision plane more quickly. It is perhaps more likely that, as the seed annular plasma and stagnation layers have comparable intensity, these images display better contrast between seed and stagnation layer making the latter more visible at earlier time delays.

The time resolved imaging also allows for a much clearer image of the initial (or seed) annular plasma to be captured. It can be seen that the annulus is not perfectly symmetric and this results in an asymmetric intensity distribution in the corresponding stagnation layers. It can also be seem that the layer formed is quite tight at a time delay of 40 ns but then expands quite rapidly, radially, with time.

4.2.4 Time Resolved Plume Front Positions

Figure 4.21 shows the plasma expansion data for the single plume, dual colliding plume and colliding annular plasmas in a background air pressure of $1x10^{-2}$ mbar. Figure 4.22 shows the corresponding measurements in a background air pressure of $1x10^{-5}$ mbar. All data were taken for a pulse energy of 52 mJ. The plume front positions presented were extracted from the full set of time resolved broadband images. Plume fronts were obtained using the methodology outlined in section 3.2.1. 'Plume front' in the cases of dual and annular colliding plasmas means 'stagnation layer front'. The first data point in each case corresponds to a time delay of 40 ns, the time at which stagnation layers begin to form (Figure 4.(e)) or have already formed (Figure 4.(e)).

The first observation that can be made is that the rate of plume expansion differs for each plasma configuration and also differs between pressures. Making simple linear fits to each of the plots one obtain approximates plume expansion rates (Table 4.1).

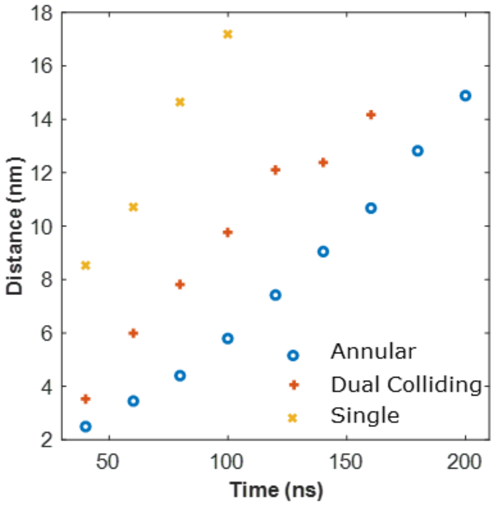

Figure 4.21: Plume front position for a single plasma, two seed plasmas and an annular plasma at an ambient pressure of $1x10^{-2}$ mbar with a laser pulse energy of 52 mJ. The front is taken as the position on a lineout, normal to the target and along the centre line of plasma (or stagnation layer), at which the intensity has dropped to 10% of its peak value. Single plume (yellow X's), dual colliding plasmas (red crosses) and annular colliding plasma (blue circles).

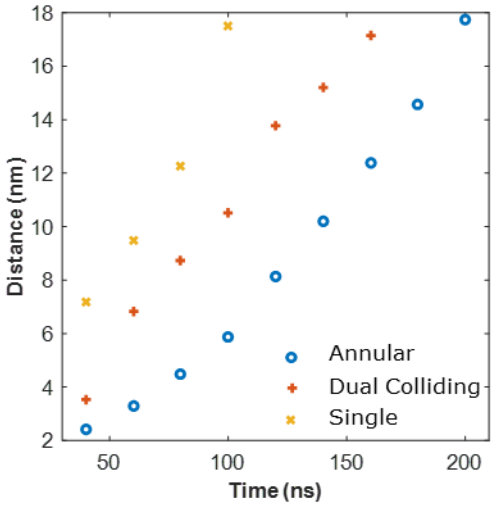

Figure 4.22: Plume front position for a single plasma, two seed plasmas and an annular plasma at an ambient pressure $1x10^{-5}$ mbar with a laser pulse energy of 52 mJ. The front is taken as the position on a lineout along the plasma (or stagnation layer) at which the intensity has dropped to 10% of its peak value. Single plume (yellow X's), dual colliding plasmas (red crosses) and annular colliding plasma (blue circles).

Table 4.1: Expansion velocities obtained from figures 4.21 and 4.22.

Pressure	10^{-2} mbar	10^{-5} mbar
Seed Plasma Type		
Single	1.66×10^{7} cm.sec^{-1}	1.86×10^{7} cm.sec^{-1}
Dual Colliding	1.00×10^{7} cm.sec^{-1}	1.17×10^{7} cm.sec^{-1}
Annular	0.75×10^{7} cm.sec^{-1}	0.95×10^{7} cm.sec^{-1}

So the expansion rate is (20±5)% faster at the lower pressure of 10^{-5} mbar. Also the ratio of the expansion rates for each plasma configuration SP : DP : AP is 3.0: 1.8 :1.4 with an error of ±0.1 for both background air pressure values. The values are not untypical for stagnation layers and laser plasma plumes which exhibit expansion velocities in the few 10^{6} to early 10^{7} cm.sec^{-1} range [3],[17].

4.3 Summary

Time integrated and time resolved broadband images of plasmas formed using three different laser focusing schemes have been presented, namely a single plasma plume formed a point focus using a simple plano-convex lens, a pair of such plasmas formed side by side on a slab target and an annular plasma formed by the combination of an axicon and a plano convex lens. Images of these plasma systems were taken both along and orthogonal to the plasma expansion axis and at two background pressures, namely 10^{-2} mbar and 10^{-5} mbar. Time integrated images show, not unexpectedly, that that the bulk of the emission intensity comes from point like plasmas, both single plume and dual colliding. In some cases the stagnation layer was quite visible in these images, e.g., Figures 4.5, 4.6, 4.9, 4.10, 4.11 and 4.12, most especially in the annular plasma case where the initial irradiance is some two order of magnitude lower than for the case of point plasmas and so the corresponding stagnation layer intensities tend to lie within the intensity of the annular seed plasma emission.

The time resolved images were taken mainly in the 40 ns to 200 ns time delay range, i.e., the time from stagnation layer begin to form to when they are well established. The results show that plume (single or stagnation) expansion rates are reduced somewhat (ca. 20%) at the higher pressure but that the ratios of plume expansion rates for the different optical plasma configurations are quite similar to each other (at least in the 10^{-2} mbar and 10^{-5} mbar background air pressure range).

Bibliography

[1] P. Hough *et al.*, “Ion emission in collisions between two laser-produced plasmas,” *J. Phys. D. Appl. Phys.*, Vol. 44, no. 35, Art. No. 355203, 2011.

[2] P. Hough *et al.*, “Electron and ion stagnation at the collision front between two laser produced plasmas,” *J. Phys. D. Appl. Phys.*, Vol. 42, no. 5, Art. No. 055211, 2009.

[3] P. Hough, C. McLoughlin, S. S. Harilal, J. P. Mosnier, and J. T. Costello, “Emission characteristics and dynamics of the stagnation layer in colliding laser produced plasmas,” *J. Appl. Phys.*, Vol. 107, no. 2, Art. No. 024904, 2010.

[4] N. Walsh, J. T. Costello, and T. J. Kelly, “Optical diagnostics of laser-produced aluminium plasmas under water,” *Appl. Phys. B*, Vol. 123, no. 6, Art. No. 179, 2017.

[5] S.S. Harilal, C. V. Bindhu, M. S. Tillack, f. Najmabadi and A. C. Gaeris, "Internal structure and expansion dynamics of laser ablation plumes into ambient gases", *J. Appl. Phys.*, Vol. 93, pp. 2380-2388, 2003.

[6] Y. H. Yoo, S.H. Jeong, R. Greif and R. E. Russo, "Explosive change in crater properties during high power nanosecond laser ablation of silicon", *J. Appl. Phys.*, Vol. 88, pp. 1638-1649, 2000.

[7] D. B. Geohegan, "Physics and diagnostics of laser ablation plume propagation for high Tc superconductor film growth", Thin Solid Films, Vol. 220, pp. 138-145, 1992.

[8] R. E. Russo X. L. Mao, XL, C. Liu, and J. Gonzalez, "Laser assisted plasma spectrochemistry: laser ablation", J. Anal. At. Spectrom., Vol. 19, pp. 1084-1089, 2004.

[9] L. St-Onge, E. Kwong, M. Sabsabi and E. B. Vadas, "Quantitative analysis of pharmaceutical products by laser-induced breakdown spectroscopy", Spectrochimica Acta Part B, Vol 57, pp. 1131–1140, 2002.

[10] I. Umezu, S. Yamamoto and A. Sugimura, "Emission induced by collision of two plumes during pulsed laser ablation", Appl. Phys. A., Vol. 101, pp. 133–136, 2010.

[11] L. M. Cabalın and J. J. Laserna, "Atomic emission spectroscopy of laser-induced plasmas generated with an annular-shaped laser beam", J. Anal. At. Spectrom., Vol. 19, pp. 445–450, 2004.

[12] S. S. Harilal, C. V. Bindhu and H.-J. Kunze, "Time evolution of colliding laser produced magnesium plasmas investigated using a pinhole camera ", J. Appl. Phys. Vol. 89, pp. 4737-4740, 2001.

[13] T. Atwee and H-J. Kunze, "Spectroscopic investigation of two equal colliding plasma plumes of boron nitride", J. Phys. D: Appl. Phys. Vol. 35, pp. 524-528, 2002

[14] H Luna, K D Kavanagh and J T Costello, "Study of a colliding laser-produced plasma by analysis of time- and space-resolved image spectra", J. Appl. Phys. 101, Art. No. 033302, 2007.

[15] X. Li, Z. Yang, J. Wu, J. Han, W. Wei, S. Jia and A. Qiu "The effect of target materials on colliding laser-produced plasmas", J. Appl. Phys. Vol. 119, Art. No. 133301, 2016.

[16] T. Sizyuk, J. Oliver and P. K. Diwakar, "Mechanisms of carbon dimer formation in colliding laser-produced carbon plasmas", J. Appl. Phys. Vol. 122, Art. No. 023303, 2017.

[17] C. Ursu, S. Gurlui, C. Focsa, and G. Popa, "Space- and time-resolved optical diagnosis for the study of laser ablation plasma dynamics", Nucl. Instrum. Methods Phys. Res. B Vol. 267, pp. 446-450, 2009

5. Spectroscopy and Plasma Diagnostics of Dual and Annular Colliding Plasmas

5.1 Plasma Spectroscopy

In order to gain greater insights into the plasma conditions pertaining in the stagnation layers formed by both dual colliding and annular colliding plasmas space integrated emission spectra of these entities were obtained in the optical region of the electromagnetic spectrum. Space integrated but time resolved spectra were also recorded so that the evolution of the plasma parameters, specifically the electron density and electron temperature, in the stagnation layers could be tracked. All spectra were recorded on a 0.5 Czerny-Turner spectrometer with ICCD readout as described in Chapter 3. All spectra were fully vertically binned so that all spectra presented in this chapter are space integrated.

The primary lines of interest for spectroscopy of both dual colliding and annular colliding plasma systems comprised neutral, singly and doubly ionised lines of aluminium [1,2] which have been used extensively in laser plasma spectroscopy for diagnostic purposes [3 - 11] in the past. The neutral lines (394.40 nm and 396.15 nm) are present in the spectral window centred at 394nm captured by the spectrometer. The singly (466.44 nm) and doubly (451.26 nm and 452.89 nm) ionised Al lines were present in the window centred at 460nm. They can be used for both electron density determination via Stark broadening [12-14] and also electron temperature determination via line intensity ratios, especially for line originating from successive charge states [15-18].

5.1.1 Time and Space Integrated Spectroscopy

The spectrometer has been (relative) intensity calibrated and the efficiency does not vary much within any one spectral window. Thus, the choice of these close lines allow for an almost direct intensity comparison. The same optical systems were used to focus the colliding plasma systems onto the entrance slit of the spectrometer, namely a relay lens system for side on views and a parabolic reflector with a focusing lens for head on views.

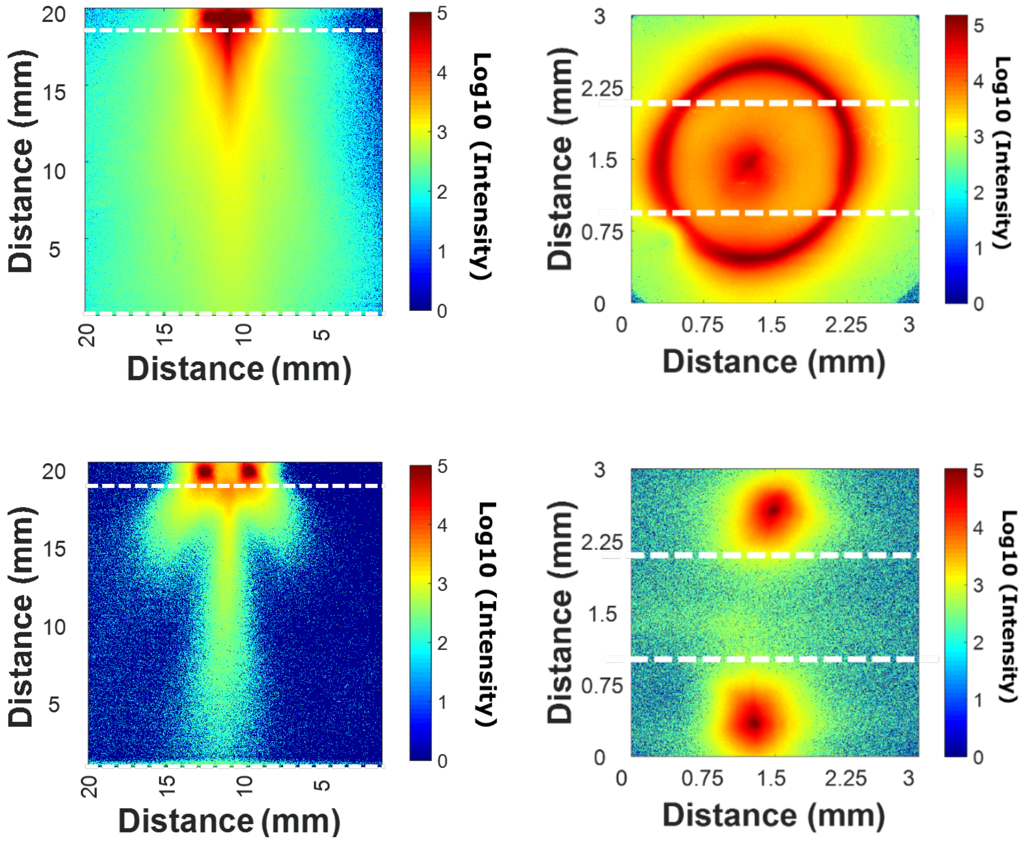

Figure 5.1: Broadband time integrated images indicating the bounds of partial binning (i.e., the region between the dashed white lines) for both an annular colliding plasma (top) and dual colliding seed plasma (bottom) and for the side-on (left) and head-on (right) viewing cases.

The stagnation layers formed focused onto the vertical entrance slit so that they expanded up along the slit (i.e., along the direction of spatial resolution, as the spectrometer was stigmatic). Figure 5.1 shows the areas of interest which were binned in both the annular (top panels) and dual colliding plasma (bottom panels) cases. The side view spectral images encompassed a lineout extending from the close to the target surface out to a distance of 20 mm. Spectral images were useful since they could be easily cropped to exclude the annular seed plasma from the presented spectra. The same binning was also carried out in the dual colliding plasmas case to exclude the point-like seed plasmas. Partial binning was also carried out in the head on case; this binning excluded the seed plasmas in the dual colliding case where the area of interest was confined to the stagnation layer itself. Similarly, in the annular case the binning excludes the top and bottom of the annulus while the slit is aligned with the centre of the annulus, excluding the left and right of the annulus. In principle, for the dual colliding case, the entrance slit excluded the seed plasmas due to its narrow width. However, the images were still cropped to make the area of interest the same as that for the annular colliding plasma case.

The spectral lines of interest in neutral, singly ionized and doubly ionized aluminium are given in the table 5.1 below.

*Table 5.1****:*** *Transitions of interest in Al, Al^+ and Al^{2+} for diagnostic purposes.*

Ion	**Lower State**	**Upper State**	**Wavelength (nm)**
Al^0	$3s^24p\ ^2P_{1/2}$	$3s^24s\ ^2S_{1/2}$	394.40
Al^0	$3s^24p\ ^2P_{3/2}$	$3s^24s\ ^2S_{1/2}$	396.15
Al^+	$3p^2\ ^1D_1$	$3s4p\ ^1P_1$	466.31
Al^{2+}	$2p^64p\ ^2P_{1/2}$	$2p^64d\ ^2D_{3/2}$	451.26
Al^{2+}	$2p^64p\ ^2P_{3/2}$	$2p^64d\ ^2D_{3/2}$	452.89

*Table 5.2****:*** *Other lines identified in the Al spectra obtained.*

Ion	**Lower State**	**Upper State**	**Wavelength (nm)**
Al^+	$3s3p\ ^1P_1$	$3p^2\ ^1D_2$	390.07
O^+	$2s^22p^2(^3P)3p\ ^4D_{5/2}$	$2s^22p^2(^3P)3d\ ^4P_{5/2}$	390.75
O^+	$2s^22p^2(^1D)3s\ ^2D_{3/2,5/2}$	$2s^22p^2(^1D)3p\ ^2P_{3/2}$	391.20
O^+	$2s^22p^2(^3P)3s\ ^4P_{3/2}$	$2s^22p^2(^3P)3p\ ^4D_{5/2}$	464.18
Al^{3+}	$2s^22p^5(^2P_{1/2})4s\ ^2[1/2]_1$	$2s^22p^5(^2P_{1/2})4p\ ^2[3/2]_1$	462.61
O^{2+}	$2s^22p(^2P°)4p\ ^3P_0$	$2s^22p(^2P°)5s\ ^3P_1$	463.08
O^+	$2s^22p^2(^3P)3s\ ^4P_{5/2}$	$2s^22p^2(^3P)3p\ ^4D_{7/2}$	464.91
Al^+	$3s4d\ ^1D_2$	$3s10p\ ^1P_1$	464.86

Oxygen contamination of Al targets is not unusual and so it is no surprise to see lowly ionized oxygen emission in the spectra. In the high pressure (10^{-2} mbar) (Figure 5.2) and the low pressure (10^{-5} mbar) (Figure 5.3) cases the intensity of the neutral lines at 394 nm and 396 nm, corresponding to the Al doublet, 3p ($^2P_{1/2,3/2}$) – 4s ($^2S_{1/2}$) transitions, for the point and annular colliding plasma plumes are on the same intensity scale but not equal. The line intensities for the dual colliding plasmas case are slightly less than those for the annular plasma system. It is also clear that the line intensities in the low pressure (10^{-2} mbar) case (Figure 5.3) are reduced by a factor of 2 compared to the 10^{-2} mbar case (Figure 5.2). To gain further insight it is best to look at the singly and doubly charged ion spectra in these figures.

Hence turning to the spectra in the 450 – 467 nm range where emission lines associated with singly and doubly charged ions appear, the spectra for the high pressure (10^{-2} mbar) (Figure 5.2) and low pressure (10^{-5} mbar) (Figure 5.3) cases are quite different. For the former the stagnation layer formed by the dual colliding plasma plumes yields the more intense lines while at low pressure (10^{-5} mbar, i.e., effectively in vacuo) the spectral signal from the doubly ionised lines for the annular colliding plasma case is approximately eight times that produced in the other two cases {i.e., for the biprism in vacuo (Figure 5.3) and both the axicon and the biprism in the higher pressure case (Figure 5.2)}. This rather strange looking result has yet to be fully understood but the spectra and their processing have been checked and rechecked and the result remains as shown.

As the spectra are space and time integrated, it seems clear that the annular colliding plasma system, at 10^{-5} mbar, has conditions optimised for the formation of excited doubly charged ions. This may also explain why the emission from atomic aluminium is weakest in this case. Returning to the comparison of the Al^{2+} lines in Figure 5.2 and Figure 5.3, it may also be the case that at higher pressure (10^{-2} mbar) emission from more highly charged ions is weaker. Hence the doubly charged ion density is lower. The only difference between the two cases is the background air pressure. At 10^{-2} mbar the number density of air molecules is $\sim 2.7 \times 10^{16}$ cm^{-3}. The charge exchange cross section for ion velocities of ca. 10^{6} cm.sec^{-1} is typically 100 MB [19,20]. Hence the charge exchange rate would be typically 2.7×10^{6} sec^{-1}.

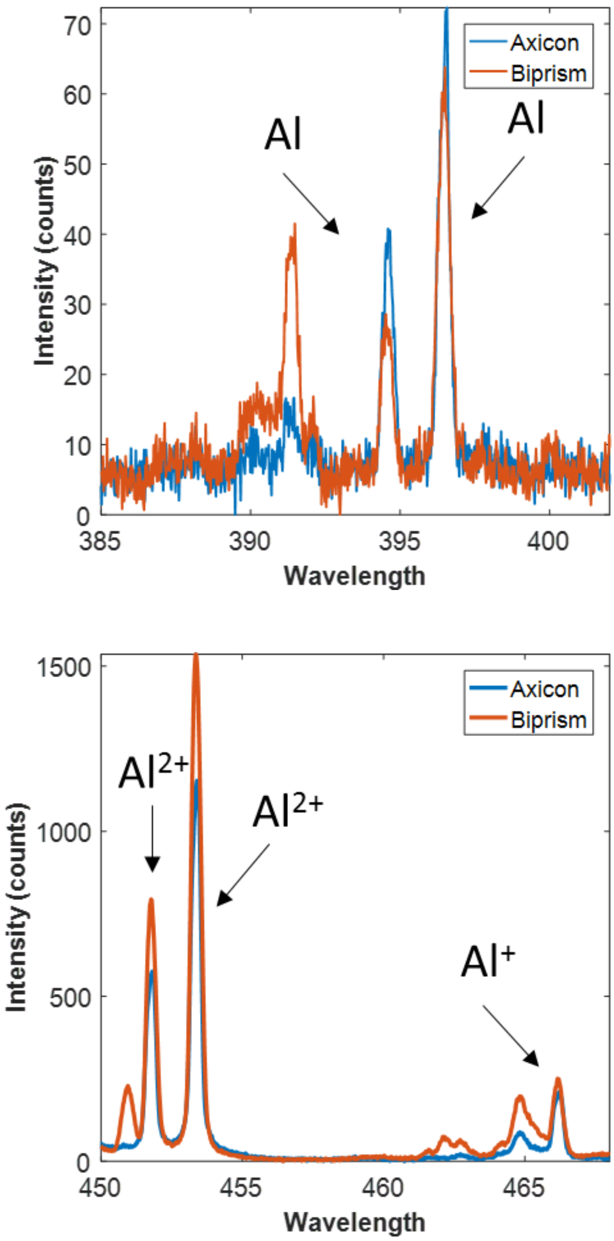

Figure 5.2: Side-on, time integrated spectra of both annular and dual colliding plasmas at an ambient pressure of 1x10^{-2} mbar, for a laser pulse energy of 52 mJ. The spectrometer was centred at 394 nm (top) and 460 nm (bottom).

Assuming the emission time to be 500 ns, this corresponds to ca. 1.5 events per ion taking place during the exposure time for each figure 5.2 and 5.3. As a result it is likely that most 2+ ions were inhibited in that time. Since the charge exchange probability scales linearly with air molecule number density, the rate at 10^{-5} mbar is three orders of magnitude lower and hence negligible.

Looking to the singly ionised aluminium emission line at 466.3 nm, one observes a similar trend. The Al^+ intensity, for the annular colliding plasma system, is more than five times higher for the low pressure (10^{-5} mbar) environment, compared to the spectrum recorded at a background air pressure of 10^{-2} mbar. As before, at 10^{-2} mbar the line intensity is almost the same for the colliding plasmas formed with the aid of both the biprism and axicon.

In summary, at 10^{-2} mbar, both dual colliding and annular colliding plasma systems produce stagnation layers with similar ion emission intensities. At 10^{-5} mbar, the axicon appears to produce a colliding plasma system, and resulting stagnation layer, optimised for singly and doubly charged species. The exact mechanism underlying this significant difference with the dual colliding plasma system is not yet clear from these time integrated spectra. Strong emission from the initial ring plasma was excluded by selecting the area of interest shown in Figure 5.1 and can be eliminated as a cause. Of course, as time proceeds and the ring expands and one cannot exclude some leakage into the imaged area of interest. The on-target laser irradiance in the case of the point seed plasmas (dual colliding plasmas), is $\sim 10^{11}$ W/cm^2 or ca. two orders of magnitude greater than the annular (seed) plasma case. The estimated initial temperature for the point like seed plasmas is 30 to 40 eV and is hence ca. 10 - 20 times higher than the annular seed plasma case, using Equation 29 from section 2.5.3, which was taken from Colombant and Tonon [21]. Hence for the dual colliding plasmas case one would expect most of the laser energy to be coupled into generating much more highly ionized species than those recorded here, at least during the early stages of seed plasma formation.

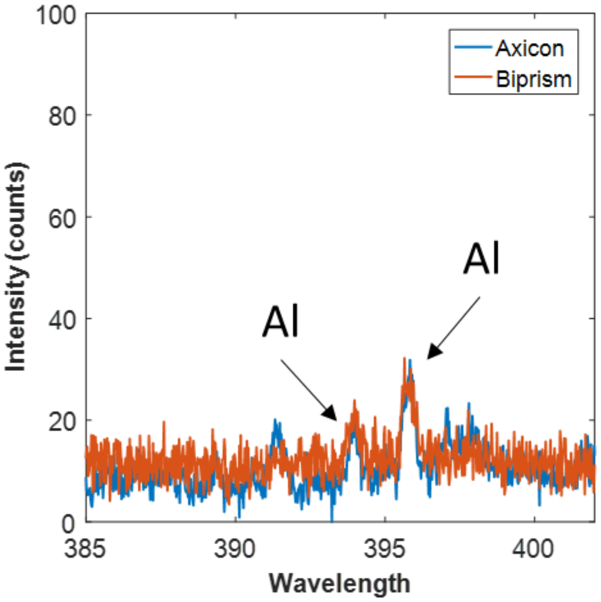

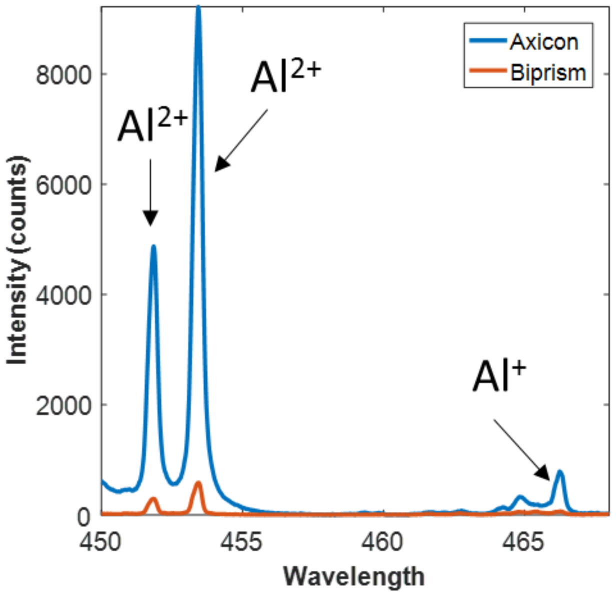

Figure 5.3: Side-on, time integrated spectra, of both annular and dual colliding plasmas at an ambient pressure of 1x10^{-5} mbar, for a laser pulse energy of 52 mJ. The spectrometer was centred at 394 nm (top) and 460 nm (bottom).

For the annular plasmas, at an initial temperature of ca. 5 eV, which is expected at an irradiance of a few 10^9 W/cm^2, the dominant species are singly and doubly ionized aluminium ions. At 10^{-5} mbar, effectively in vacuo, one could expect these to be transported to the stagnation layer without strong electron-ion recombination having occurred, for either singly or doubly charged species.

The time and space integrated spectra obtained by viewing each stagnation layer head-on are shown below for the high pressure (10^{-2} mbar) and low pressure (10^{-5} mbar) cases in Figure 5.4 and Figure 5.5 respectively. Looking first to the Al I spectrum in the vicinity of 395 nm, it is clear that the Al doublet line intensity ratio is in general comparable to that observed in the spectrum obtained by viewing the plasma side on, albeit it is about a factor of two higher in absolute counts. This is perhaps not surprising as the collecting optic is f/1 in this case and hence has very strong light gathering power. It is clear that the Al doublet intensity ratio is far from the expected statistical value of 2 in all spectra except for the axicon assisted plasma spectrum shown in Figure 5.4, i.e., at a background air pressure 10^{-2} mbar in the target chamber. Since the 396 nm transition ends on a state with a higher total angular momentum (J = 3/2, statistical weight 2J + 1 = 4), one would expect this line to suffer greater absorption in the stagnation layer. On the other hand the 394 nm line has a statistical weight of 2 and will have an opacity some e^2 (ca. factor of 7) lower. Hence it is a more reliable feature for comparing line intensities for different pressures and between the colliding plasma systems (and resulting stagnation layers) formed with the aid of the axicon and biprism.

Looking to the 394 nm line intensity it is clear that it is higher for the annular colliding plasma system than the dual colliding plasma system at the higher pressure (Figure 5.4, 10^{-2} mbar). However the 394 nm line intensity is slightly lower in dual colliding plasma case at the lower pressure (Figure 5.5, 10^{-5} mbar).

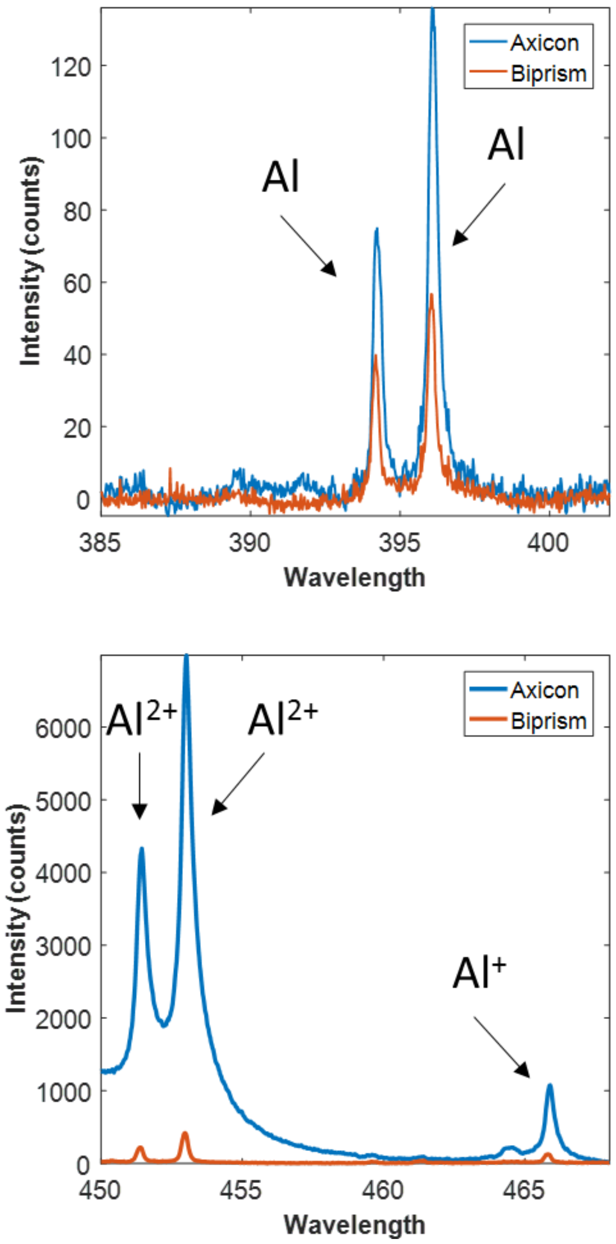

Figure 5.4: Head-on, time integrated spectra, for both annular and dual colliding plasmas, at an ambient pressure of $1x10^{-2}$ mbar, for a laser pulse energy of 52 mJ. The spectrometer was centred at 394 nm (top) and 460 nm (bottom).

In addition the line intensity ratio in Figure 5.5 is smaller for both colliding plasma systems compared to Figure 5.4 indicating higher opacity at lower ambient air pressure (10^{-5} mbar).

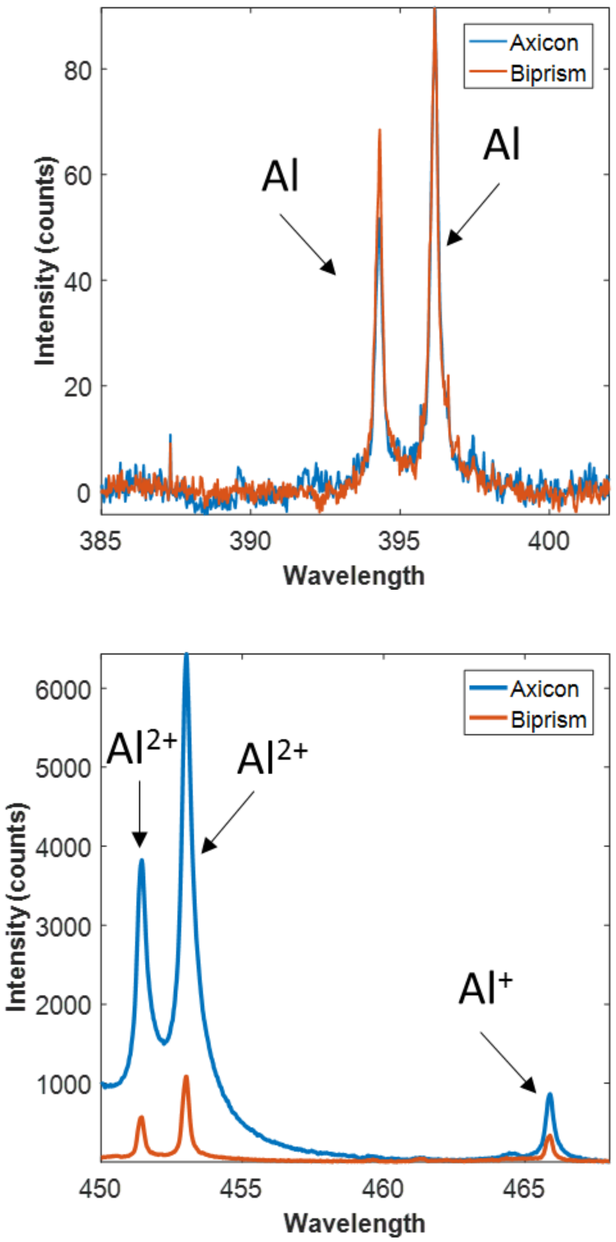

Figure 5.5: Head-on, time integrated spectra, for both annular and dual colliding plasmas, at an ambient pressure of $1\text{x}10^{-5}$ mbar, for a laser energy of 52 mJ. The spectrometer was centred at 394 nm (top) and 460 nm (bottom).

Lower opacity implies a lower ground state atomic density along the path of the radiation as that radiation is generated and passes down along each stagnation layer. Hence it must be concluded that collisions of each stagnation layer, as it is formed, with the background air results in a higher population of excited atomic species than in the 10^{-2} mbar compared to the 10^{-5} mbar case.

In the case of the axicon at higher pressure, where there is almost no evidence of opacity affecting the doublet line intensity ratio, one must conclude that there is a very uniform plasma column in terms of temperature, density and excited atomic species with almost no significant population of ground state species. This uniformity of plasma parameters is a desirable hallmark of stagnation layers for applications [22,23].

Moving now to the 465 nm spectral region it can be seen the annular colliding plasma spectra are quite similar at both low and high pressures, with very slightly higher intensities observed at the higher pressure, i.e., at 10^{-2} mbar. The peak intensity values are about half of those measured for spectra recorded in side on geometry (Figure 5.3, 10^{-5} mbar).

On the other hand the dual colliding plasma spectra intensities are quite different at the two different pressures. Specifically the intensity at low background air pressure (10^{-5} mbar) is about three times higher than observed at high pressure (10^{-2} mbar). This applies to the both the Al^{2+} and Al^{+} lines. It appears that, for the dual colliding plasma case, the higher pressure quenches the ions via recombination processes and reduces their relative populations and hence the corresponding spectral signals.

One final note of caution. Since the imaging and collection geometries are quite different, one cannot rule out their effect on these space integrated spectra. The f/1 parabola will view the end of the stagnation layer as a point source producing a parallel beam that is imaged onto the spectrometer slit by a f/8 lens. Assuming a radial distribution that is reasonably uniform with little shot to shot spatial jitter (found true in practice, especially for stagnation layers formed with axicons), one would expect the spectra to be not too sensitive to small optical misalignments between experiments. In the side-on view, where the stagnation layer is aligned with the slit, and imaged onto it using a relay lens system, small lateral misalignments could result in imaging of different regions of the stagnation layer. Longitudinal variations in ionization and excitation balance along with opacity could thus give rise to somewhat different spectra.

5.1.2 Time Resolved and Space Integrated Spectroscopy

Time resolved spectroscopic data are presented at delays of 100 ns, 200 ns and 300 ns from plasma ignition. These times were chosen as the spectra acquired during the early plasma lifetime (< 50 ns) were dominated by continuum emission and hence could not be used to distinguish between different ion stages in the stagnation layers imaged onto the entrance slit of the spectrometer.

From Figure 5.6, which shows spectra obtained by side-on viewing at 10^{-2} mbar, it can be seen that neutral line emission intensities are very similar for both the annular and dual colliding plasma systems. The lines are weak and grow in intensity as the time proceeds as the stagnation layers begin to be formed in the imaged areas of interest. Although initially the annular plasma system yields the brighter line emission, by 300 ns both annular and dual colliding plasmas produce an Al doublet with close to equal line intensities at an ambient air pressure of 10^{-2} mbar. It is also clear from the actual value of intensity ratio of the Al doublet that the opacity of the stagnation layer grows with time on moving from a delay of 100 ns to 300 ns. The atomic aluminium lines at 394 nm and 396 nm are also very weak in comparison to the doubly ionized Al lines indicating a higher temperature in the region of interest imaged by the spectrometer and ICCD. Indeed the Al^{2+} lines are stronger than the Al^{+} line at 466 nm, albeit this line grows slightly in relative intensity with time delay. From a quick comparison with the collisional radiative model of Colombant and Tonon [21] one would expect the electron temperature to reside in the region of 5-10 eV for Al^{2+} to dominate the spectra.

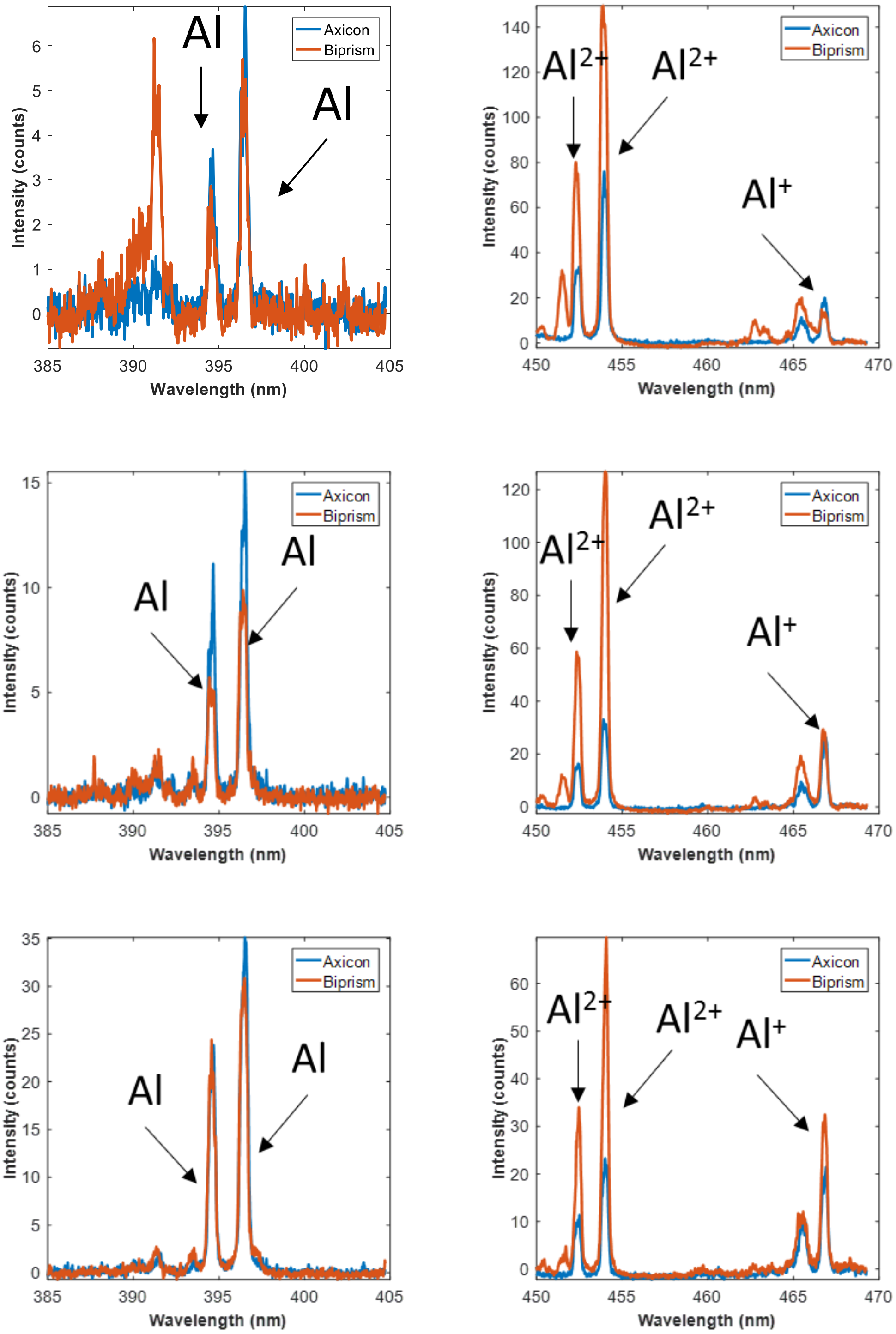

Figure 5.6: Side-on, time resolved spectra, at an ambient pressure of 1x10^{-2} mbar, for both annular and dual colliding plasmas at delays of 100 ns (top), 200 ns (middle) and 300 ns (bottom) at a laser pulse energy of 52mJ The spectrometer was centred at 394 nm (left) and 460 nm (right).

As expected, the doubly ionized lines diminish in intensity as time proceeds and that particular ion fraction declines due to recombination processes within the stagnation layers themselves and also at the layer-air interface. This trend clearly aids the growth in intensity of the Al^+ line at 466 nm with time, relative to the Al^{2+} lines, which is evident from Figure 5.6.

In the corresponding lower pressure case (10^{-5} mbar) shown in Figure 5.7 neutral line emission is weak for both dual and annular colliding plasma spectra. Similar to Figure 5.6, the Al line intensities increase with time delay. On the other hand, and in contrast to Figure 5.6, the annular colliding plasma system consistently yields the brighter line emission, and grows more quickly with time delay than the dual colliding plasma spectra. The doubly ionized lines are extremely intense in vacuo and not unexpectedly decrease very rapidly from peak values of ca. 1500 counts at 100 ns to <50 counts at 300 ns for the annular colliding plasma system. Another difference is that while the Al^{2+} lines in the dual colliding plasma spectra are consistently higher by between a factor of 2 and 10 compared to those in Figure 5.6 (10^{-2} mbar), at short time delays (<200 ns) and at 10^{-5} mbar the axicon assisted plasma lines are more intense (Figure 5.7). At longer time delays, e.g., 300 ns, the situation is reversed and mimics the spectrum shown in Figure 5.6 at 300 ns. Comparing Al^{2+} lines from dual colliding plasmas at both pressures, it can be seen that these are remarkably similar and it is the emission from the annular colliding plasma system that appears to be anomalous (as one sees in the time integrated case). It is also clear from Figure 5.7 (10^{-5} mbar) that the Al^{2+} lines are strongly broadened, indicating a high electron density. We will return to this point in the next section on plasma diagnostic data obtained using these spectra.

The 466 Al^+ emission line intensity from the annular and dual colliding plasma spectra is similar at 10^{-2} mbar. However, at 10^{-5} mbar they are quite different, by up to an order of magnitude at 200 ns, with the brightest emission coming from the annular colliding plasma system.

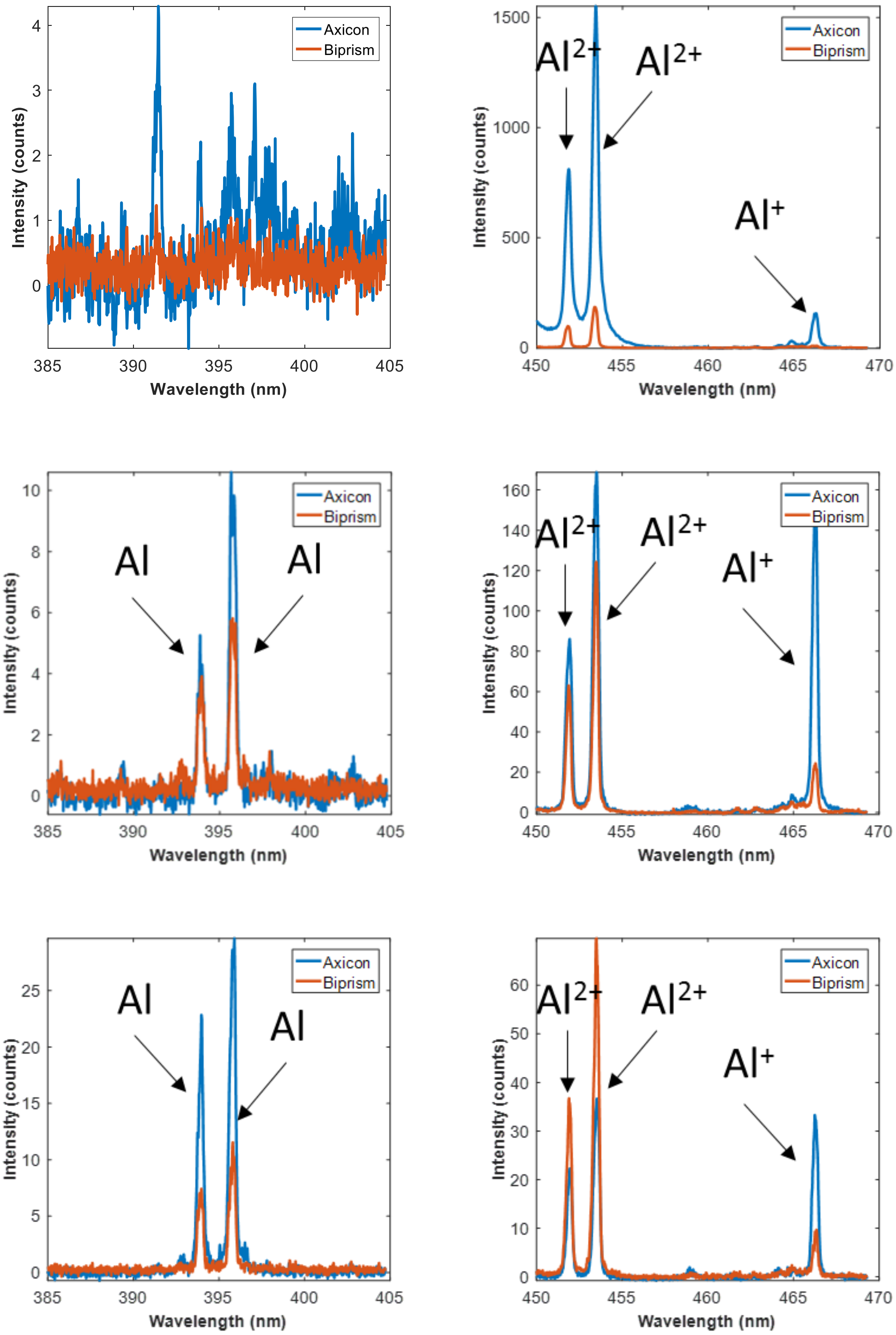

Figure 5.7: Side-on, time resolved spectra, at an ambient pressure of 1x10^{-5} mbar, for both annular and dual colliding plasmas at delays of 100 ns (top), 200 ns (middle) and 300 ns (bottom) at a laser energy of 52mJ. The spectrometer was centred at 394 nm (left) and 460 nm (right).

The reason is not immediately clear but it is worth noting the intensity ratio of the Al^{2+}/Al^{+} lines drops form more than an order of magnitude to close to unity at 200 ns, indicating a high electron-ion recombination rate for Al^{2+} perhaps leading to a much increased Al^{+} relative intensity.

For head-on viewing and at a pressure of 10^{-2} mbar (Figure 5.8) the annular colliding plasma spectra are stronger than the dual colliding spectra for the Al doublet except at a time delay of 300 ns where the line intensities become comparable. However, the atomic Al lines are weak in terms of absolute counts at both pressures, i.e., 10^{-2} mbar (Figure 5.8) and 10^{-5} mbar (Figure 5.9). There is no clear intensity trend with time delay evident from Figure 5.9 for the Al doublet as the source of the more intense lines fluctuates from colliding point plasmas to the annular colliding plasma case and back to the colliding point plasmas. The spectra are the result of averaging fifty single shot spectra and the statistical fluctuation on each peak is expected to be less than 10%. Hence these trends are not the result of large intensity fluctuations. Once again the starkest difference in intensities occurs for the doubly charged Al ion spectra where there is more than an order of magnitude difference between the annular and dual colliding plasma spectra for both pressures at a time delay of 100 ns. This is especially true at 10^{-2} mbar where the ratio of annular to dual colliding Al^{2+} line intensities is greater than 10 at all-time delays. At 10^{-5} mbar the ratio drops from over 10 to a factor of 2 at 300 ns. At 100 ns the Al^{2+} emission lines are significantly broadened indicating a high electron density and also temperature. Although broadening is clear for the comparable side-on case at 10^{-5} mbar (Figure 5.7, top right hand panel), it is much less at 10^{-2} mbar (Figure 5.8). This once again points to the need to be cautious when dealing with space integrated spectra, especially where the opacity varies from very high at the target surface to near zero far away. In such cases, where opacity varies along the direction of spatial integration, such strong broadening of the resulting spectra has been observed previously [24].

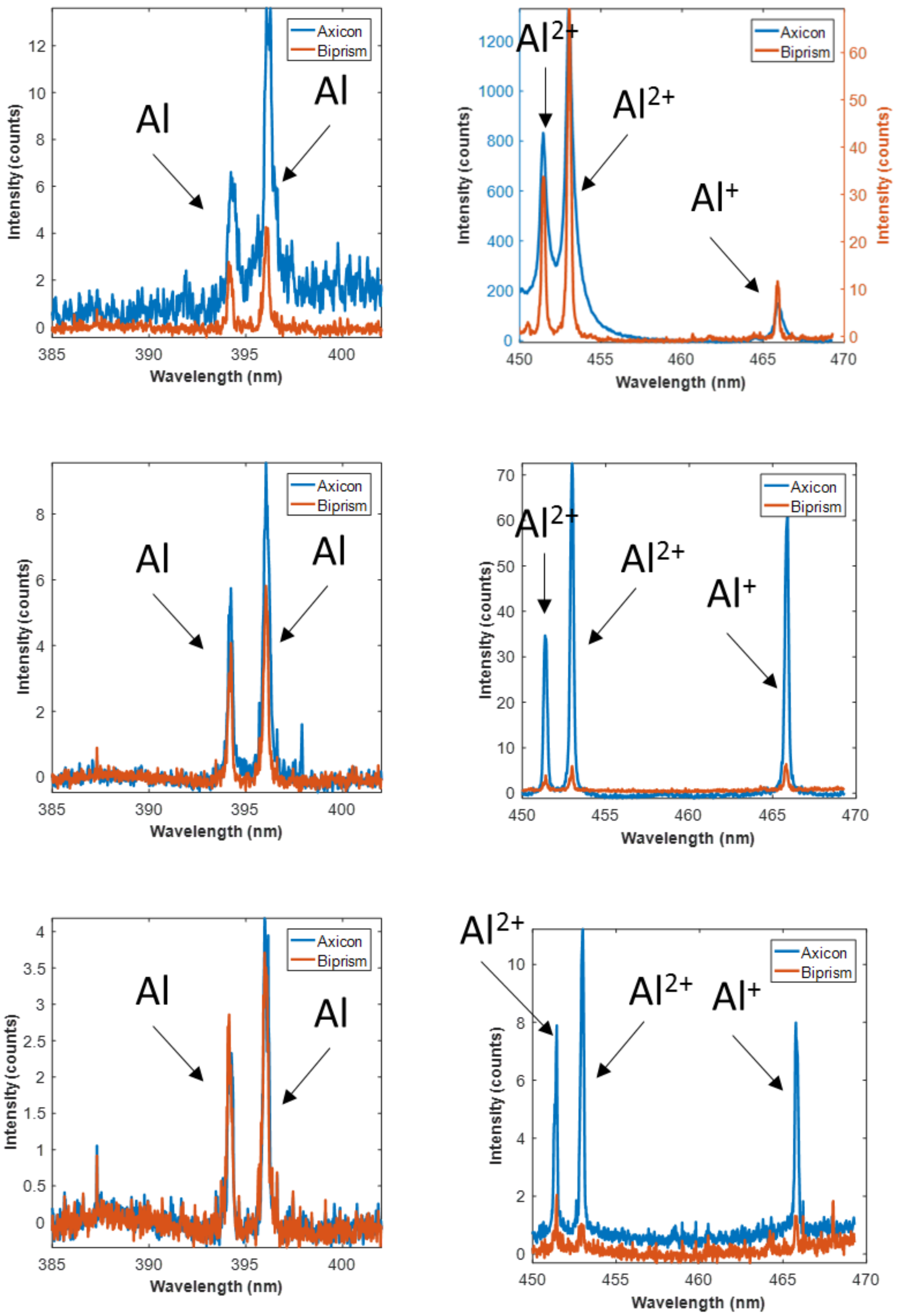

Figure 5.8: Head-on, time resolved spectra, at an ambient pressure of 1x10^{-2} mbar, for both annular and dual colliding plasmas at delays of 100 ns (top), 200 ns (middle) and 300 ns (bottom) at a laser pulse energy of 52mJ. The spectrometer was centred at 394 nm (left) and 460 nm (right).

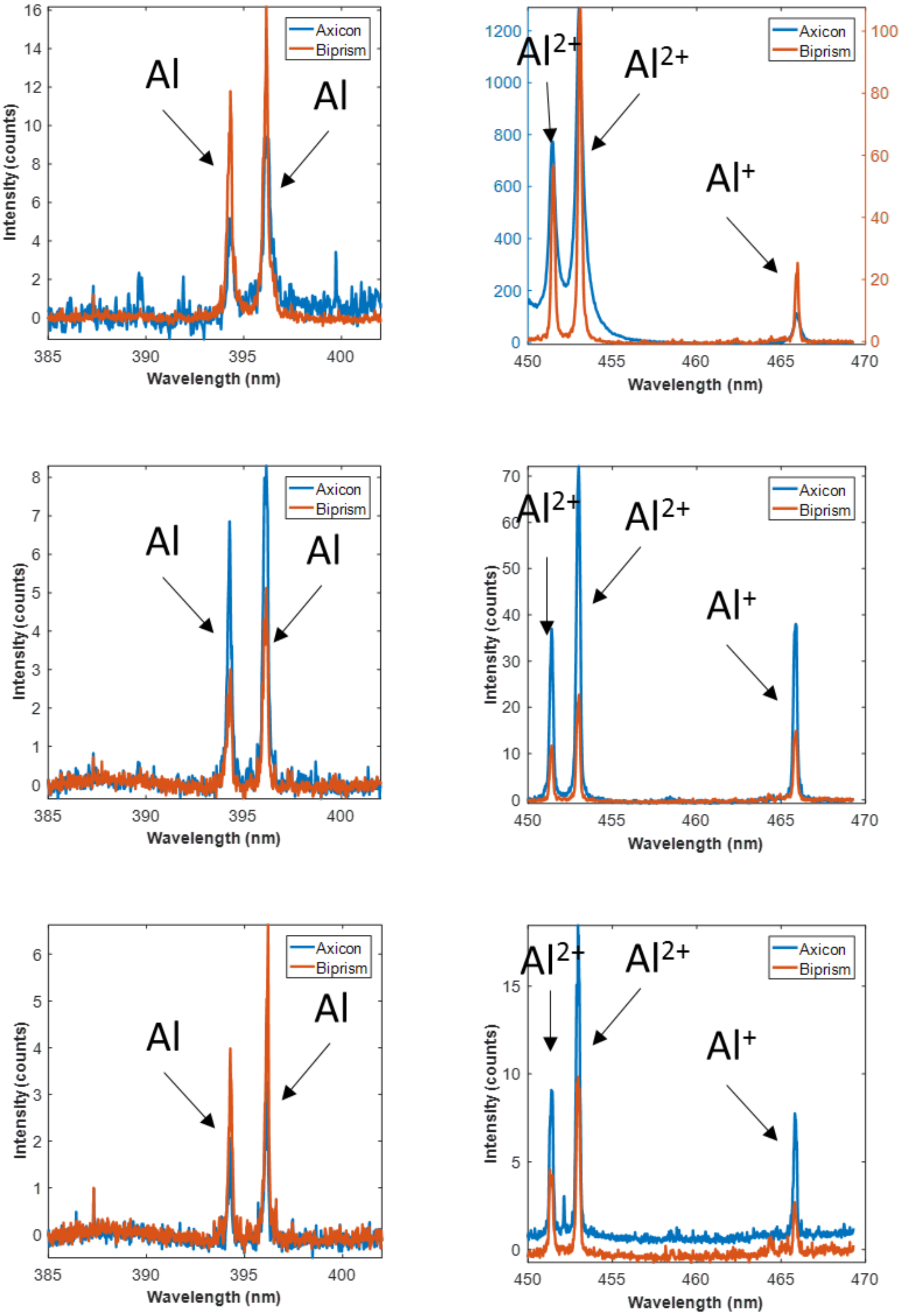

Figure 5.9 Head-on, time resolved spectra, at an ambient pressure of 1x10^{-5} mbar, for both annular and dual colliding plasmas at delays of 100 ns (top), 200 ns (middle) and 300 ns (bottom) at a laser energy of 52mJ. The spectrometer was centred at 394 nm (left) and 460 nm (right).

Turning now to the 466 nm Al^+ line, the axicon assisted plasma emission is by far the strongest at all-time delays and for both pressures. In addition, the ratio of Al^+ line intensities for annular to dual colliding plasmas is greater than 10 time delays of 200 ns and 300 ns for 10^{-2} mbar, whereas at 10^{-5} mbar the ratio is closer to 3 at these time delays.

5.2 Time Resolved Plasma Diagnostics

5.2.1 Time Resolved Density Measurements

As outlined in section 3.4.2 the electron density was extracted from the Stark broadened width of the 466.3 nm aluminium neutral line. Densities were obtained from space integrated time resolved spectra obtained at time delays in the range of 50 – 200 ns. For time delays shorter than 50 ns the spectra were dominated by continuum emission while for time delays above 200 ns, the line broadening could not be extracted reliably as they approached the instrumental broadening limit. Data are shown for plasmas formed with three different total laser pulse energies, namely 28 mJ, 38mJ and 52 mJ and at two background air pressures, namely 10^{-2} mbar and 10^{-5} mbar. The results are presented in Figure 5.10 to Figure 5.13. Each Figure contains two plots, the upper plot corresponding to an ambient air pressure of 10^{-2} mbar and the lower plot to 10^{-5} mbar.

Figure 5.10 and Figure 5.11 show the results for annular colliding plasmas viewed side-on and head-on respectively while Figure 5.12 and Figure 5.13 show the corresponding plots for the dual colliding plasmas experiments. The error bars in all density measurements reflect the error estimate range of ±10% to ±15%. The top panel in each case corresponds to the higher background air pressure, namely $1x10^{-2}$ mbar while the bottom panel show results from measurements made at the lower air pressure, i.e., $1x10^{-5}$ mbar. As for the previous section, the area of interest over which the spectra are space integrated corresponds to the locations of the stagnation layers formed in the collisions.

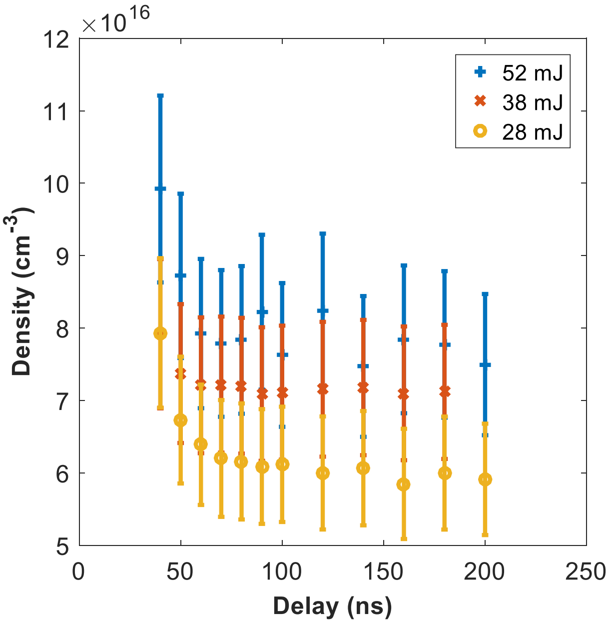

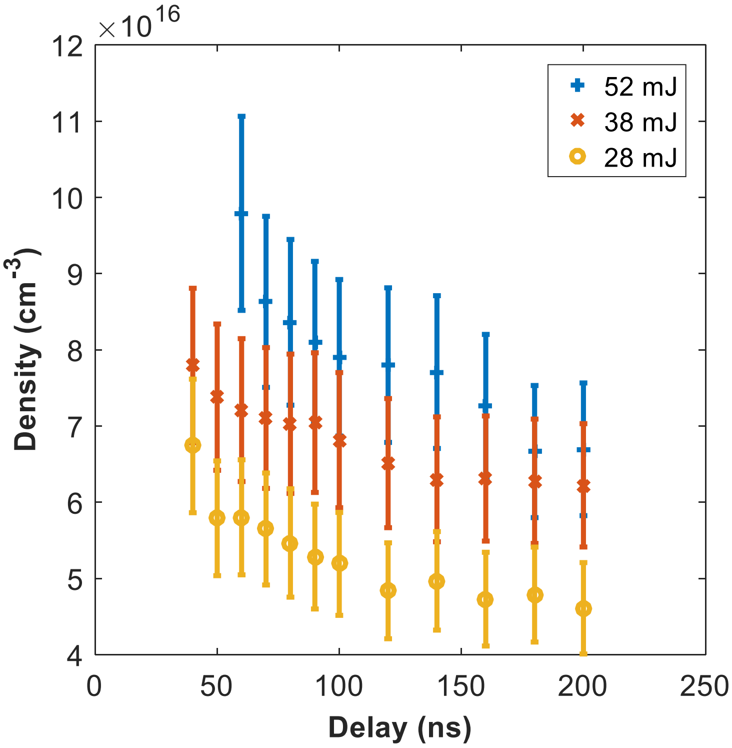

Figure 5.10: Time resolved electron density plots for an annular colliding plasma at ambient pressures of 1x10^{-2} mbar (top) and 1x10^{-5} mbar (bottom) for laser energies of 52 mJ, 38 mJ and 28 mJ. The spectra used were obtained at a side-on viewing angle.

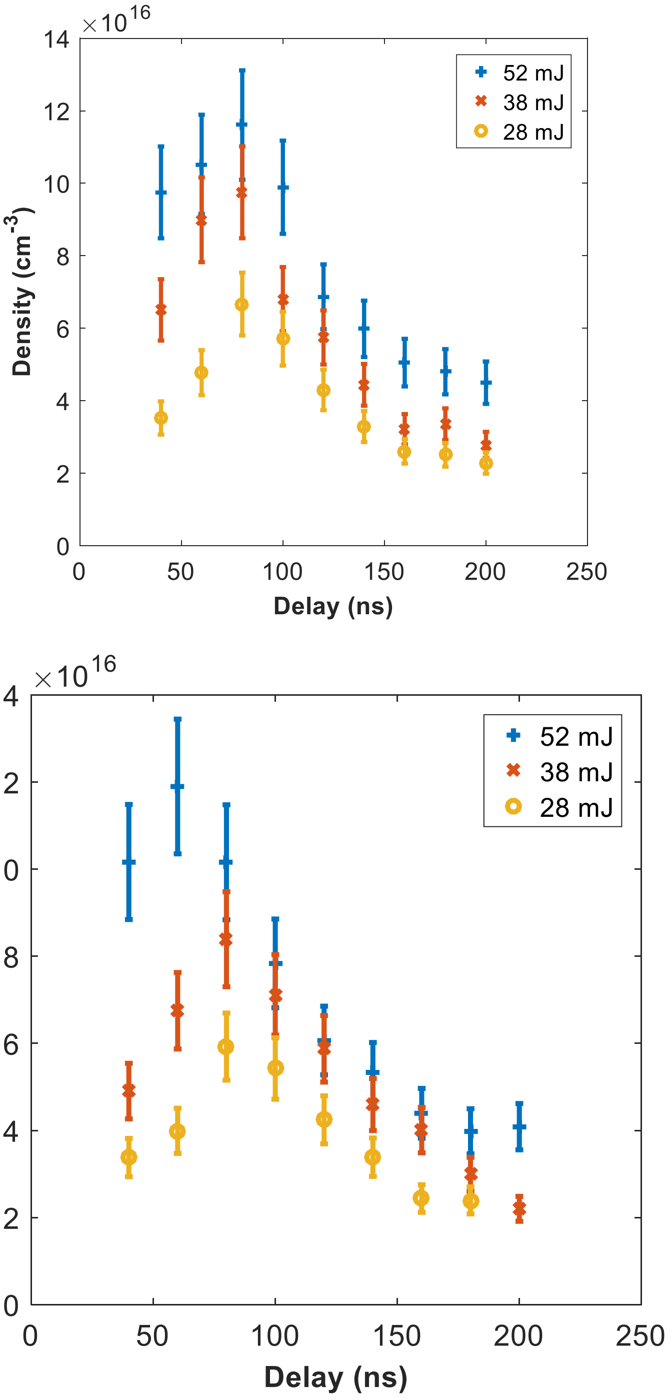

Figure 5.11: Time resolved electron density plots for an annular colliding plasma at ambient pressures of 1x10^{-2} mbar (top) and 1x10^{-5} mbar (bottom) for laser energies of 52 mJ, 38 mJ and 28 mJ. The spectra used were obtained at a head-on viewing angle.

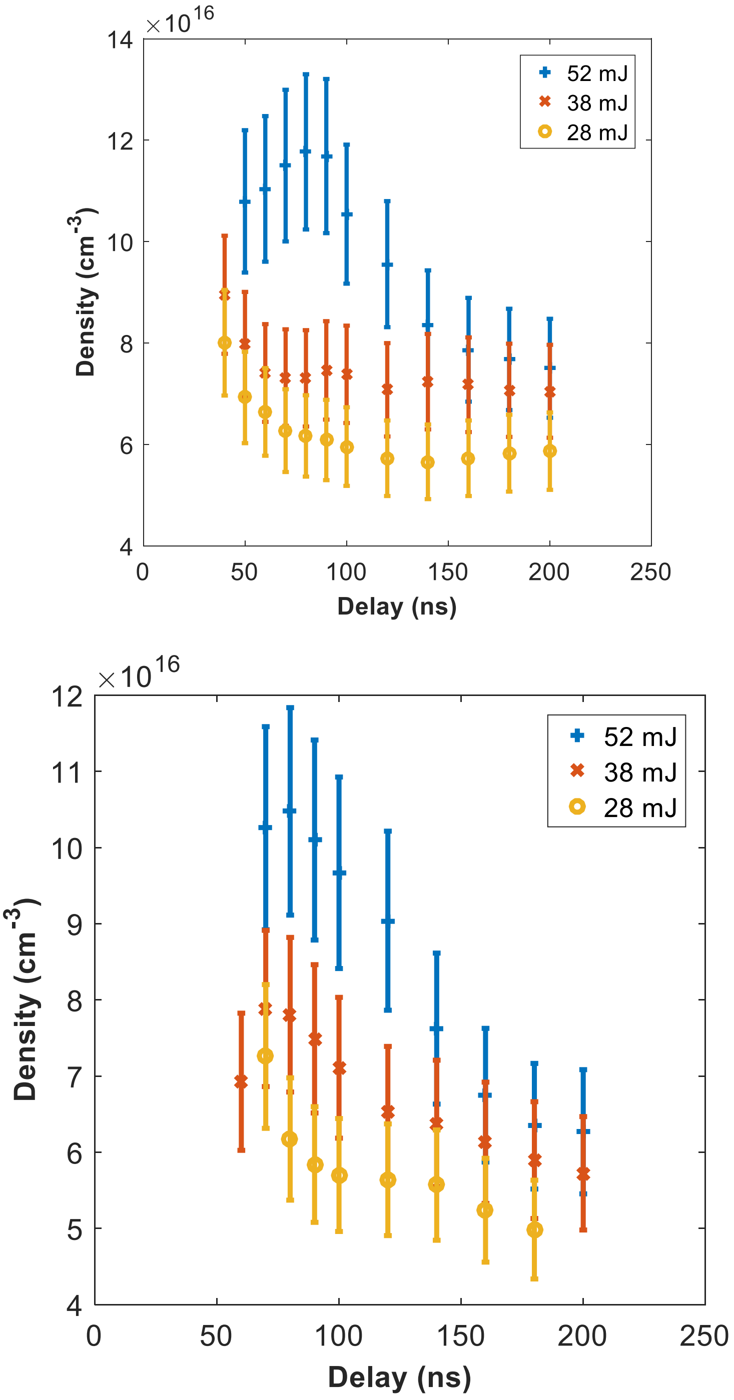

Figure 5.12: Time resolved electron density plots for dual colliding plasmas at ambient pressures of 1x10^{-2} mbar (top) and 1x10^{-5} mbar (bottom) for laser energies of 52 mJ, 38 mJ and 28 mJ. The spectra used were obtained at a side-on viewing angle.

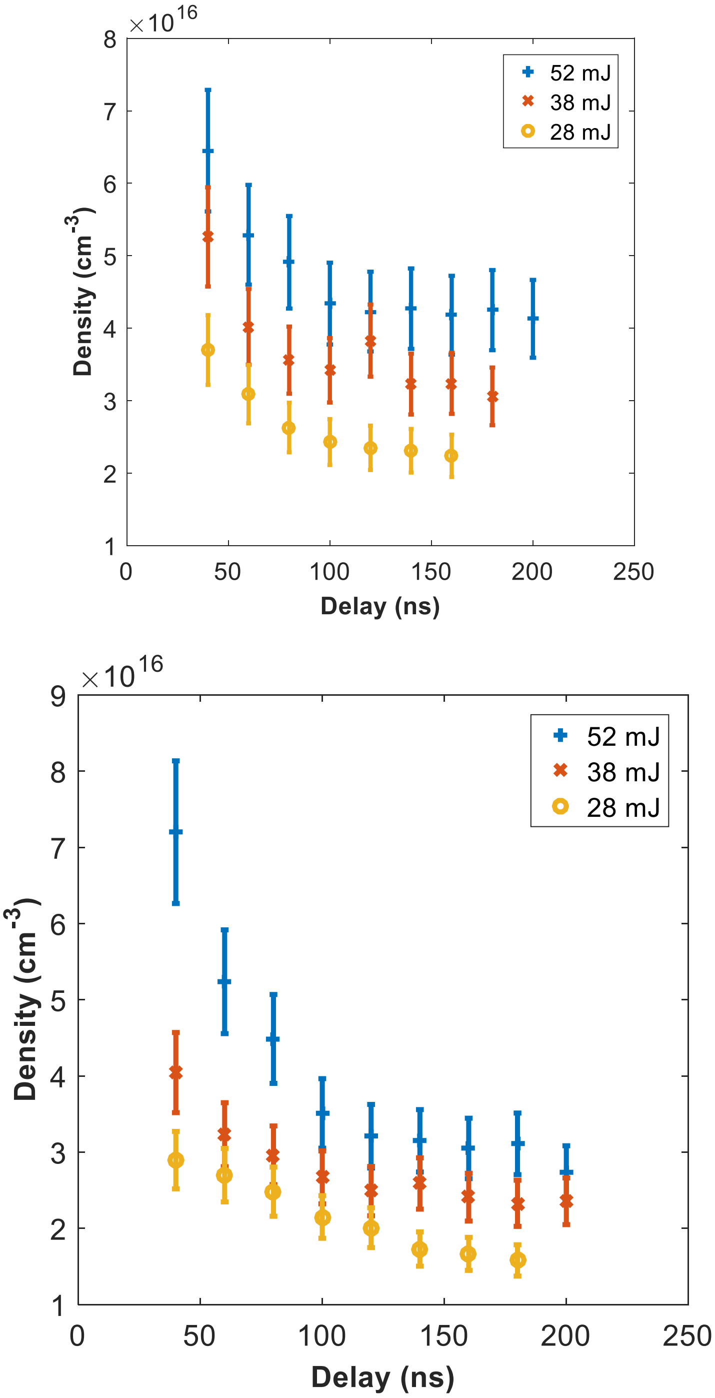

Figure 5.13: Time resolved electron density plots for dual colliding plasmas at ambient pressures of 1x10^{-2} mbar (top) and 1x10^{-5} mbar (bottom) for laser energies of 52 mJ, 38 mJ and 28 mJ. The spectra used were obtained at a head-on viewing angle.

The error on the widths obtained by fitting a Voigt profile to each spectrum line has been folded into the densities extracted from these widths and shown as an error bar on each data point on the plots (Figure 5.10 to Figure 5.13). These typically in the range of ±10% to ±20% as can be seen from these figures.

Looking at all four figures it is clear that the electron density scales with laser pulse energy. This is to be expected as a higher pulse energy results in a higher on target irradiance, temperature and average ionization stage for the seed plasmas which will convert into higher values of these parameters for the stagnation layers formed. Overall the highest densities are observed for the shortest time delays.

For the side-on views the density tends to peak near 50 ns and drop off gradually with time delay. On the other hand for the spectra obtained via the head-on view, the density increases with time delay, peaking at ca. 80 ns and then gradually falling off with time delay. This is consistent with the occurrence of stagnation which tends to become evident in the time resolved imaging at ca. 40 ns and is well established by 80 ns, see for example figure 4.19 and 4.20 for annular plasmas.

In addition the densities from spectra obtained in the head-on view are consistently higher by about 20% compared to the values obtained in side-on viewing mode. This is consistent with the rather broad spectra observed in the previous section, especially for annular colliding plasmas, albeit that was more obvious in the ion emission lines which are clearly more sensitive to electron density. There is also some evidence that in general stagnation layers formed at the higher ambient air pressure (i.e., 10^{-2} mbar) exhibit slightly higher electron densities, especially at delays in excess of 100 ns, by which time gated imaging shows stagnation layers to have been well established.

In summary the electron density in all stagnation layers peaks at values in the 10^{17} cm^{-3} range with the highest values obtained in head-on viewing mode. It also appears that stagnation layers formed in the higher background pressure of 10^{-2} mbar display slightly higher electron densities than for the 10^{-5} mbar cases for time delays, especially at the longer time delays.

Knowing now the electron density at the stagnation region and relative expansion velocities of the seed plasmas (dual colliding point plasmas or the annular plasma) it is possible to use equations 15 and 16 to compute the collisionality parameter ξ. It is worth restating the equations here for ease of reading, namely:

$$\xi = \frac{D}{\lambda_{ii}} \qquad \text{Equation 61}$$

where ξ is the collisionality parameter, D is the distance between the two seed plasmas and

$$\lambda_{ii}(1-2) = \frac{4\pi\epsilon_0 {m_i}^2 {v_{12}}^4}{e^4 Z^4 n_i \ln(\Lambda_{12})} \qquad \text{Equation 62}$$

An average charge of 1+ is assumed. The measured electron density averages around 10^{17} cm^{-3} for both colliding plasma systems and is used in equation 16 for the ion density. The Coulomb logarithm is typically 5 for table top laser produced plasmas [25] and we take the experimental *D* = 2mm. We will take as examples two relative seed velocities, 3 x 10^4 m.sec^{-1} and 1 x 10^5 m.sec^{-1}. For copper ions the results are as follows.

v_{12} = 3 x 10^4 m.sec^{-1}, $\lambda_{ii}(1-2)$ = 2.7 x 10^{-5} m, $\xi = 74$

v_{12} = 1 x 10^5 m.sec^{-1}, $\lambda_{ii}(1-2)$= 3.3 x 10^{-3} m, $\xi = 0.6$

The results show the quartic dependence of the collisionality parameter very nicely. Since seed plasmas typically expand at low 10^4 m.sec^{-1}, and stagnation occurs for values of ξ > 1, one can expect strong stagnation in the case of the system studied here, which is indeed observed.

5.2.2 Time Resolved Temperature Measurements

As outlined in the experimental setup chapter the electron temperature was extracted from the ratio of the 451.38 nm doubly ionised aluminium line to the 466.43 nm singly ionised aluminium line. The results are presented in the same sequence as for the electron densities in section 5.2.1 above. As expected the highest temperatures are obtained for stagnation layers formed with the highest laser pulse energy and the temperature scales with laser pulse energy at all-time delays. Temperatures tend to peak at delays shorter than 80 ns. However, the large error bars make it difficult to confirm that in Figure 5.15, Figure 5.16 and Figure 5.17 where the temperature appears to grow with time delay initially before falling away thereafter. The error bars in all temperature measurements reflect the error estimate range of ±10% to ±15%.

The temperature does not vary much with time delay. It at values close to 1.1 eV and ends on values close to 1 eV (at a time delay of 200 ns). Similar drops of 0.1 eV are observed for the other laser pulse energies of 38 mJ and 28 mJ so that the stagnation layer temperatures vary only slowly with time delay. This is in contrast to what is normally observed for single point plasma plumes where temperature tends to drop quite quickly with time delay as the plume expands adiabatically [26]. It is also one of the positive features of stagnation layers, namely that temperature is not just quite uniform spatially [27] but also temporally [28]. This is important for potential applications, e.g., as a pre-heated target for an EUV Lithography (EUVL) light source [29], for use in laser-analytical methods such as double pulse LIBS [30] or potentially as source for thin film materials growth [31].

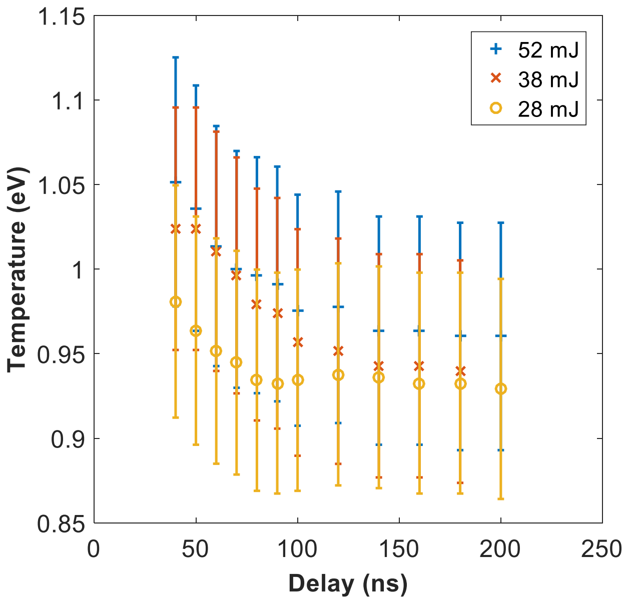

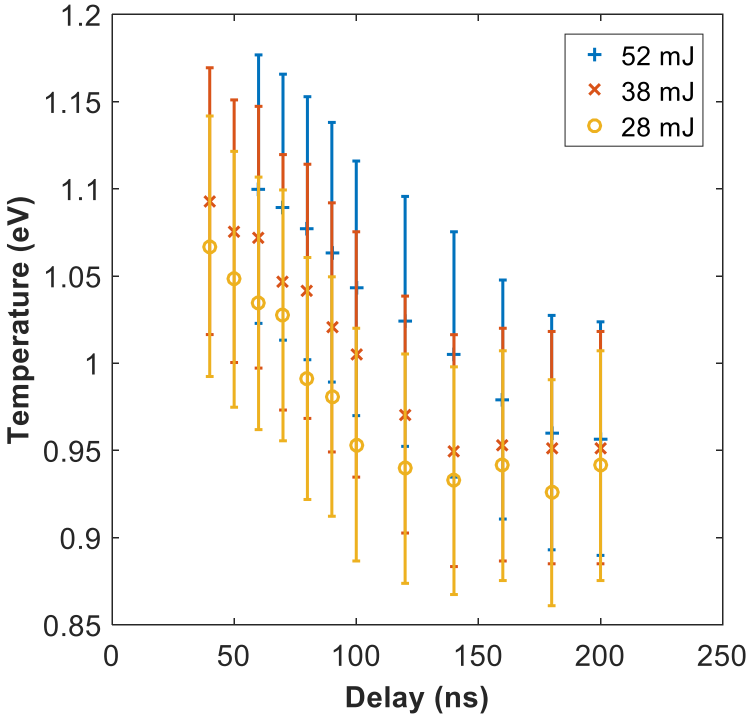

Figure 5.14 Time resolved temperature plots for an annular colliding plasma at ambient pressures of $1x10^{-2}$ mbar (top) and $1x10^{-5}$ mbar (bottom) at laser energies of 52 mJ, 38 mJ and 28 mJ. The spectra used were obtained at a side-on viewing angle.

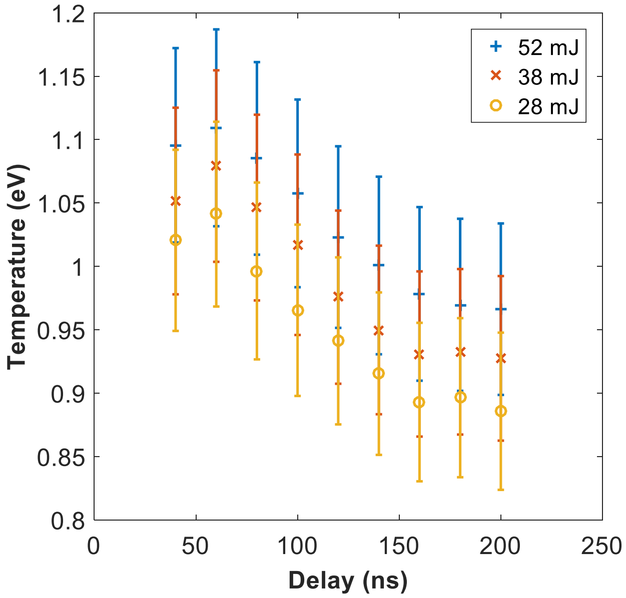

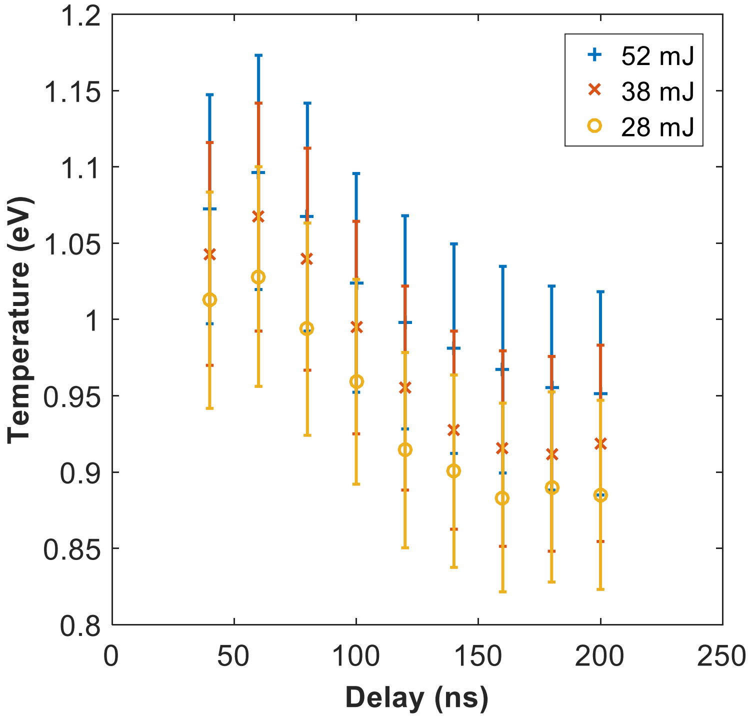

Figure 5.15 Time resolved temperature plots for an annular colliding plasma at ambient pressures of 1x10^{-2} mbar (top) and 1x10^{-5} mbar (bottom) at laser energies of 52 mJ, 38 mJ and 28 mJ. The spectra used were obtained at a head-on viewing angle.

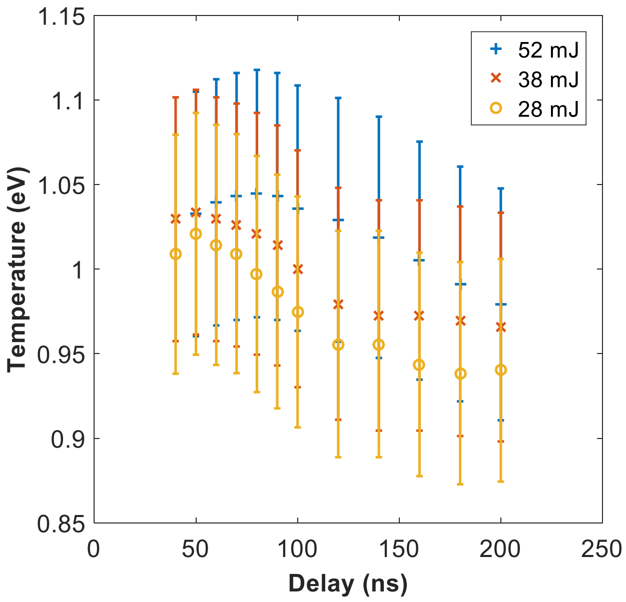

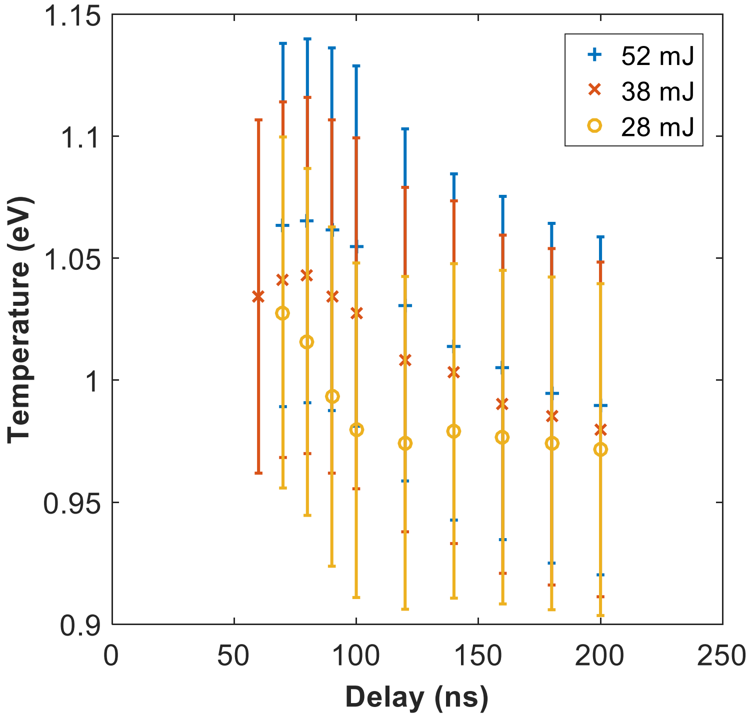

Figure 5.16: Time resolved temperature plots for dual colliding plasmas at ambient pressures of 1x10^{-2} mbar (top) and 1x10^{-5} mbar (bottom) at laser energies of 52 mJ, 38 mJ and 28 mJ. The spectra used were obtained at a side-on viewing angle.

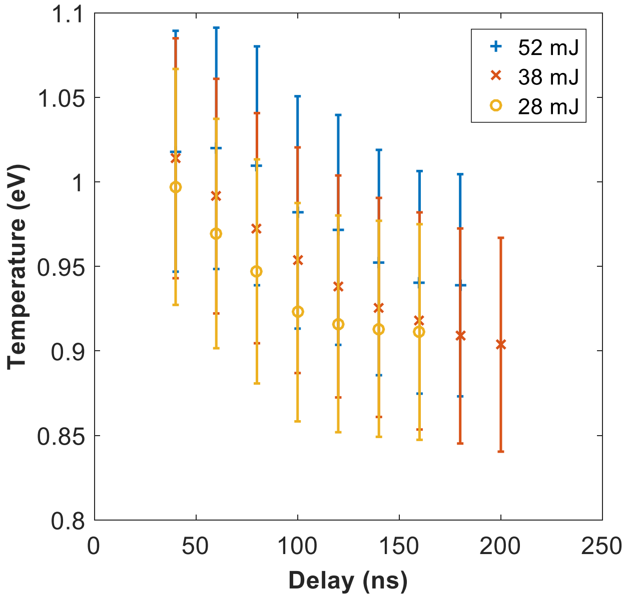

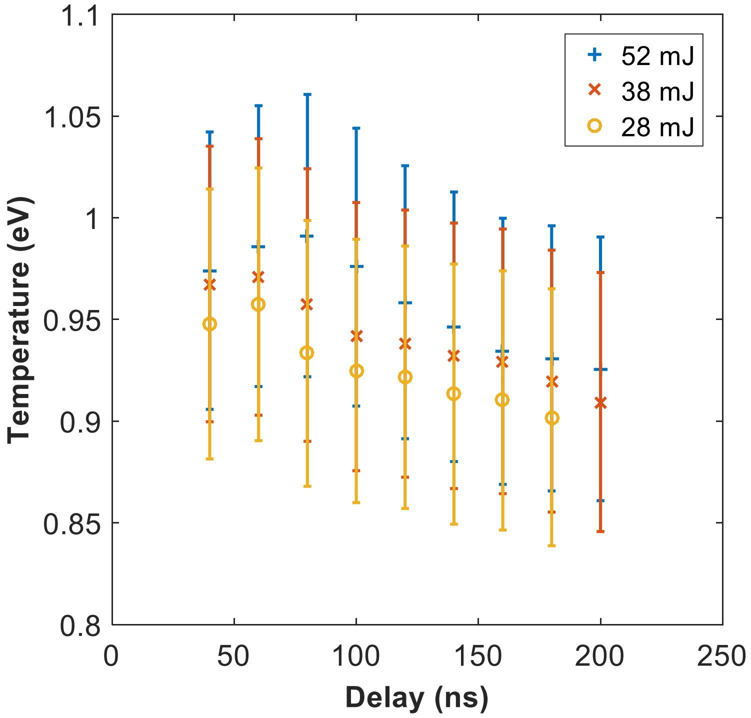

Figure 5.17: Time resolved temperature plots for dual colliding plasmas at ambient pressures of 1x10^{-2} mbar (top) and 1x10^{-5} mbar (bottom) at laser energies of 52 mJ, 38 mJ and 28 mJ. The spectra used were obtained at a head-on viewing angle.

So the stagnation layer temperatures do not vary much with time or between layers formed in annular colliding plasma versus dual colliding plasma systems. Temperature does depend on the initial seed plasma conditions, as determined by the laser pulse energy.

5.3 Summary

Space integrated and time integrated, along with space integrated and time resolved spectra have been presented for stagnation layers formed at the collision front between two side by side plasmas and also an annular or ring plasma. Plasmas were formed at two background air pressures, namely 1x10^{-2} mbar and 1x10^{-5} mbar. Spectra were recorded both along and orthogonal to the plasma (stagnation layer) expansion axis. Results were presented for a range of low laser pulse energies extending from 28 mJ to 52 mJ. In general spectral behaviour with laser pulse energy and/or time delay was as expected. However, some trends are still not fully understood, especially very high intensities which can depend on viewing geometry, the ambient environment or the focusing geometry. It is likely these are due to spatial variations in electron density and temperature evidenced by the broad line widths in the most anomalously intense emission lines. Such anomalies have been observed before in space resolved spectra where strong broadening and line reversal occur close to the target surface and result in line shapes that are quite distorted when such spectra are space resolved. In future work, it would be important to record and analyse space-time resolved spectra for stagnation layers formed with the aid of biprism and axicon optical elements.

Bibliography

[1] D. E. Kelleher and L. I. Podobedova, “Atomic Transition Probabilities of Aluminum. A Critical Compilation,” *J. Phys. Chem. Ref. Data,* Vol. 37, no. 2, pp. 709–911, 2008.

[2] https://physics.nist.gov/PhysRefData/ASD/lines_form.html

[3] P. Sankar, H. D. Shashikala and R Philip, "Ion dynamics of a laser produced aluminium plasma at different ambient pressures", *Appl. Phys. A*, Vol. 124, Art. No. 26, 2018.

[4] N. Walsh, J. T. Costello and T. J .Kelly, "Optical diagnostics of laser-produced aluminium plasmas under water", *Appl. Phys. B*. Vol. 123, Art. No. 179 2017.

[5] G A Wubetu, H Fiedorowicz, J T Costello and T J Kelly, "Time resolved anisotropic emission from aluminium laser produced plasma", *Physics of Plasmas* Vol. 24, Art. No. 013105, 2017.

[6] D. M. Surmick and C. G.Parigger, "Electron density determination of aluminium laser-induced plasma", *J. Phys. B: At. Mol. Opt. Phys.* Vol. 48 Art. No. 115701 2015.

[7] P.Yeates, "Biberman 'free-bound' continuum correction factor approximation for line-to-continuum temperature diagnostic of aluminium laser plasma", *J. Phys. B: At. Mol. Opt. Phys. Vol. 44,* Art. No. 075002 2011.

[8] C. Goueguel, S. Laville, F. Vidal, F, M. Sabsabi, M and M. Chaker, "Investigation of resonance-enhanced laser-induced breakdown spectroscopy for analysis of aluminium alloys", *J. Anal. At. Spec.*, Vol. 25, pp. 635-644, 2010.

[9] M. Ribiere, D. Karabourniotis and B. G. Cheron, "Spectroscopic analysis of the excitation transfer from background air to diffusing aluminum laser produced plasma", *J. Appl. Phys.*, Vol 105, Art. No. 083309, 2009.

[10] R. Ramos, G. Cunge, G, M. Touzeau, and N. Sadeghi, "Measured velocity distribution of sputtered Al atoms perpendicular and parallel to the target", *J. Phys. D: Appl. Phys. Vol. 41*, Art. No. 152003 2008.

[11] O. A. Bukin, E. A. Sviridenkov, N. V. Sushilov, NV, A. Y. Maior and O. I. Kholodkevich, "Detection of anomalous self-reversal of emission lines of a laser plasma formed on the surface of a solid target in a normal atmosphere", *Quant. Electron.*, Vol. 27, pp. 706-707, 1997.

[12] G. O'Connell, I. Tobin, I and J. G. Lunney, "Early stage optical emission in nanosecond laser ablation", *Appl. Phys. A,* Vol 110, pp. 731-734, 2013.

[13] A. Sarkar and M. Singh, "Laser-induced plasma electron number density: Stark broadening method versus the Saha-Boltzmann equation", *Plasma Sci. & Technol.*, Vol. 19, Art. No. UNSP 025403, 2017.

[14] M. Burger and J. Hermann, "Stark broadening measurements in plasmas produced by laser ablation of hydrogen containing compounds", *Spectrochimica Acta Part B*, Vol. 122, pp. 118-126, 2016.

[15] J. Bengoechea, J. A. Aguilera and C. Aragon, "Application of laser-induced plasma spectroscopy to the measurement of Stark broadening parameters", *Spectrochimica Acta Part B*, Vol. 61, pp. 69-80, 2006.

[16] N. Farid, S. S. Harilal, H. Ding, and A. Hassanein, "Emission features and expansion dynamics of nanosecond laser ablation plumes at different ambient pressures", *J. Appl. Phys.*, Vol. 115, Art. No. 033107, 2014.

[17] R. S. Marjoribanks, F. W. Budnik, H.Chen and D. D. Meyerhofer, "Electron temperature in transient plasmas from quasi-steady ratio of isoelectronic lines: Application to picosecond and subpicosecond plasmas", *J. Opt. Soc. Am. B*, Vol. 13, pp 380-387, 1996.

[18] R. S. Marjoribanks, M. C. Richardson, P. A. Jaanimagi and R. Epstein, "Electron-temperature measurement in laser-produced

plasmas by the ratio of isoelectronic line-intensities", *Phys. Rev. A*, Vol. 46, pp. R1747-R1750, 1992.

[19] Integral cross section measurements and product recoil velocity distributions of Xe^{2+} + N_2 hyperthermal charge-transfer collisions, M. L. Hause, B. D. Prince and R. J. Bemish, *J. Chem. Phys.*, Vol. 145, Art. No. 044309, 2016.

[20] S. Werbowy and B. Pranszke, "Charge-exchange processes in collisions of H^+, H^{+2} , H^{+3} , He^+, and He^{+2} ions with CO and CO_2 molecules at energies below 1000 eV", *Phys Rev. A,* Vol 93, Art. No. 022713, 2016.

[21] D. Colombant and G.F. Tonon, "X-ray emission in laser-produced plasmas", *J. Appl. Phys.*, Vol. 44, pp. 3524–3537, 1973.

[22] C. Fallon, P. Hayden, N. Walsh, E. T. Kennedy, and J. T. Costello, "The Effect of Wedge Angle on the Evolution of a Stagnation Layer in a Colliding Plasma Experiment," *J. Phys. Conf. Ser.*, Vol. 548, no. 1, p. 12036, 2014.

[23] C. Fallon, P. Hayden, N. Walsh, E. T. Kennedy, and J. T. Costello, "Target geometrical effects on the stagnation layer formed by colliding a pair of laser produced copper plasmas," *Phys. Plasmas*, Vol. 22, no. 9, p. 93506, 2015.

[24] K. D. Kavanagh, "Image and Spectroscopy of Laser produced Colliding Plasmas," *PhD Thesis,* no. August, p. 225, 2006.

[25] P. Mulser, G. Alber and M. Murakami, "Revision of the Coulomb logarithm in the ideal plasma", *Physics of Plasmas*, Vol. 21, Art. No. 042103 (2014)

[26] D Doria, K D Kavanagh, J T Costello and H Luna, "Plasma parametrization by analysis of time-resolved laser plasma image spectra", *Meas. Sci. Technol.*, Vol. 17, pp670-674, 2006.

[27] J Dardis and J T Costello,"Stagnation layers at the collision front between two laser-induced plasmas: A study using time resolved

imaging and spectroscopy”, *Spectrochimica Acta Part B*, Vol. 65, pp627-635, 2010.

[28] H Luna, K D Kavanagh and J T Costello, “Study of a colliding laser-produced plasma by analysis of time- and space-resolved image spectra”, *J. Appl. Phys.*, Vol. 101, Art. No. 033302, 2007.

[29] T. Cummins, C. O'Gorman, P. Dunne, E. Sokell, G. O'Sullivan, and P. Hayden, "Colliding laser produced plasmas as targets for laser-generated extreme ultraviolet sources", *Appl. Phys. Lett.*, Vol. 105, Art. No. 044101, 2014.

[30] C. Sánchez-Aké, Marduk Bolaños and C.Z. Ramírez, "Emission enhancement using two orthogonal targets in double pulse laser-induced breakdown spectroscopy", *Spectrochimica Acta Part B*, Vol. 64, pp. 857–862., 2009.

[31] A. Tselev, A. Gorbunov and W. Pompe, "Cross-beam pulsed laser deposition: General characteristic", *Rev. Sci. Instrum.*, Vol. 72, pp2665-2672, 2001.

6. Focusing Geometrical Effects on the Limit of Detection of Laser Induced Breakdown Spectroscopy

LIBS or laser induced breakdown spectroscopy for elemental detection, classification and quantification [1–3] and is one potential application of colliding plasma systems and stagnation layers [4–6]. In LIBS characteristic emission lines act as the fingerprints of elements in the sample being irradiated with an intense laser. The critical figure of merit is the limit-of-detection [7–9] (LOD) which is related to the line to background intensity ratio, most commonly referred to as the signal-to-background ratio [10–12] (SBR). An initial study on the effect of focusing geometry on SBR and LOD is reported in this chapter. Specifically a single point plasma, dual colliding plasmas and annular colliding plasmas are compared. The targets are aluminium with known concentrations of copper. So the matrix here is aluminium while the analyte (trace element) is copper.

6.1 Time and Space Integrated Spectroscopy

The optimal time delay between plasma formation and the opening of the gate was found using the single plasma focusing geometry and a laser energy of 52 mJ. The optimal delay was taken as the delay at which the signal to background ratio of the 466.4 nm was maximised. The delay was increased in increments of 20ns while the gate of the ICCD was maintained at 1.5 μs [13,14].

The maximum signal to background ratio for the given experimental conditions was found to be 130 ns after plasma ignition. This delay was used for all experiments within this chapter. It is well established that the early time emission from laser produced plasmas (and stagnation layers) is dominated by continuum emission [15–18].

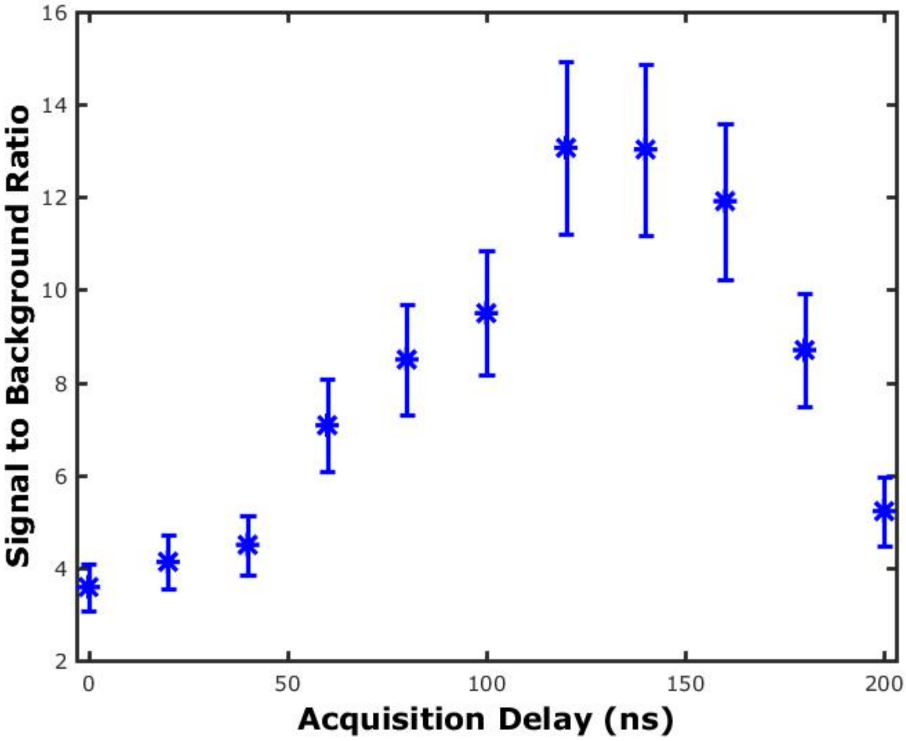

Figure 6.1: Variation in signal to background ratio for the 466.4 nm singly ionised aluminium line with increasing gate delay and a fixed gate width of 1.5µs. The experiment was performed for a single point plasma.

As can be seen in Figure 6.1, by delaying the exposure (i.e., the opening of the gate in the ICCD), one optimises the line signal over the continuum signal. The maximum signal-to-background ratio (SBR) occurred for a time delay of 130 ns in the case of the Al^+ 466.3 nm line. This line is used here as a proxy for all emission lines, especially the Cu line emission. There is also a maximum width for the gate window (exposure time) beyond which the line emission will become weak and drop back towards the background signal level, adversely affecting the SBR. This is typically 1 – 5 μs for most LIBS experiments and was found to be 1.5 μs for the 466.3 nm line. Clearly, if time permitted, it would be best to do this measurement for all emission lines of interest. This would however, constitute a major future study in itself. It should also be noted that by 130 ns the stagnation layer has been formed in the area of interest captured by the ICCD. So spectra recorded for annular colliding and dual colliding plasmas are the spectra of the corresponding stagnation layers.

6.2 Time Integrated Spectra

Time and space integrated spectroscopy was carried out on each of the four standard aluminium targets containing known concentrations of trace element impurities such as copper. This enabled the construction of calibration curves for each focusing geometry, namely annular, dual colliding and single plume plasmas. Fifty single shot acquisitions (exposures) were taken for each target using each of three focusing geometries. Annular, dual colliding and single plasma spectra are shown in Figure 6.2, Figure 6.3 and Figure 6.4 respectively for a total laser pulse energy of 28 mJ. The copper concentration values for each target were T1 (141 ppm), T2 (184 ppm), T3 (860 ppm) and T4 (2600 ppm). The delay was fixed at 130 ns as above and the ICCD gate width (exposure time) was set at 1.5 µs. Hence the spectra are effectively time integrated, while noting that the initial emission in the 0-130 ns time window has been rejected. The main transitions are listed in table 6.0 below.

*Table 6.0**:** Lines identified in the LIBS spectra*

Ion	**Lower State**	**Upper State**	**Wavelength (nm)**
Cu^+	$3d^9(^2D_{3/2})4d\ ^2[3/2]_1$ $3d^9(^2D5_{/2})4d\ ^2[1/2]_1$	$3d^8(^3P)4s4p(^3P)\ ^1P_1$ $3d^8(^3P)4s4p(^3P)\ ^3P_2$	517.74
Cu^+	$3d^9(^2D_{5/2})4d\ ^2[1/2]_0$	$3d^9(^2D_{5/2})4f\ ^2[1/2]_1$	518.48
Cu^+	$3d^8(^3F)4s4p(^3P)\ ^3F_4$	$3d^9(^2D_{5/2})5d\ ^2[5/2]_3$	519.41
O^{3+}	$2s2p(^1P)3p\ ^2S_{1/2}$	$2s2p(^3P)4s\ ^2P_{1/2}$	519.82
Cu	$3d^9(^2D)4s4p(^3P)^2F_{5/2}$	$3d^94s(^3D)5s\ ^4D_{5/2}$	520.23
Cu^{2+}	Unassigned	Unassigned	520.97
Cu	$3d^{10}4p\ ^2P_{3/2}$	$3d^{10}4d\ ^2D_{5/2}$	521.96
Cu^+	$3d^9(^2D_{3/2})4d\ ^2[3/2]_1$	$3d^8(^3F)4s4p(^1P)\ ^3D_2$	529.74

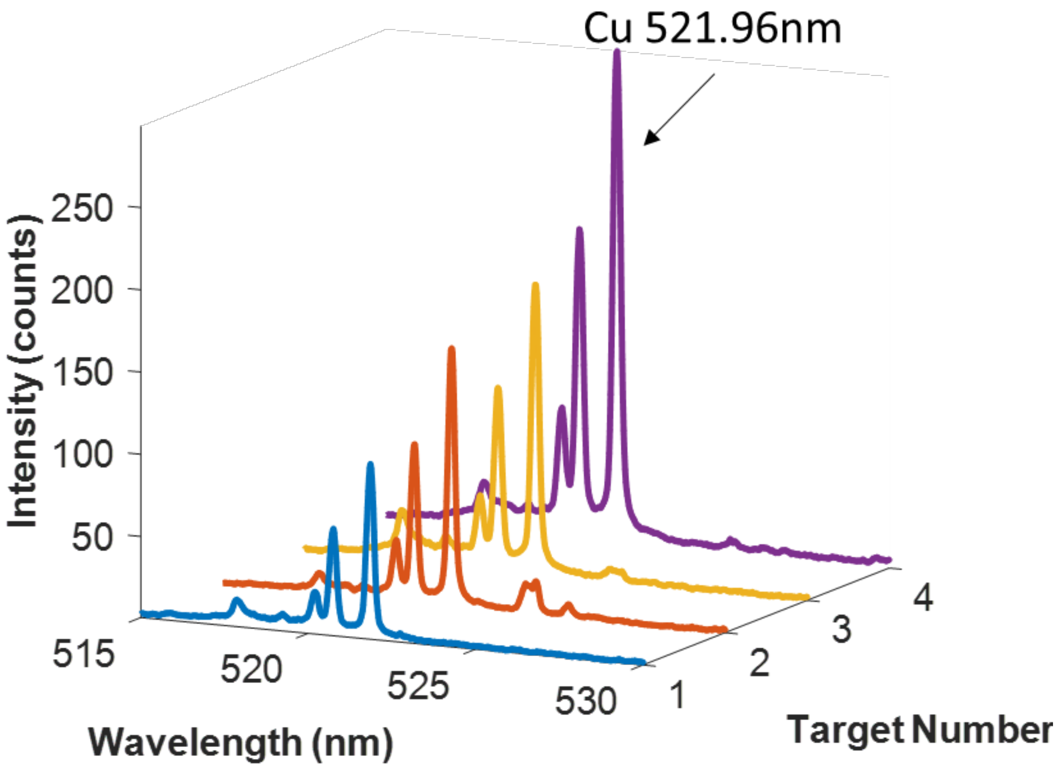

Figure 6.2:Time and space integrated spectra centred at 519 nm, for each aluminium target, captured from the stagnation layer formed at the centre of an annular plasma generated with a laser energy of 28 mJ. The Cu concentration values for T1 to T4 are 141, 184, 860 and 2600 ppm respectively.

Emission from the dual and single plasma cases is stronger in the spectral range between 517 nm and 520 nm compared to the 521.96 nm copper neutral line indicating strong ion emission for these cases. Specifically, the lines within the 517nm to 520 nm spectral window are three singly ionised copper lines, at 517.74 nm, 518.48 nm and 519.57 nm, and one neutral iron line at 519.37 nm. It is likely that these lines are more prevalent due to the higher power density onto the target in the dual and single plasma cases. It should also be noted that as the laser energy is increased in the annular plasma case, these lines become more prominent (see Figure 6.5, Figure 6.6 & Figure 6.7 in the following section) as the associated stagnation layer becomes hotter (higher plume kinetic energy converted into a hotter stagnated region), although they are accompanied by a larger continuum contribution.

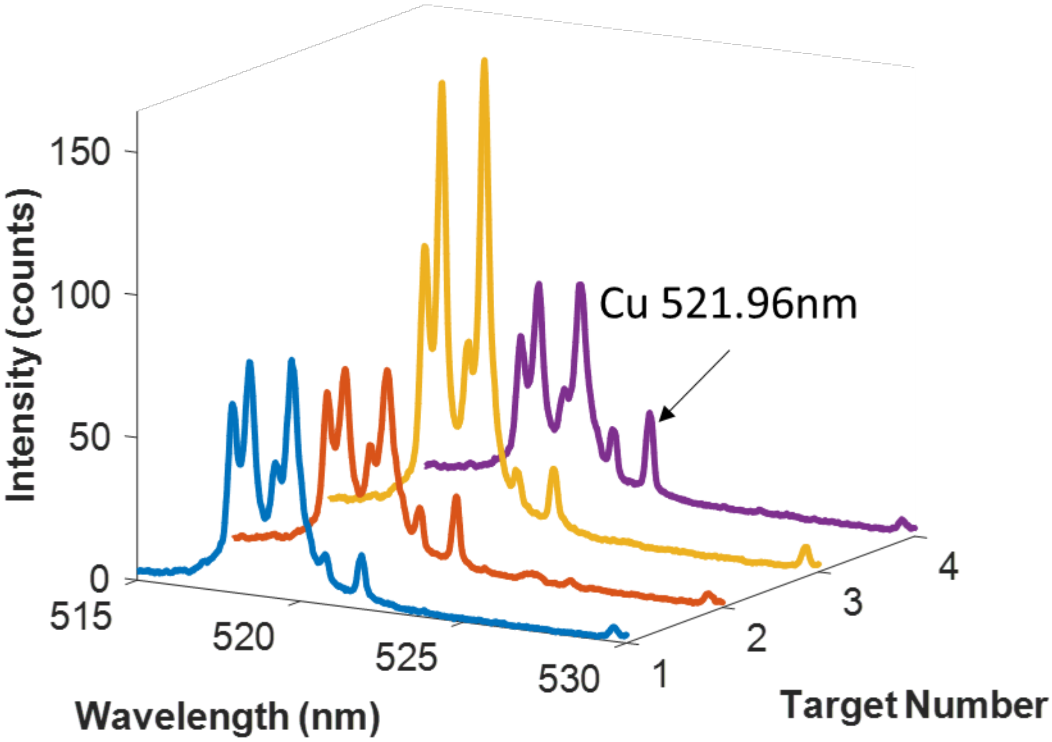

Figure 6.3: Time and space integrated spectra centred at 519 nm, for each aluminium target, captured from the stagnation layer formed between two seed plasmas generated with laser energy of 14 mJ per seed. The Cu concentration values for T1 to T4 are 141 (blue), 184 (red), 860 (orange) and 2600 (purple) ppm respectively.

It is also clear that although the spectral line intensity increases with increasing concentration from T1 to T4 in the case of the annular colliding plasma, this not the case for the other two geometries. From Figure 6.3 and Figure 6.4 it seems clear that target T3 (860 ppm) yields the brightest spectra in the region of the singly ionized lines. Once can only conclude that for the plasmas formed with the highest Cu concentration, namely T4 at 2600 ppm, these Cu^+ lines suffer strong attenuation due to opacity of both the single plume and the stagnation layer formed by the dual colliding plasma system. However, the atomic copper 521.94 nm line is at least equally intense for all targets and in the case of the annular plasma scales with target concentration.

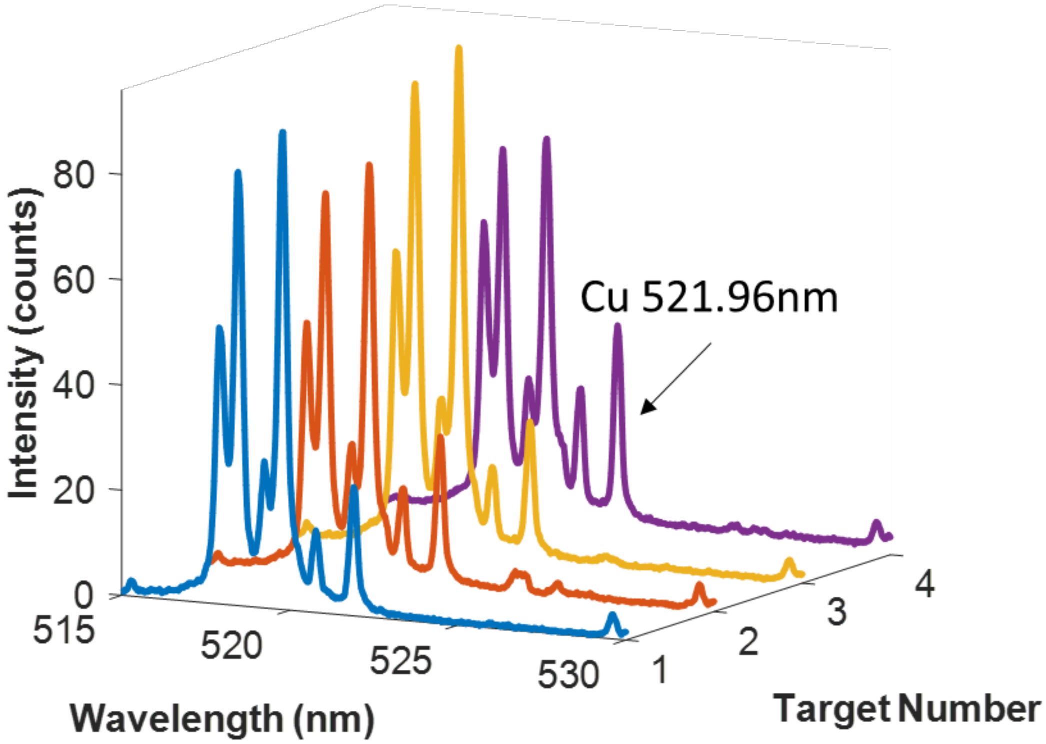

Figure 6.4: Time and space integrated spectra, centred at 519 nm for each aluminium target, captured from a single plasma generated with laser energy of 28 mJ. The Cu concentration values for T1 to T4 are 141 (blue), 184 (red), 860 (orange) and 2600 (purple) ppm respectively.

6.3 Signal to Background Ratio

The spectra for each focusing geometry are shown in Figure 6.5, Figure 6.6 and Figure 6.7 for total laser pulse energies of 28 mJ, 38 mJ and 52 mJ respectively. The target used here was T4 with a copper concentration of 2600 ppm. The variation in signal-to-background ratio (SBR) for each geometry and pulse energy can be gleaned from these plots. Although the maximum absolute signal varies from case to case it is clear that the signal to background ratio is highest for the annular colliding plasma system at the low end of the energy range, i.e., around 28mJ. Specifically at 28 mJ the absolute signal levels from both the single plasma plume and the stagnation layer formed at the collision front between the pair of colliding plumes are much lower than for the annular plasma and the SBRs are poorer.

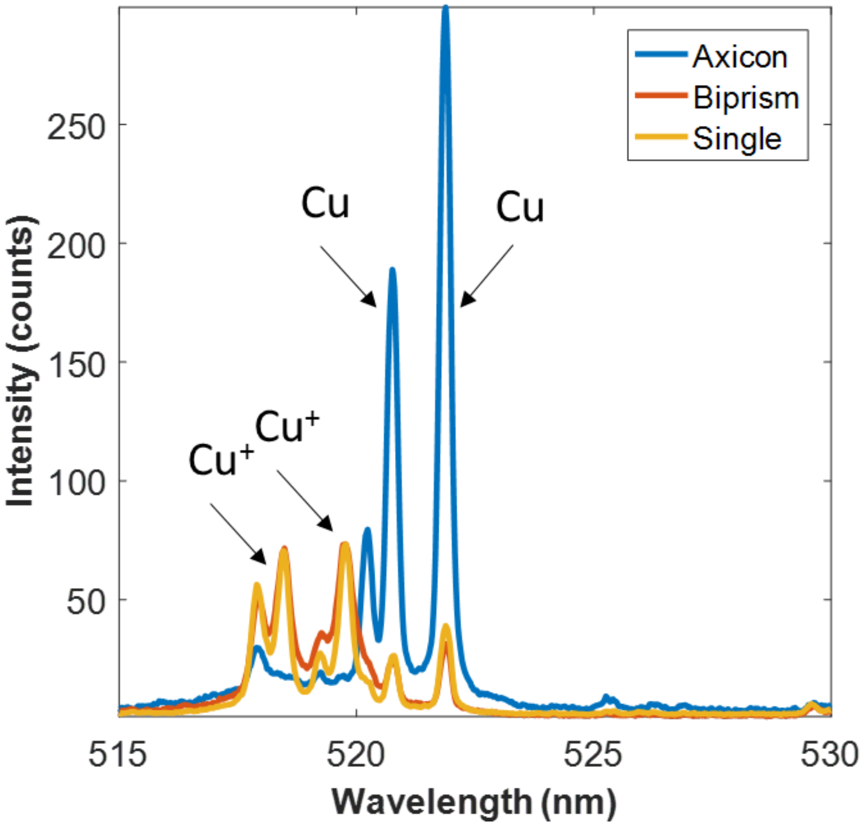

Figure 6.5: Time and space integrated spectrum centred at 519 nm captured from the stagnation layer formed at the centre of an annular plasma, the stagnation layer formed between two seed plasmas (14 mJ per seed) and a single plasma generated from target 4 with a laser energy of 28 mJ.

For a laser energy of 38 mJ there is an abundance of ion lines in the spectra (Figure 6.6). Most prominent are the 518.48 nm and 519.57 nm singly ionised copper lines which are strongest in the dual colliding plasma case with the Cu^+ signal eclipsing the neutral copper line of interest for LIBS applications. In the single plasma case the signal from all of these lines appear with roughly equal intensity, whereas in the annular plasma case the neutral line continues to dominate, albeit it sits on a higher continuum level than in the 28 mJ case.

The increase from 28 mJ to 38 mJ makes it apparent that stagnation layer in the dual colliding case is optimised for line emission within the 517nm to 520 nm window (mostly from Cu^+).

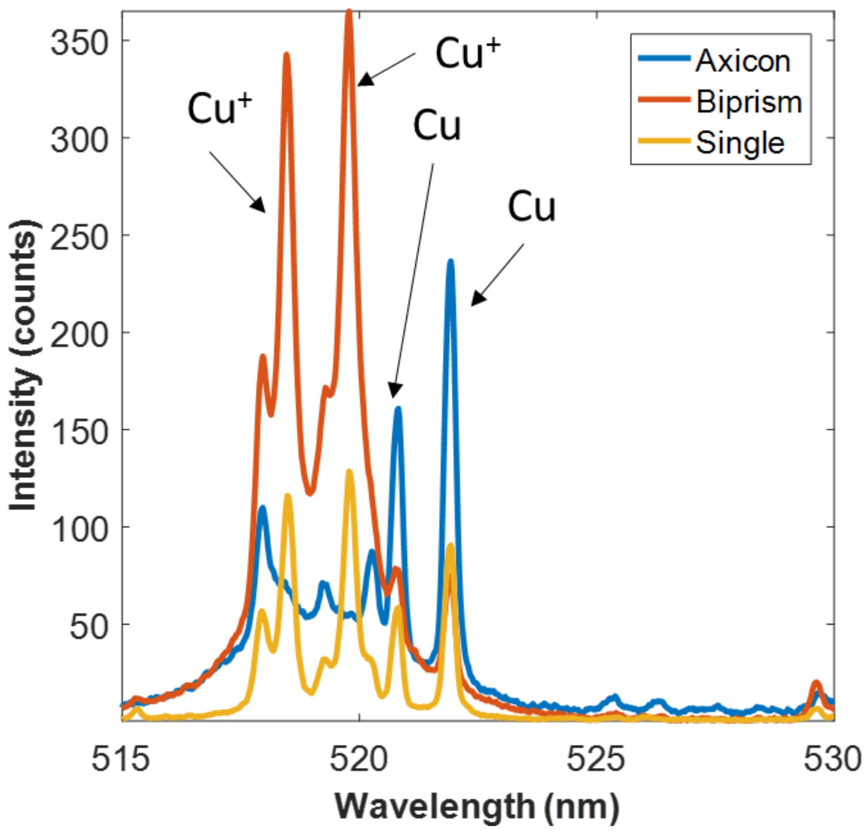

Figure 6.6: Time and space integrated spectrum centred at 519 nm captured from the stagnation layer formed at the centre of an annular plasma, the stagnation layer formed between two seed plasmas (19 mJ per seed) and a single plasma generated from target 4 with a laser energy of 38 mJ.

Neutral and singly ionized copper emission from single plumes is quite weak indicating, as expected, that the higher plasma temperature favours more highly charged ions. For the annular colliding plasma case, the stagnation layer is hotter and singly ionized emission begins to appear. The relative intensities, widths and shapes of the lines indicate that opacity maybe also a problem in this case.

Moving to the highest total laser pulse energy of 52 mJ, the background signal is highest for the axicon assisted stagnation layer (Figure 6.7). The background signal achieves a level almost half that of the 521.96 nm copper line and is comparable to the line intensities in the dual colliding and single plasma cases. This, in summary, as the pulse energy increases the SBR for the annular colliding plasma system decreases.

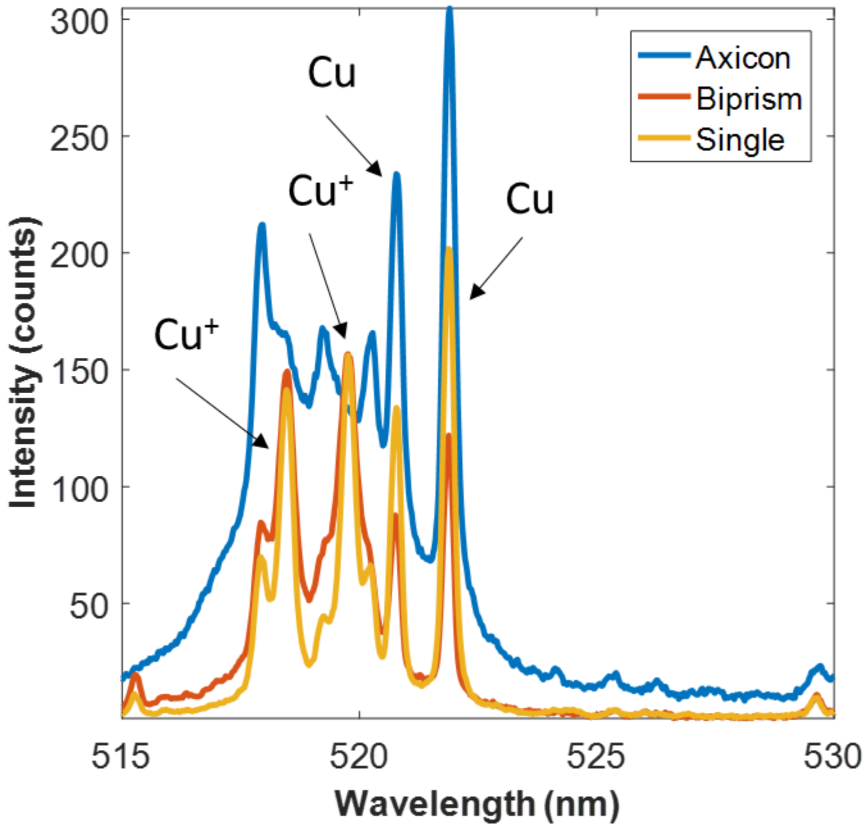

Figure 6.7: Time and space integrated spectrum centred at 519 nm captured from the stagnation layer formed at the centre of an annular plasma, the stagnation layer formed between two seed plasmas (26 mJ per seed) and a single plasma generated from target 4 with a laser energy of 52 mJ.

The signal to background ratios, for the 521.96 nm neutral line, summarised in Table 6.1, show clear trends. In the annular case, as the laser energy increases the signal to background ratio decreases from ca. 10 to 4, in the dual colliding case it remains reasonably flat in the 3 – 5 range, while in the single plasma plume case it increases by 50% from 6 to 9.

*Table 6.1**:** Signal to background ratio for the 521.96 nm copper neutral line, emitted from a plasma formed on target 4, for each focusing geometry.*

Energy	28 mJ	38 mJ	52 mJ
Annular Plasma	10.2	6.5	4.2
Two Seed Plasmas	4.7	2.8	5.2
Single Plasma	5.8	9.2	9.4

6.4 Limit of Detection of Trace Copper in Bulk Aluminium

Calibration curves are presented in this section for each focusing geometry and for all three laser energies of 28 mJ, 38mJ and 52 mJ in Figure 6.8, Figure 6.9 and Figure 6.10 respectively. In each case a linear fit yields the slope [Intensity (counts)/concentration (ppm)].

The values of the limits-of-detection (LOD) extracted from the calibration curves, and shown in Table 6.2, are in line with the state of the art for commercial LIBS systems. One clear trend in these values is that the limit of detection in the annular plasma case worsens as the energy of the laser is increased. This is to be expected as the fingerprint line is an atomic line, which should be strongest at lower on-target irradiances that do not favour the formation of ions and continuum emission via bremsstrahlung and/or recombination processes.

This increase (i.e., degradation) in the limit of detection with laser pulse energy for the annular case can be attributed to the background signal increasing at a greater rate than the line intensity of the copper neutral with laser energy. In the dual colliding plasma (biprism) case the optimum limit of detection, for the configurations used, also occurs in the 28 mJ case. In the single plasma case the lowest limit of detection is achieved with laser energy of 52 mJ.

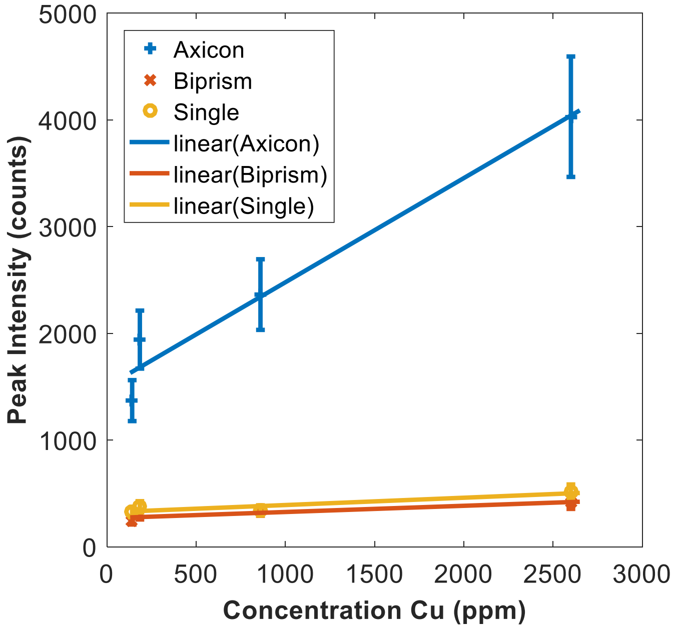

*Figure 6.8***:** *Calibration curves constructed using the 521.96 nm copper neutral line for each focusing geometry. Plasmas were generated with a laser energy of 28 mJ on each of the four targets. A linear regression of each dataset is also shown, the parameters of which are given in Table 6.2.*

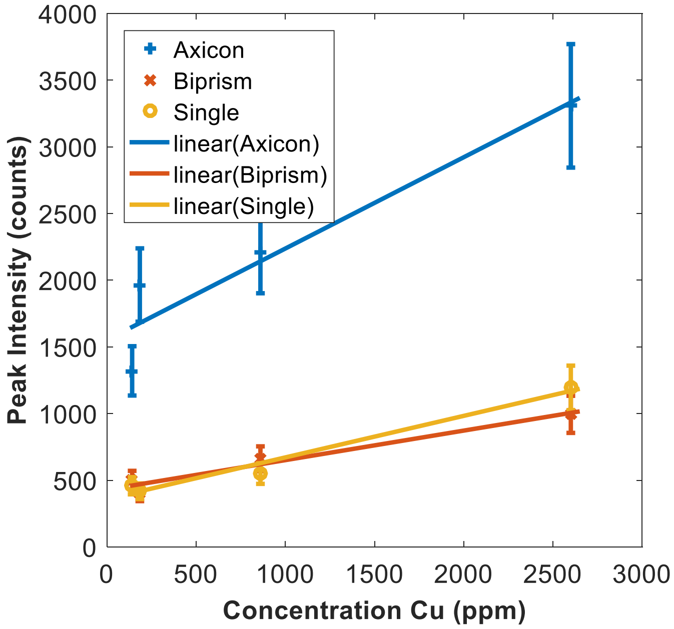

Figure 6.9: Calibration curves constructed using the 521.96 nm copper neutral line for each focusing geometry. Plasmas were generated with a laser energy of 38 mJ on each of the four targets. A linear regression of each dataset is also show, the parameters of which are given in Table 6.2.

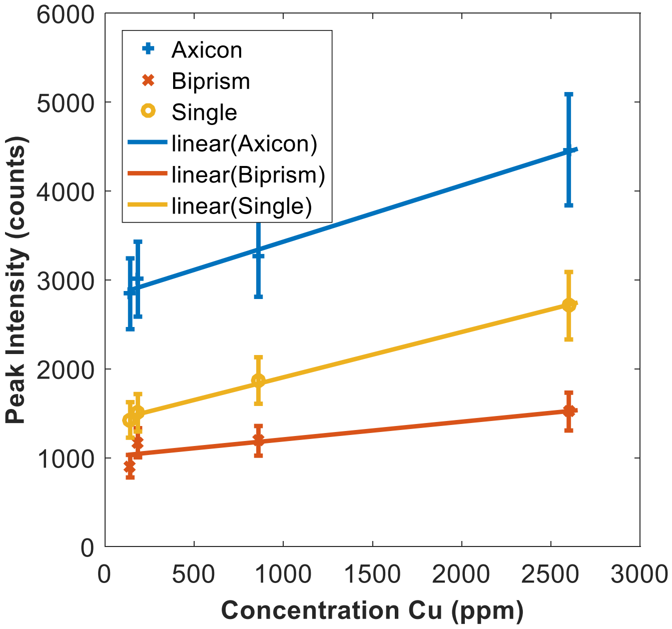

Figure 6.10: Calibration curves constructed using the 521.96 nm copper neutral line for each focusing geometry. Plasmas were generated with a laser energy of 52 mJ on each of the four targets. A linear regression of each dataset is also show, the parameters of which are given in Table 6.2.

It is clear from Table 6.2 that the limit of detection of a LIBS system is quite sensitive to the experimental conditions under which the calibration curve is constructed. The annular colliding plasma values are largely set by the increase in background continuum emission which increases with on-target irradiance at the expense of the atomic line emission. Growth in background continuum for the annular system while the analyte signal stalls at 38 mJ, and its impact on the standard deviation of the background of the system drive a large swing in the LOD.

The limit of detection values presented are on the same order of magnitude with similar single plasma based experiments which quantify trace copper in bulk aluminium [19-20]. The limit of detection is on the same order of magnitude for the axicon at 28 mJ and the single plasma at 52 mJ.

Table 6.2: Limit of detection (parts per million) and coefficient of determination for Cu in an Al matrix obtained from the calibration curves constructed for each combination of focusing geometry and laser energy.

Configuration	**LOD (ppm)**	**Line of Best Fit**	**R^2**
Axicon 28mJ	1.4	0.976x + 1502	0.96
Biprism 28mJ	18.1	0.058x + 268	0.87
Single 28mJ	7.8	0.069x + 322	0.84
Axicon 38mJ	5.4	0.685x + 1552	0.91
Biprism 38mJ	5.5	0.222x + 429	0.96
Single 38mJ	1.5	0.311x + 360	0.98
Axicon 52mJ	6.2	0.634x + 2797	0.99
Biprism 52mJ	5.7	0.199x +1008	0.83
Single 52mJ	1.8	0.510x + 1395	0.99

6.5 Summary

Limits-of-detection (LOD) have been presented for the trace element Cu in an Al matrix have been presented for three different plasma systems, namely a single plasma plume, a stagnation layer formed in a dual colliding plasma plume experiment and a stagnation layer formed along the axis of symmetry of an annular colliding plasma. Experiments were carried out for three different laser pulse energies, 28 mJ, 38 mJ and 52 mJ. The neutral copper line at 521.96 nm was chosen for these LOD determinations. For these specific cases the LOD was found to be best for an annular colliding plasma at 28 mJ followed closely by a single plasma plume at 52 mJ.

Bibliography

[1] D. A. Cremers, F.-Y. Yueh, J. P. Singh, and H. Zhang, "Laser-Induced Breakdown Spectroscopy, Elemental Analysis Update based on the original article by Fang-Yu Yueh, Jagdish P. Singh, Hansheng Zhang, *Encyclopedia of Analytical Chemistry*, 2000, John Wiley & Sons, Ltd.," *in Encyclopedia of Analytical Chemistry*, American Cancer Society, 2012.

[2] D. W. Hahn and N. Omenetto, "Laser-Induced Breakdown Spectroscopy (LIBS), Part I: Review of Basic Diagnostics and Plasma--Particle Interactions: Still-Challenging Issues Within the Analytical Plasma Community," *Appl. Spectrosc.*, Vol. 64, no. 12, p. 335A-366A, 2010.

[3] D. W. Hahn and N. Omenetto, "Laser Induced Breakdown Spectroscopy (LIBS), Part II: Review of Instrumental and Methodological Approaches th Material Analysis and Applications to Different Fields," *Appl. Spectrosc.,* 2012.

[4] J. Dardis and J. T. Costello, "Stagnation layers at the collision front between two laser-induced plasmas: A study using time-resolved imaging and spectroscopy," *Spectrochimica Acta Part B*: *At. Spectrosc.*, Vol. 65, no. 8. pp. 627–635, 2010.

[5] R. P. Singh, S. L. Gupta, and R. K. Thareja, "Spectroscopic investigation of colliding plasma plumes," *Spectrochem. Acta Part B: At. Spectrosc.*, no. 88, pp. 2013.

[6] K. F. Al-Shboul, S. M. Hassan, and S. S. Harilal, "Molecular formation in the stagnation region of colliding laser-produced plasmas," *Plasma Sources Sci. Technol.,* Vol. 25, no. 6, Art. No. 65017, 2016.

[7] A. McNaught, A. D., Wilkinson, IUPAC. *Compendium of Chemical Terminology*, 2nd ed. (the "Gold Book"). Blackwell Scientific Publications, Oxford, 1997.

[8] R. Noll, C. Fricke-Begemann, S. Connemann, C. Meinhardt, and V. Sturm, "LIBS analyses for industrial applications – an overview of developments from 2014 to 2018," *J. Anal. At. Spectrom.*, Vol. 33, no. 6, pp. 945–956, 2018.

[9] M. M. ElFaham, M. Okil, and A. M. Mostafa, "Limit of detection and hardness evaluation of some steel alloys utilizing optical emission spectroscopic techniques," *Opt. Laser Technol.*, Vol. 108, pp. 634–641, 2018.

[10] D. N. Stratis, K. L. Eland, and S. M. Angel, "Dual-Pulse LIBS Using a Pre-ablation Spark for Enhanced Ablation and Emission," *Appl. Spectrosc.,* Vol. 54, no. 9, pp. 1270–1274, 2000.

[11] R. González, P. Lucena, L. M. Tobaria, and J. J. Laserna, "Standoff LIBS detection of explosive residues behind a barrier," *J. Anal. At. Spectrom.,* Vol. 24, no. 8, pp. 1123–1126, 2009.

[12] D. Díaz, A. Molina, and D. Hahn, "Effect of laser irradiance and wavelength on the analysis of gold- and silver-bearing minerals with laser-induced breakdown spectroscopy," *Spectrochim. Acta Part B At. Spectrosc.*, Vol. 145, pp. 86–95, 2018.

[13] E. Mal, R. Junjuri, M. K. Gundawar, and A. Khare, "Optimization of temporal window for application of calibration free-laser induced breakdown spectroscopy (CF-LIBS) on copper alloys in air employing a single line," *J. Anal. At. Spectrom.*, 2019.

[14] D. Sun, Y. Ma, Y. Wang, M. Su, Q. Lu, and C. Dong, "Determination of the limits of detection for aluminum-based alloys by spatially resolved single- and double-pulse laser-induced breakdown spectroscopy," *Anal. Methods*, Vol. 10, no. 22, pp. 2595–2603, 2018.

[15] R. E. Russo, "Laser Ablation," *Appl.Spectrosc.*, Vol. 49, no. 9, p. 14A–28A, Sep. 1995.

[16] D. Zhao et al., “Temporal and spatial dynamics of optical emission from laser ablation of the first wall materials of fusion device,” *Plasma Sci. Technol.,* Vol. 20, no. 1, p. 14022, 2017.

[17] R. El-Rashedy, H. Imam, K. Elsayed, and M. Mansour, “Spectroscopic investigation of plasma evolution induced by double pulse laser in distilled water,” *J. Plasma Phys.*, Vol. 83, no. 4, p. 905830406, 2017.

[18] M. Helmi, M. S. Aziz, and J. Ali, “Temporal emission of magnesium lines from laser-induced plasma and use in calibration curves,” *AIP Conf. Proc.*, Vol. 1824, no. 1, p. 30008, 2017.

[19] W. T. Y. Mohamed, “Improved LIBS limit of detection of Be, Mg, Si, Mn, Fe and Cu in aluminum alloy samples using a portable Echelle spectrometer with ICCD camera,” *Optics & Laser Technology*, Vol. 40, no. 1. pp. 30–38, 2008.

[20] H. Li, M. Liu, Z. Chen, and R. LI, “Quantitative analysis of impurities in aluminum alloys by laser-induced breakdown spectroscopy without internal calibration,” *Transactions of Nonferrous Metals Society of China*, Vol. 18, no. 1. pp. 222–226, 2008.

[21] M. Sabsabi, R. Héon, and L. St-Onge, “Critical evaluation of gated CCD detectors for laser-induced breakdown spectroscopy analysis,” Laser Induced Plasma Spectroscopy and Applications (LIBS 2004), Third International Conference, Vol. 60, no. 7. pp. 1211–1216, 2005

7. Conclusions

7.1. Summary and Conclusions

An investigation of both annular and dual colliding plasmas *in vacuo* was undertaken with a view to forming more symmetrical stagnation layers than had been formed in previous work. An annular beam profile was achieved by focusing the far field of a ns pulsed laser beam which had passed through an axicon. A symmetrical energy distribution and beam profile was ensured in the dual colliding case by passing a ns pulsed beam through a biprism rather than a wedge prism, as had been used in previous work. A system to image expansion of each plasma formed (seeds and stagnation layers) parallel to the propagation direction of the laser was also developed through the use of an off-axis parabolic mirror that had a small hole drilled through its centre point. Time-integrated and time resolved fast imaging along with time integrated and time resolved spectroscopy were used to track the space evolution of, and diagnose, these colliding plasma systems from both 'side on' and 'head on' viewing angles.

Broadband time integrated and time resolved imaging experiments were presented in Chapter 4. Formation of a stagnation layer at the centre of an annular plasma was observed, to the best of my knowledge, for the first time. A comparison was drawn between such an 'annular stagnation layer' and the stagnation layer formed at the centre of two colliding plasmas. The 'annular stagnation layer' was found to create a brighter, shorter stagnation layer.

Time integrated and time resolved spectroscopy results were presented in Chapter 5 and used to diagnose each stagnation layer. Both plasma densities and temperatures were extracted from line broadening and ion intensity ratios respectively.

Chapter 6 presents time integrated Laser Induced Breakdown Spectroscopy measurements were taken, *in vacuo,* from four known standard samples for three focusing geometries; annular, dual colliding and single point foci. The standard samples consisted of bulk aluminium containing various trace elements, of which copper was studied. The signal to background ratio for each focusing geometry was extracted and the limit of detection determined. An atomic copper emission line was used to determine the limit-of-detection (LOD) for Cu in each case. The LOD was lowest for a stagnation layer formed in an annular colliding plasma system for low pulse energies, specifically 28 mJ. It was closely followed by a single plasma plume formed at a pulse energy of 52 mJ.

7.2. Future Work

Time and Space Resolved Spectroscopy

All spectra were binned along the spatial direction to improve the signal quality for presentation and analysis. However, it is clear that further analysis of the same spectra, especially employing the inherent space resolution would provide additional valuable information on how parameters such as electron density and temperature, ionization balance and excited state distributions vary in space at each time point. It would also elucidate how opacity effects on line intensities vary in space in both the single plasma plumes and colliding plasma systems.

Interferometry

Interferometry can be used to investigate the plasma at very early lifetimes ($0 - 40\, ns$) to obtain electron densities. The method of electron density determination via Stark broadening used in this work was not able to obtain results before c.a. $40\, ns$ due to continuum emission and line blending. Therefore interferometry could shed some light on these early time delays when the initial plasma collisions occur.

Ion Measurements and VUV Spectroscopy

The spectroscopy presented shows differences between the species of ions generated by annular and dual colliding plasmas for the observed windows. While the energy supplied by the laser was kept constant across focusing geometries, the power density was not. A full spectral analysis comparison of both of these focusing geometries should give further insight into the processes driving stagnation layer formation. If this spectral data was coupled with ion diagnostics from a Faraday cup or an electrostatic analyser, the possibility of using stagnation layers for ion sources could be explored.

Broadened LIBS Parameter Space

The initial aim of this work was to show an improvement in the limit of detection of LIBS by adding a single optical element to existing system, which can be seen in Chapter 6. Further work should now be carried out to compare the limit of detection over a range of pressures, with the aim of moving to a system at atmospheric pressure. Efforts should also be made to equalise the power density across the three compared focusing geometries, a laser with a lower range of energy output would be required to achieve this, whilst keeping all other parameters constant.

List of Figures

List of Tables

Appendices

ECTS Courses Taken:

- EE602 Components for Optical Communication
- INSPIRE Introduction to Nanoscience
- CS507 Advanced Statistics & Chemometrics
- GS601 Intellectual Property & Commercialization
- GS602 Postgraduate Tutor/Demonstrator Module
- GS607PS Laboratory Tutoring

Workshops Attended:

- Safelab 1&2 Postgraduate Modules 2013/14
- COST Action MP1203 Dublin Oct 2013
- VUV/EUV Workshop UCD Dublin November 2nd, 2013
- Applied Spectra Inc. Laser Based Analytical Techniques workshop. San Francisco Feb, 2014
- European XFEL Users Meeting Jan 2015
- NCPST Plasma/Nanoscience Conference DCU Dublin March 2014
- Perdue PIRE Annual Meeting DCU Dublin July 2015

Research Visits:

- Indian Institute of Technology Kanpur, Laser Produced Plasma group. 16th March 2014 – 15th April 2014.
- Driving a Fano resonance: Creating stable inner-valence holes and highly aligned outer-valence hole states. 23rd Nov – 1st Dec 2014, FERMI, ELETRA, Trieste, Italy.

Oral Presentations:

- Determination of Detection Limits of Trace Elements in Aluminium Using Stagnation Layers. Delaney B., Kelly T. J., Kennedy E. T., Costello J. T., EMSLIBS, Pisa, 2017.

Poster Presentations:

- An Investigation into Laser Drilling for use in Laser Induced Breakdown Spectroscopy (LIBS). Delaney B., Kelly T. J., Kennedy E. T., Costello J. T., 5th NCPST Postgraduate Poster competition, DCU, December 2013.
- An Investigation into Laser Drilling for use in Laser Induced Breakdown Spectroscopy (LIBS). Delaney B., Kelly T. J., Kennedy E. T., Costello J. T.,DCU BOC Poster competition, Dublin, February 2015.
- An Investigation into Laser Drilling for use in Laser Induced Breakdown Spectroscopy (LIBS) (Ver2). Delaney B., Kelly T. J., Kennedy E. T., Costello J. T., 42nd IOP Plasma conference, Milton Keynes England, March 2015.

- Stagnation Layer Formation in Annular Copper Plasmas. Delaney B., Kelly T. J., Kennedy E. T., Costello J. T., Photonics Ireland, Cork, September 2015.
- Detection Limits for Trace Elements in Steel for Different LIBS Geometries. Delaney B., Kelly T. J., Kennedy E. T., Costello J. T., 9th international conference on LIBS, Chamonix France, September 2016.